GEORG-AUGUST-UNIVERSITÄT
GÖTTINGEN

Fakultät für
Physik

Master's Thesis

Studien zur Messung der Zerfallsbreite des Top-Quarks am ATLAS Experiment

Studies on the Measurement of the Top-Quark Decay Width at the ATLAS Experiment

prepared by

Dominik Müller

from Wolfsburg

at the II. Institute of Physics

Thesis Period:	1st April 2014 until 30th September 2014
Thesis Number:	II. Physik-UniGö-MSc-2014/04
First Referee:	Prof. Dr. Arnulf Quadt
Second Referee:	Prof. Dr. Ariane Frey

Abstract

The top-quark is special amongst the known elementary particles and even more so amongst a particular subset of these particles – the quarks. While being significantly heavier than any other known elementary particle, it is unique amongst the quarks due to its very large decay width. It is affected by all possible decays of the top-quark and hence opens a window to physics beyond the Standard Model. This thesis presents studies on the measurement of this quantity in the context of semileptonically decaying $t\bar{t}$ pairs in the ATLAS experiment at the Large Hadron Collider. It is estimated by using the fiducial, differential cross-section $\mathrm{d}\sigma/\,\mathrm{d}m_t$ defined on the level of stable particles. The motivation as well as other potential applications of this fiducial cross-section are discussed. In the presented studies, the fiducial cross-section is obtained by unfolding the measured differential cross-section using singular value decomposition. Emphasise is placed on the careful tuning of the unfolding procedure and the evaluation of its performance. The presented studies are meant to be proof-of-concept studies to determine whether such an approach is feasible and should be continued in a real measurement or not.

Zusammenfassung

Das Top-Quark nimmt einen besonderen Platz unter den bekannten Elementarteilchen, im Besonderen aber unter den Quarks, ein. Es ist schwerer als alle anderen Elementarteilchen und einzigartig unter den Quarks aufgrund seiner großen Zerfallsbreite. Diese berücksichtigt alle möglichen Zerfälle des Top-Quarks, sodass eine Abweichung von den Standardmodellvorhersagen einen Hinweis auf neue Physik geben kann. Diese Arbeit präsentiert Studien zur Messung dieser Größe im Kontext von semileptonisch zerfallenden $t\bar{t}$ Paaren, welche im ATLAS Experiment am Large Hadron Collider beobachtet werden. Die Zerfallsbreite wird aus einer Messung des differenziellen Wirkungsquerschnitts $\mathrm{d}\sigma/\,\mathrm{d}m_t$ auf dem wohldefinierten Teilchenniveau bestimmt. Dieser Arbeit diskutiert die Motivation und Definition einer einer solchen Messung des Wirkungsquerschnitts und stellt weitere mögliche Anwendungen vor. In den vorgestellten Studien wird dieser Wirkungsquerschnitt durch das Entfalten der im Detektor gemessen Verteilung mittels Singulärwertzerlegung bestimmt und ein Schwerpunkt dieser Arbeit ist durch die Vorstellung sowie Untersuchung dieser Entfaltungsmethode gegeben. Die präsentierten Studien stellen Machbarkeitsstudien dar, um zu bestimmen, ob ein solcher Ansatz weiterverfolgt werden sollte oder nicht.

Contents

1 Introduction

The ongoing advancement of humankind is driven by the irrepressible aspiration to understand how things function and what they are made of. Elementary particle physics is at the forefront of this endeavour as it strives to describe the smallest constituents of matter. It is the key to our endless curiosity of understanding the most fundamental questions: When and – more important – *how* did the universe begin? Although the ultimate answer is yet unknown, the Standard Model of elementary particle physics is the current theoretical framework describing the elementary particles and their interactions. It is the culmination of work done over the past decades while constantly being improved and extended. Nonetheless, the core concepts of the model withstand all efforts trying to falsify them using experiments of ever increasing magnitude. Huge laboratories operate particle accelerators reaching higher and higher energies to test the predictions of the Standard Model and to advance our knowledge of elementary particles and their interactions. One of these advances is the discovery of the top-quark – one of six known quarks – at the Tevatron at Fermilab. This quark is set apart from all other elementary particles by one property: its incredibly large mass.

This large mass also affects other properties and hence the top-quark is unique amongst the quarks. Studying this particle could be pivotal for discovering physics beyond the Standard Model due to the large amount of energy being available in its decay.

However, the decay width of the top-quark, which is most important when describing the decay, has not yet been measured precisely but is predicted to be much larger than for any other quark. This corresponds to a very short life time which is even shorter than the timescale needed to form bound states with other quarks. Consequently, the top-quark is the only quark which can be observed as a “bare” quark, preserving its properties in the decay. Entire analyses, like the measurement of spin correlation, base their motivation on this feature which sets the top-quark apart from all other quarks.

Additionally, the decay width of the top-quark is sensitive to physics beyond the Standard Model. Many possible extensions and additional particles would participate in the decay and hence enter in the decay width.

The top-quarks studied here are produced at the Large Hadron Collider (LHC) in Geneva. It is the newest and most powerful particle accelerator available for scientists all around the world as well as the largest machine ever built by humankind. Several detectors record the result of the proton-proton collisions delivered by the LHC. The analysis presented in this thesis uses events with top-quark pairs decaying to one charged lepton, the corresponding

(anti-)neutrino and jets recorded by the ATLAS detector.
The analysis explores the potential for measuring the decay width using a fiducial measurement of the cross-section – a quantity proportional to the rate of events – as a function of the reconstructed invariant mass of the top-quark. The result of a fiducial measurement should be independent of detector as well as of modelling effects. As will be discussed in this thesis, only well defined objects on the level of stable particles – the particle level – should be used in such a measurement. Once obtained, the fiducial measurement can be stored and later reused easily in a combination with results obtained by other experiments. It can also be used to test theoretical models without the need to include detector effects in the prediction.

The next chapter will give an introduction to the Standard Model of elementary particle physics followed by a more detailed discussion of the top-quark and its properties. Additionally, theoretical predictions and the experimental status of decay width measurements are presented. Chapter 3 will describe both the LHC and the ATLAS experiment. Unfolding, which is used to correct for detector effects in general as well as the method used in this analysis are detailed in Chapter 4. Chapters 5 and 6 present the particle level and studies performed to investigate the expected sensitivity on the decay width and mass. The following Chapters 7 and 8 introduce detector effects and estimate the impact on the previous studies. Chapter 9 closes the circle by discussing the correction of detector effects by unfolding the measured distributions down to particle level. Concluding this thesis, Chapter 10 investigates one major source of systematic uncertainty before a conclusion is given.

Natural units $\hbar = c = e = 1$ are used throughout this thesis and all given values for particle properties are taken from [1] unless otherwise stated.

2

Theoretical Background

This analysis presents studies on the measurement of the top-quark decay width – a property predicted by the Standard Model – and thus the fundamental aspects of this theory will be presented in this chapter. Additionally, the physics of the top-quark and its unique position among the quarks will be discussed followed by a brief description of Monte Carlo event generators – a tool crucial for the performed studies.

2.1 The Standard Model of Particle Physics

The current Standard Model of elementary particle physics serves as theoretical framework to understand the behaviour and properties of the microcosm. It is based on quantum field theories which describe the interactions between fermions – half integer spin particles – mediated by bosons with integer spins. The Standard Model currently incorporates three fundamental forces: the electromagnetic, weak and strong force. The fourth fundamental force – gravity – is not included.

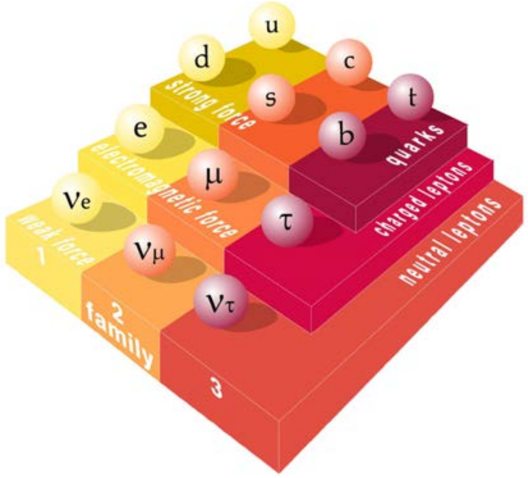

Fig. 2.1: Overview of all known elementary fermions and their affiliation to one of the three families.

2.1.1 The Elementary Particles

Elementary particles are the basic building blocks of matter and have no known substructure. The Standard Model currently comprises twelve different spin-$1/2$ particles – the so-called fermions. One distinguishes between two distinct kinds of elementary fermions: quarks and leptons. An overview of all known elementary fermions is given in Figure 2.1. The set of six known quarks is further divided into two groups: up- and down-type quarks while the known set of leptons is separated into electrically charged and neutral particles, the so-called neutrinos. All particles within one of these four groups share the same quantum numbers. As visualised in Figure 2.1, a second ordering scheme is implied which places the known elementary fermions in one of three families. All observed stable matter is solely built by the members of the first family – the electron, the electron neutrino, the up- and the down-quark. The particles in the other two families are unstable and can only be observed for a brief moment after their creation in high energetic processes, e.g. in a particle collider.

The aforementioned separation into distinct types of fermions is made due to their different quantum numbers. In analogy to the electric charge, one can interpret the different quantum numbers presented in the following as the charges of one of the fundamental forces.

Electric Charge The defining property which separates the four different types of particles is the electric charge Q. Charged leptons carry $Q = -1$ whereas their counterpart – the neutrinos – do not have an electric charge and hence will not participate in electromagnetic processes. The up-type quarks carry an electric charge of $Q = +{}^2\!/\!_3$ whereas the down-type quarks carry $Q = -{}^1\!/\!_3$.

Isospin The isospin, typically described by its third component T_3, is the charge of the weak interaction. Due to the vector minus axialvector ($V - A$) structure of the charged current interaction, it only couples to left-handed particles. One has to carefully differentiate between the chirality and the helicity of particles: the chirality is a quantity invariant under Lorentz boosts and obtained by using the chirality operator γ^5 on a spinor representing the particle. The helicity is the sign of the projection of the spin onto the momentum axis. It is not Lorentz invariant (unless the particle is massless) and thus in general not identical to the chirality. The handedness refers to the chirality of the particle. Therefore, the left-handed leptons and quarks are ordered in isospin doublets ($T_3 = \pm{}^1\!/\!_2$) while the right-handed particles are present in isospin singlets ($T_3 = 0$):

$$\begin{pmatrix} \nu \\ l^- \end{pmatrix}_L \quad \begin{pmatrix} u \\ d \end{pmatrix}_L \qquad\qquad u_R \qquad d_R \qquad l^-_R \ .$$

Neutrinos solely couple to $V - A$ structures and are assumed to be massless in the Standard Model. Conclusively, only left-handed neutrinos participate in the interactions described by the Standard Model.

Colour Charge The colour charge is the charge of the strong interaction and only carried by quarks. It can take three different values which are called, in analogy to real colours, red, blue and green. Therefore, leptons do not participate in the strong interaction.

For every particle there exists an antiparticle of equal mass but inverted quantum numbers. The interactions are included in the Standard Model by requiring the Lagrangian of a free particle to be invariant under local gauge transformations. They are described in the following.

2.1.2 The Electroweak Interaction

The electromagnetic interaction is included in the Lagrangian by requiring it to be invariant under the local gauge transformation $U(1)_Q$. To achieve the gauge invariance, one has to modify the derivative and introduce a local gauge field A_μ corresponding to the photon, the intermediating boson of the electromagnetic interaction. The same can be done to include the weak interaction by using $SU(2)_L$ as the symmetry group. This introduces three additional fields $W_\mu^{1,2,3}$ of which W_μ^1 and W_μ^2 are linearly combined to form the W^+ and W^- bosons. However, no correspondence to any known particle was found for the third component W_μ^3.

A solution to this problem was first developed by Weinberg, Salam and Glashow [2–4], who proposed to unify the descriptions of electromagnetic and weak interactions into the electroweak interaction described by a common gauge symmetry group:

$$U(1)_Y \times SU(2)_L$$

where the hypercharge $Y = 2Q - T_3$ is the generator of the $U(1)_Y$ interaction which introduces a field B_μ to the Lagrangian to ensure gauge invariance. Mixing W_μ^3 and B_μ using a unitary matrix characterised by the Weinberg-angle θ_W, leads to two gauge fields:

$$\begin{aligned} A_\mu &= W_\mu^3 \sin(\theta_W) + B_\mu \cos(\theta_W) \text{ and} \\ Z_\mu &= W_\mu^3 \cos(\theta_W) - B_\mu \sin(\theta_W) \ . \end{aligned}$$

A_μ corresponds to the photon and only couples to electrically charged particles while the new gauge field Z_μ corresponds to the Z^0 boson which is the mediating particle of the weak neutral current interaction.

The charged current interaction given by the $SU(2)_L$ gauge symmetry group allows mixing between different generations of quarks because the weak eigenstates are not equal to the flavour eigenstates [5, 6]. This is described by the unitary CKM matrix which connects the weak down-type eigenstates $|d'\rangle$ to the flavour eigenstates $|d\rangle$:

$$\begin{pmatrix} | \, d'\rangle \\ | \, s'\rangle \\ | \, b'\rangle \end{pmatrix} = \begin{pmatrix} V_{ud} & V_{us} & V_{ub} \\ V_{cd} & V_{cs} & V_{cb} \\ V_{td} & V_{ts} & V_{tb} \end{pmatrix} \begin{pmatrix} | \, d\rangle \\ | \, s\rangle \\ | \, b\rangle \end{pmatrix} . \tag{2.1}$$

The square of the absolute value for each entry of the CKM matrix gives the probability for finding a specific flavour in a given weak eigenstate.

2.1.3 The Strong Interaction

The strong interaction is described by quantum chromodynamics and is given by the gauge symmetry group $SU(3)_C$. It describes the interactions of particles carrying a colour charge. The eight generators of $SU(3)_C$ result in eight different gluons. Those are the mediating particles in the strong interaction. Furthermore, they can couple to each other due to carrying colour charges themselves. The so-called *confinement* requires quarks to be bound in colourless hadrons because states with a net colour charge are not invariant under $SU(3)_C$ transformations. Therefore, quarks cannot be observed as free particles in nature. These colourless hadrons are either mesons $|q\bar{q}\rangle$ combining two quarks carrying a colour and the corresponding anticolour charge, or baryons $|qqq\rangle$ combining all three colours or anticolours. The strong coupling increases with increasing distance between two quarks which are bound by gluons in contrast to the weak coupling that decreases with increasing distance. If one tries to separate two quarks, there is a point where it is energetically more favourable to produce an additional quark-antiquark pair instead of increasing the distance any further. This results in *hadronisation* – a quark in the final state of any process spawns quark-antiquark pairs until the energy is too low and bound states between these quarks are able to form. These bound states are the aforementioned hadrons – the actual particles which are observable in experiments. Due to the large energies available in modern experiments, every final state quark yields a large number of hadrons. These hadrons typically form a cone-like structure, a so-called jet, which is measured in the detector.

2.1.4 The Higgs Mechanism

Up to this point, the theory describes the kinematics of massless fermions and their interactions mediated by massless bosons. Nevertheless, a variety of experiments have measured masses for the fermions and the W and Z bosons. This issue can be solved by the HIGGS mechanism [7, 8] where spontaneous symmetry breaking is used to include the masses of the fermions (except the neutrinos) and W and Z bosons while keeping the photon and gluon massless. This is achieved by adding a new doublet ϕ with a potential $V(\phi)$ to the Lagrangian. The potential has its minimum at $\phi \neq 0$ and thus rewriting the field ϕ with respect to the deviation of that minimum yields additional terms in the Lagrangian. These are divided into mass terms for the massive bosons and fermions as well as the coupling of these particles to a new gauge field. This new gauge field was interpreted as a new particle, the Higgs boson. It has been sought for several decades before it has finally been discovered in 2012 by the ATLAS and CMS collaborations at the LHC [9, 10].

2.2 The Top-Quark

This section gives an overview over the studied particle of this analysis – the top-quark. Several properties are discussed with a focus on the decay and theoretical predictions for the top-quark decay width. Furthermore, details on the production of $t\bar{t}$ pairs at the LHC and their possible decay channels are given.

2.2.1 Properties

In the Standard Model, the top-quark is the weak isospin partner of the bottom-quark thus having an isospin of $T_3 = +{}^1\!/\!_2$ and carrying an electric charge of $Q = +{}^2\!/\!_3$ as the two other up-type quarks. It has been discovered in 1995 by the CDF and D0 experiments at the Tevatron [11, 12]. The most intensively measured property of the top-quark is its mass. The most precise and published result is the combination of the results of the CDF and D0 collaborations at the Tevatron [13]:

$$m_t = 173.17 \pm 0.94 \text{ GeV} .$$

Very recently, a world-wide combination of this result and the current measurements of the ATLAS and CMS collaborations at the LHC became available [14]:

$$m_t = 173.34 \pm 0.76 \text{ GeV} .$$

Therefore, the top-quark is by far the heaviest known elementary particle with its mass being in the region of heavy atoms like gold and tungsten. Due to its large mass, the top-quark is the dominant fermion in loop corrections. The measured mass of the W boson is affected by tb loops depending on m_t and HW loops depending on m_H. This yields a relation between the masses which allowed to constrain the possible mass regions in Higgs boson searches and can now be used to test the consistency of the Standard Model.

Even though the top-quark has been discovered almost 20 years ago, many of its properties have not been measured and are simply assumed based on their theoretical predictions. Others have only been measured to a poor precision not allowing any meaningful comparison with their predicted values within the Standard Model. The isospin, the defining property placing the left handed top-quark in an isospin doublet with the bottom-quark, has actually never been measured. The electric charge has not been measured to a high precision but agrees with the Standard Model value while alternative models with a top-quark charge of $Q = -{}^4\!/_3$ could be excluded [15]. The very large decay width – and thus very short lifetime – sets the top-quark apart from all other quarks. However, this assumption is primarily based on theoretical predictions and has not been measured to a satisfactory precision. Exploring the potential of a decay width measurement is the goal of this analysis and thus its theoretical prediction as well as previous measurements are described in detail in Section 2.2.3.

2.2.2 Production of Top-Quarks at Hadron Colliders

In hadron colliders, top-quarks are predominantly produced in pairs consisting of a top t and an antitop $\bar{t}$ quark. The main production mechanism of these $t\bar{t}$ pairs in hadron colliders is the strong interaction between the gluon and quark components of the colliding protons. The leading order Feynman diagrams for quark-antiquark annihilation and gluon fusion are shown in Figure 2.2.

In a proton-proton (pp) collision, each parton carries an unknown fraction x of the proton's total momentum which varies in each event. Therefore, the total momentum along the beam axis in a single collision is unknown and thus cannot be used in the reconstruction and the analysis. As a consequence, the centre-of-mass energy between both partons $\sqrt{\hat{s}}$

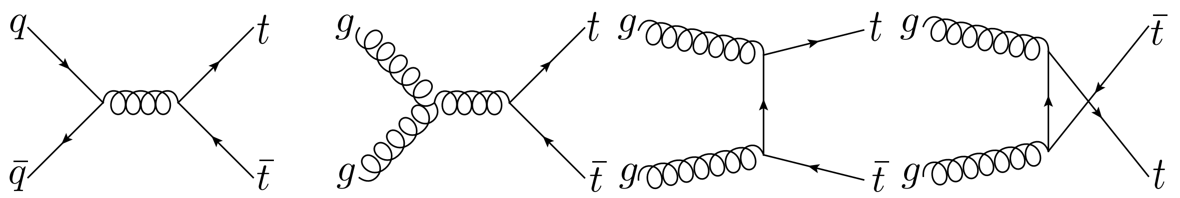

(a) $q\bar{q}$ annihilation **(b)** gg fusion

Fig. 2.2: Leading order Feynman diagrams for the $t\bar{t}$ production at hadron colliders via $q\bar{q}$ annihilation (a) and gg fusion (b).

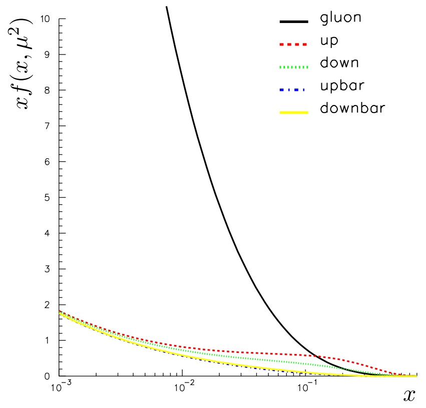

Fig. 2.3: PDF for $\mu = 2 \cdot 173$ GeV based on [17].

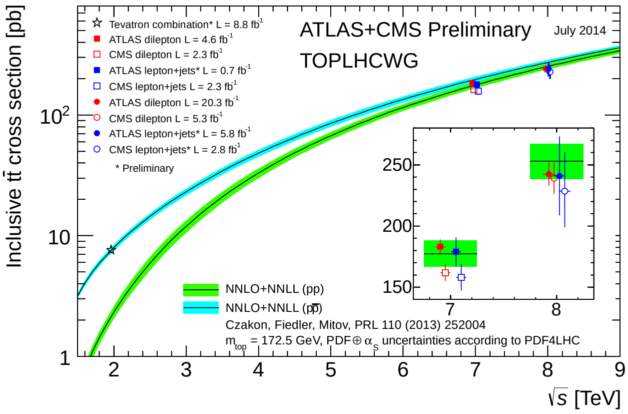

Fig. 2.4: Measured $t\bar{t}$ production cross section at the Tevatron and LHC at different centre-of-mass energies and their theoretical predictions [18].

is different in each event and typically substantially smaller than the total centre-of-mass energy $\sqrt{s}$ between the protons. The probability to find a parton with a certain momentum fraction in the proton is given by the parton distribution function (PDF) $f(x,\mu^2)$ with μ being the scale at which they are evaluated [16]. Figure 2.3 shows the CT10 PDF evaluated at the scale of $\mu = 2m_t$. For large proton energies, only a small momentum fraction of the proton's momentum is required to reach the minimum energy of $2m_t$ which is needed to produce a $t\bar{t}$ pair. Therefore, the gg fusion, depicted in Figure 2.2b, is the dominant production mechanism of $t\bar{t}$ pairs at the LHC. The total production cross-section for $t\bar{t}$ pairs in the collision of two protons can be – according to the factorisation theorem – written as [16]:

$$\sigma_{pp\to t\bar{t}} = \sum_{i,j} \int \int \mathrm{d}x_i \, \mathrm{d}x_j f\left(x_i, \mu^2\right) f\left(x_j, \mu^2\right) \sigma_{ij\to t\bar{t}}\left(x_i, x_j, \alpha_s, \hat{s}\right) \ . \tag{2.2}$$

Here, i and j refer to the different parton contents of a proton – quarks, antiquarks and gluons – and the sum is taken over all possible combinations to produce a $t\bar{t}$ pair at a given order. At leading order QCD production, at least two strong couplings are required, all possible diagrams are shown in Figure 2.2. At higher orders, $t\bar{t}$ pairs can also be produced from qg initial states. Furthermore, $\sigma_{ij\to t\bar{t}}$ is the partonic cross-section for the process. It depends on the parton centre-of-mass energy $\hat{s} = x_i x_j s$ and includes the phase space integration for the outgoing particles. The measured cross sections at the LHC and the Tevatron are shown in Figure 2.4 together with their predicted values. Overall,

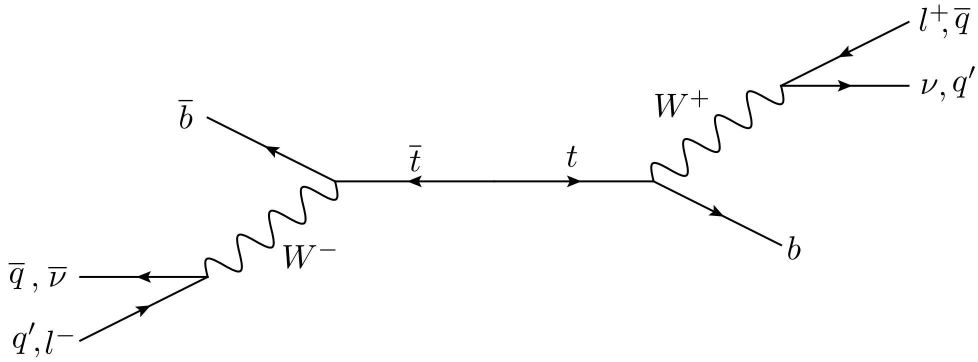

Fig. 2.5: Leading order Feynman diagram for the decay of a $t\bar{t}$ pair with all possible final states.

the measured values agree well with the theoretical predictions. The plot also shows the increasing contribution of gg fusion towards higher centre-of-mass energies as the difference in the predicted cross-sections for pp and $p\bar{p}$ becomes smaller.

It is also possible to produce single top-quarks in pp collisions via the electroweak interaction. However, the cross-sections for these processes are significantly smaller than the ones for the strong production of $t\bar{t}$ pairs.

2.2.3 Decay

Top-quarks decay almost immediately and thus cannot be observed directly but can be studied through their decay products. The following detailed discussion of this decay is essential in the understanding of the analysis presented here.

In the Standard Model, the top-quark decays through the weak interaction into a W boson and a down-type quark $t \to W^+ q_d$. In principle, this down-type quark can be a down-, strange- or bottom-quark. However, the corresponding CKM matrix element for the decay into a b-quark exceeds the ones for d- and s-quarks by far with a value of $|V_{tb}| = 1.021 \pm 0.032$ [1] and thus the top-quark decays almost exclusively into a b-quark. Beyond the Standard Model decays like the one into an up-type quark and a Z boson $t \to Zq_u$ – implying the existence of flavour changing neutral currents – have not been observed so far [19].

Decay of $t\bar{t}$ Pairs

As stated before, the top-quark is predominantly produced in $t\bar{t}$ pairs at hadron colliders and almost exclusively decays to a W boson and a bottom-quark $t \to Wb$. The subsequent decay of the W boson – either into two quarks or into a charged lepton and a neutrino – defines different decay channels of $t\bar{t}$ pairs as depicted in Figure 2.5. There are three different classes of $t\bar{t}$ decays which have to be treated differently due to their distinct final states. One speaks of a dilepton decay if both W bosons decay into leptons, with $l \in \{e, \mu, \tau\}$ and the corresponding neutrino, yielding a total of nine different combinations. The $l +$ jets channel is characterised by one leptonically and one hadronically decaying W boson. 36 combinations for such a final state exist, 12 for each of the possible leptons. In case both W bosons decay into quarks one speaks of an alljets event with a total of 36 combinations.

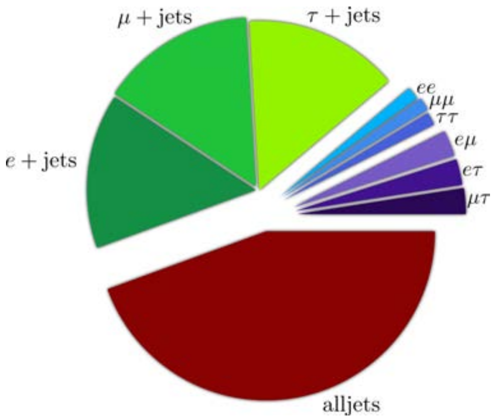

Fig. 2.6: Visualised $t\bar{t}$ branching ratios

Figure 2.6 shows the different final states and their branching ratios solely based on combinatorics (with a good agreement to the measured branching ratios [1]). Special consideration has to be given to the final states involving a τ lepton: this cannot be measured directly as it decays before it reaches any active parts of the detector. A τ also decays into a W boson and a tau neutrino. However, the W boson can then decay into an electron or muon with the corresponding neutrino or into quarks and thus events involving taus can contribute to different categories depending on the subsequent τ decay. Due to its large branching ratio as well as the clean signature with a high energetic charged lepton, this analysis uses e+jets and μ+jets events. This also includes $\tau +$jets events with a leptonically decaying τ lepton.

Decay Width

Assuming that the top-quark decays via $t \to Wq$ (q being any down-type quark), its decay width depends primarily on the top-quark mass m_t and the Fermi coupling constant G_F [20]. In leading order perturbation theory, the decay width can be obtained by calculating the leading order matrix element for the decay shown in Figure 2.7 and using Fermi's Golden Rule. Neglecting the masses of the down-type quark in the calculation and implying only three quark generations as well as the unitary of the CKM matrix $(|V_{td}|^2 + |V_{ts}|^2 + |V_{tb}|^2 = 1)$, one obtains: [16]

$$\Gamma_t = \frac{G_F m_t^3}{8\pi\sqrt{2}} \left(1 - \frac{m_W^2}{m_t^2}\right)^2 \left(1 + 2\frac{m_W^2}{m_t^2}\right) .$$

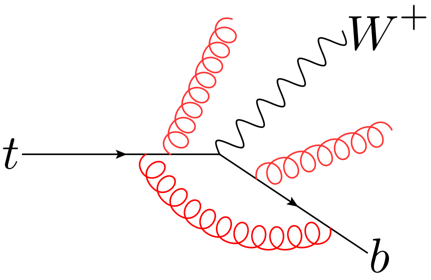

Fig. 2.7: Leading order t-quark decay (black) with examples for higher order QCD corrections (red).

Assuming the top-quark mass value from the world combination, one obtains $\Gamma_t = 1.51\,\text{GeV}$. However, several corrections due to quantum chromodynamics – some examples are depicted in Figure 2.7 – have to be considered in the calculation and substantially decrease the theoretical value [20].

Next-to-leading order QCD calculations yield a decay width of $\Gamma_t = 1.33\,\text{GeV}$ with a 1% uncertainty assuming $m_t = 172.5\,\text{GeV}$ [21, 22]. The inclusion of next-to-next-to-leading order QCD effects only changes the value within this 1% uncertainty and corrects it to $\Gamma_t = 1.32\,\text{GeV}$ [23]. The corresponding lifetime of the top-quark is $\tau \approx 0.5 \cdot 10^{-24}\,\text{s}$. This is shorter than the timescale at which hadronisation takes effect [16] and thus the top-quark is the only quark that can be studied as a "bare" quark. This allows to study effects such as the correlation of the top-quark and top-antiquark in $t\bar{t}$ pairs which are distorted for all other types of quarks due to hadronisation.

The total decay width of the top-quark is sensitive to physics beyond the Standard Model which modify the decay. An example for such a modification are the decays via neutral currents mentioned before. Furthermore, extensions to the Standard Model – like super symmetry – often introduce additional charged Higgs bosons [24]. These could be produced in the decay of top-quarks $t \to H^+ b$ and hence modify the value of Γ_t. However, current experimental results, which are presented in the following, are not yet precise enough to properly test realistic extensions to the Standard Model.

Current Measurements of Γ_t

Two possible approaches to infer on the top-quark decay width are currently undertaken: a heavily model-dependent, indirect measurements and a direct measurement which is less model dependent at the cost of a significant reduction in precision. Both approaches and the current measurements are presented in the following.

An **indirect measurement** can be performed when measuring the value $\mathcal{R}$ defined as:

$$\mathcal{R} = \frac{\mathcal{B}(t \to Wb)}{\sum\limits_{q=d,s,b} \mathcal{B}(t \to Wq)} ,$$

which is the ratio of decays to b-quarks and decays to all known down-type quarks. In the Standard Model, the denominator is equal to one and thus $\mathcal{R} = \mathcal{B}(t \to Wb)$. To extract the total decay width of the top-quark, one assumes that the Standard Model is valid and combines the measurement of $\mathcal{R}$ with a cross-section measurement of single top-quarks:

$$\Gamma_t = \frac{\sigma_t}{\mathcal{B}(t \to Wb)} \cdot \frac{\Gamma(t \to Wb)}{\sigma_t^{theo}} .$$

Here, σ_t^{theo} is the theoretical t-channel cross-section for single tops and $\Gamma(t \to Wb)$ the theoretical partial decay width for the decay into Wb. The value of the partial decay width is obtained as before but restricted to the decay $t \to Wb$ – resulting in an additional factor of $|V_{tb}|^2$ due to the Wtb vertex.
Due to the Standard Model prediction for the cross-section being included, the measured width can only be interpreted as the decay width of the top-quark if the Standard Model is indeed correct. Nonetheless, a deviation from the predicted value would indicate physics beyond the Standard Model.

Indirect measurements of Γ_t have been performed by the D0 collaboration at the Tevatron [25] and the CMS collaboration at the LHC [26]. The former obtained a value of

$$\Gamma_t^{\mathrm{D0}} = 2.00^{+0.47}_{-0.43}\,\mathrm{GeV} ,$$

while the latter obtained a value of

$$\Gamma_t^{\mathrm{CMS}} = 1.36 \pm 0.02(\mathrm{stat.})^{+0.14}_{-0.11}(\mathrm{syst.})\ \mathrm{GeV}\ .$$

Both measurements are in agreement with the Standard Model prediction. Even though the result obtained by the CMS collaboration is significantly more precise, the relative uncertainty is still $\sim 10\,\%$. Therefore, one is not yet sensitive to small corrections of the decay width which could be caused by physics beyond the Standard Model.

In a **direct measurement**, the decay width is extracted directly from the differential cross-section $\mathrm{d}\sigma/\mathrm{d}m_t$ similar to the measurement of the Z boson decay width at e^+e^- colliders. This yields a model independent result which can be used to infer on physics beyond the Standard Model. Unfortunately, the distribution in the observed top-quark mass is dominated by resolution effects which exceed the effect of the decay width on the shape of the distribution. This significantly reduces the precision of a direct measurement and coping with the large uncertainty when extracting the decay width is the main challenge in such measurements.

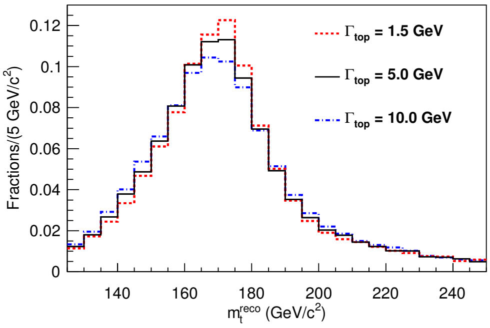

Fig. 2.8: Reconstructed m_t distribution from CDF measurement [27] for different Γ_t.

The most precise value obtained in a direct measurement has been measured by the CDF collaboration at the Tevatron [27]. Figure 2.8 shows the reconstructed m_t^{reco} distribution taken from simulations for different values of Γ_t. Due to the energy resolution of the detector, the width of the observed distribution is much larger than the expected decay width of the top-quark. Changing the value of the decay width by one order of magnitude only slightly changes the shape of the distribution. The value for the decay width is extracted by performing a template fit to the distribution in m_t^{reco}. The following limits are set:

$$1.10\,\mathrm{GeV} < \Gamma_t^{\mathrm{CDF}} < 4.05\,\mathrm{GeV}\ (@68\%\ \mathrm{C.L.})\ .$$

Compared to the indirect measurement performed by the D0 collaboration, which uses a dataset of approximately the same size, the precision of the direct measurement is significantly worse. Nonetheless, this thesis discusses studies and expected statistical uncertainties towards a direct measurement of the top-quark decay width at the ATLAS experiment, making use of the much larger number of top-quark events produced at the LHC.

2.3 Monte Carlo Event Generation

The here presented proof-of-concept studies use simulated events to investigate the prospects of a fiducial $\mathrm{d}\sigma/\mathrm{d}m_t$ and decay width measurement. Therefore, this section will give a brief description of the different steps performed in the generation of events. It goes without saying that a detailed discussion is not possible within this context and hence Reference [28] should be consulted for those details.

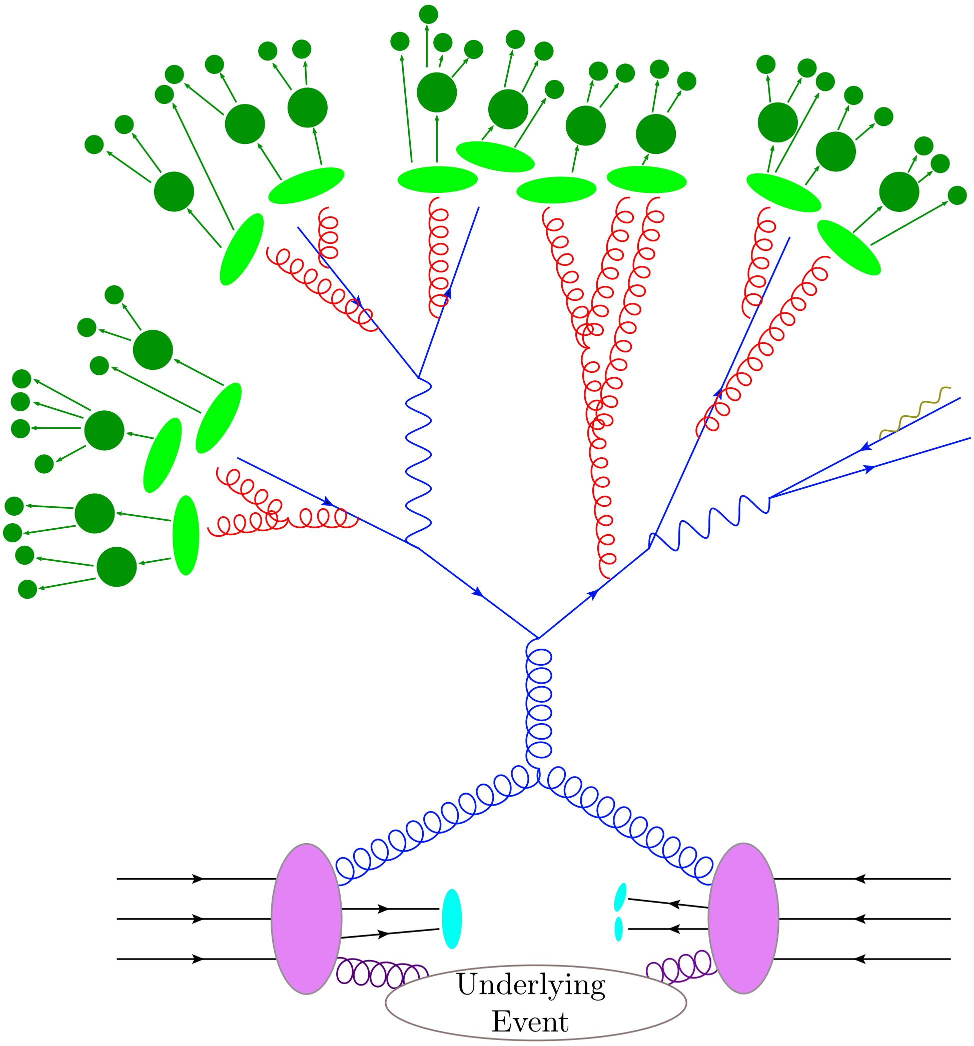

Fig. 2.9: Illustration of the different stages in the Monte Carlo event generation for a $gg \to t\bar{t} \to bW^+\bar{b}W^- \to bq\bar{q}'\bar{b}l^-\nu$. The colliding protons are shown in purple, the hard process in blue and the parton shower in red. The hadronisation is illustrated in light green while the resulting hadrons are represented by dark green.

Figure 2.9 shows a schematic illustration of the evolution of a simulated event. From each of the colliding protons, an interacting parton is chosen taking the parton density functions into account. The remnants of the proton will participate in the underlying event while the chosen partons initiate the hard process shown in blue. The hard process is described by a matrix element and typically contains the interesting physics effects studied in almost all analyses. The particles, their energies and momenta in one simulated event are taken from one phase-space point in the Monte Carlo integration of the integrals in Equation 2.2

after weighting with the matrix element.
Similar to QED bremsstrahlung leading to the emission of additional photons, QCD radiation has to be modelled to correctly describe the real processes. In principal, this additional radiation could also be described by the matrix element and hence be included in the hard process. In practice, this is unfortunately hardly ever possible due to technical and computational limitations. Nonetheless, modern event generators allow to add a few additional partons in the matrix element which should improve the precision of the results. Different numbers of additional partons will be taken as an example in this thesis to illustrate the model testing capabilities of a fiducial measurement of the $t\bar{t}$ cross-section.
The majority of the radiation is added using parton shower simulations which also decrease the momentum transfer scale from a very high scale in the hard process down to the scale at which hadrons form. The result of the parton shower is a large number of quarks and gluons depicted in red in Figure 2.9.
Using a hadronisation model, those quarks and gluons form hadrons. Such a model typically identifies subsets of all quarks and gluons which are close to each other and net no colour charge. Depending on their composition, the subsets are then replaced by multiple hadrons. These hadrons then decay further into particles stable enough to be measured by the detectors. In Chapter 5, these stable hadrons will be used to build the objects for the fiducial measurement.

The result of the event generation can then be passed to a simulation of the detector geometry such that the simulation describes the actual data. For these studies, the simulated detector is the ATLAS detector at the Large Hadron Collider, both of which are going to be discussed in the next chapter.

3 Experimental Setup

This chapter describes the experimental setup used in the analysis. The first section describes the Large Hadron Collider while the second section focusses on the ATLAS detector.

3.1 The Large Hadron Collider

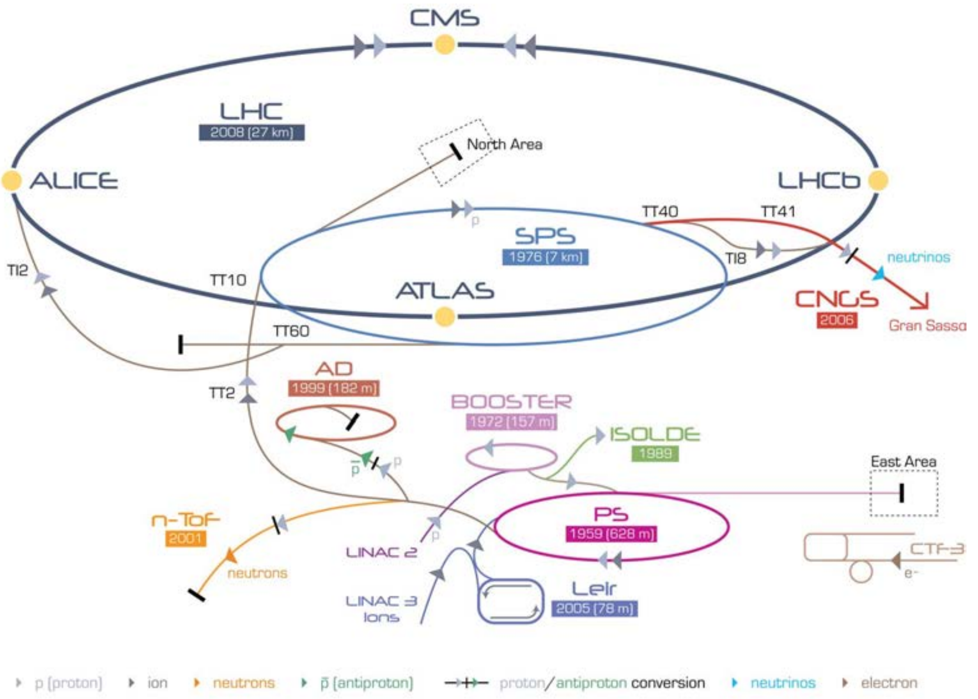

Fig. 3.1: Overview of the CERN accelerator complex [29].

The LHC [30] is located at the CERN research center close to Geneva at the Franco-Swiss border. With a circumference of 27 km, it is the largest as well as the most powerful particle accelerator in terms of centre-of-mass energy between the accelerated particles ever built by humankind. It was originally designed to accelerate protons to an energy of 7 TeV resulting in collisions at a centre-of-mass energy of 14 TeV. It was first operated at 3.5 TeV beam energy from 2010 to 2012 followed by a data taking period at a collision energy of 8 TeV until early 2013. After an upgrade-phase, the LHC is scheduled to restart in 2015 with a new data-taking period at a centre-of-mass energy of 13 TeV before being ramped up to its design value of 14 TeV. The LHC is also able to accelerate lead ions in order to study the physics in proton-lead and lead-lead collisions. However, this mode is not adressed in this analysis and thus not discussed in further detail. The protons are extracted from a hydrogen source after stripping off the electrons and bunched together. Before those protons are injected into the LHC, they pass through a chain of accelerators [31] which is depicted in Figure 3.1. The first accelerator, Linac 2, accelerates the protons to an energy of 50 MeV. These protons are then injected into the Proton Synchrotron Booster which raises the energy to 1.4 GeV, followed by the Proton Synchrotron which increases it up to 25 GeV. Upon injection into the main LHC ring, the protons have an energy of 450 GeV after passing the Super Proton Synchrotron. In the main ring, they are further accelerated until they reach their nominal energy of 4 TeV (in case of 8 TeV collision energy). The entire acceleration process takes about 20 minutes. However, once the protons reached their nominal energy, they can be stored in the main ring for several hours while the experiments located at the LHC take data.

The actual acceleration of the protons is done by using electromagnetic fields within a high-vacuum beam pipe. Since time-constant fields cannot reach gradients which are large enough, radio-frequency cavities creating a time-oscillating field are used. Therefore, particles are present in bunches of $\sim 10^{11}$ particles whose revolution frequency is synchronised with the frequency of the electric field such that they pass the cavities during an acceleration phase. Because both beams consist of positively charged particles, they are kept in separate beam pipes which only intersect in the interaction points where the different experiments are located. Up to 2800 bunches are present in each beam, achieving a bunch crossing rate at the interaction points of about 40 MHz.

Superconducting dipole magnets with fields up to 8 T are used to keep the protons on a circular orbit. In addition, quadrupole magnets are employed to focus the beam in the plane transverse to the beam direction. Focussing the beam in the interaction point increases the probability for proton-proton interactions to occur. Additionally, sextupole magnets are used to correct for dispersion effects due to different bending and focussing of particles having slightly different momenta [32].

Besides the centre-of-mass energy, the luminosity is another important quantity to characterise the collider. It can be calculated from the beam parameters of the collider:

$$\mathcal{L} = \frac{1}{4\pi} \cdot \frac{N_1 N_2 f N_b}{\sigma_x \sigma_y} \qquad \left[\frac{1}{\mathrm{cm}^2\mathrm{s}}\right] ,$$

where N_1 and N_2 are the number of particles in the colliding bunches, f is the revolution frequency of about 11 kHz and N_b is the number of bunches. σ_x and σ_y describe the beam profile in the transverse plane under the assumption of a Gaussian shape. This instantaneous luminosity relates the rate of events $\dot{N}$ to the cross-section σ of a certain process:

$$\dot{N} = \mathcal{L}\sigma \ .$$

The instantaneous luminosity can also be measured by counting the rate of a process with a well-known theoretical value of the cross-section. The time-integrated luminosity is a measure of the total collected data. The development of the integrated luminosity which has been measured by the ATLAS experiment is shown in Figure 3.2.

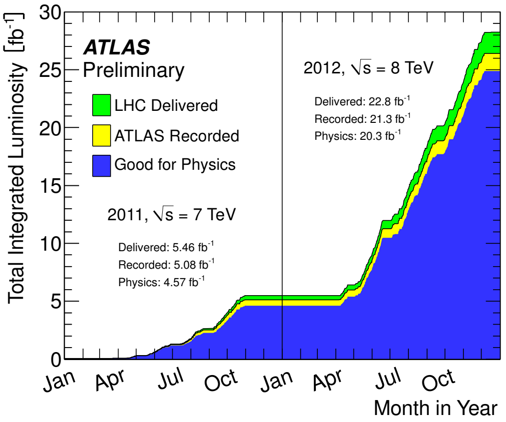

Fig. 3.2: Total integrated luminosity for the ATLAS detector until 10.3.2014 [33].

Besides the ATLAS experiment, which is a multi-purpose detector with a wide-ranging physics program, the LHC provides particle collisions for three additional major experiments. The CMS experiment [34] is also a multi-purpose detector and follows a similar physics program. The LHCb experiment [35] focusses on physics involving b-quarks and the study of $\mathcal{CP}$ violation. Lastly, the ALICE [36] experiment studies the collisions of lead ions, especially the produced quark-gluon plasma.

3.2 The ATLAS Detector

The ATLAS detector [37] has a cylindric shape around the LHC beam axis. The interaction point is in the centre of the detector, allowing a coverage of nearly the entire solid angle of 4π. The detector has a diameter of 25 m, a length of 44 m and a total weight of 7000 tonnes. It consists of different layers of subdetectors which are each optimised to fulfill their specialised roles and measure certain types of particles and their properties. Figure 3.3 shows the cylindric layers of the different subdetectors which will be described further in this section.

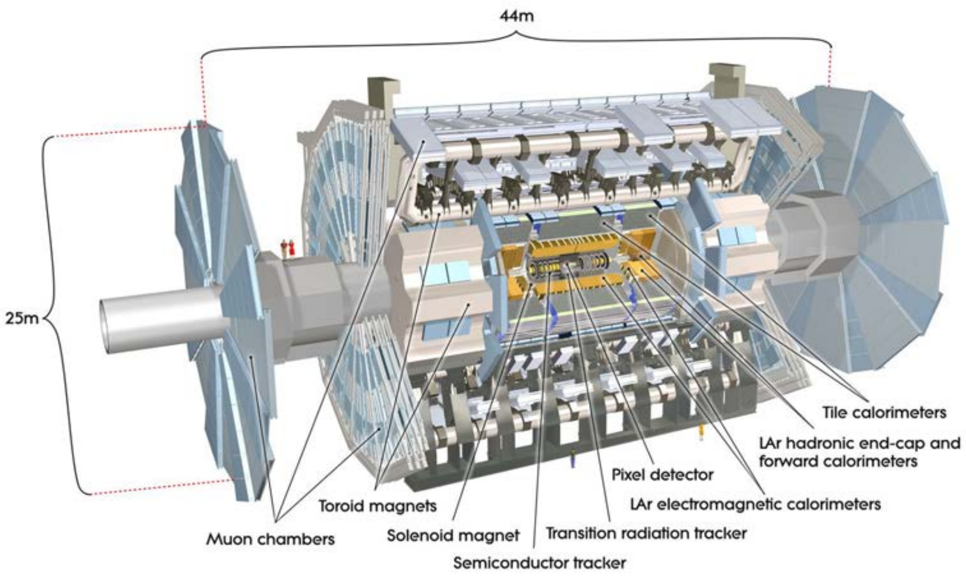

Fig. 3.3: Schematic overview of the ATLAS detector showing its different layers [38].

3.2.1 The Coordinate System

The ATLAS collaboration uses a right-handed coordinate system with the z-axis pointing along the beam axis, the x-axis being directed towards the center of the main accelerator ring and the y-axis pointing upwards. Each particle is described by a four-momentum vector that contains the energy E and the spatial momentum $\vec{p} = \left(p_x, p_y, p_z\right)$ of the particle:

$$p = \left(E \ , \ p_x \ , \ p_y \ , \ p_z \right) \ .$$

The angle ϕ is measured with respect to the positive x-axis in the plane perpendicular to the beam axis while the angle θ is the one between the particle's direction and the positive z-axis. The transverse momentum p_T is defined as:

$$p_T = \sqrt{p_x^2 + p_y^2} \ .$$

Instead of the angle θ, the pseudorapidity η is often used to describe the angle of a particle with respect to the beam axis:

$$\eta := -\ln\left[\tan\left(\frac{\theta}{2}\right)\right] = \frac{1}{2}\ln\left[\frac{|\vec{p}| + p_z}{|\vec{p}| - p_z}\right] \ .$$

The Cartesian coordinates can be expressed via the following equations:

$$\begin{aligned} p_x =& p_T \cos\phi \ , \\ p_y =& p_T \sin\phi \ , \\ p_z =& p_T \sinh\eta \ . \end{aligned}$$

A frequently used quantity to describe the distance of particles in the detector is $\Delta R = \sqrt{\Delta\eta^2 + \Delta\phi^2}$, where $\Delta\eta$ and $\Delta\phi$ are the differences of the particle's angles ϕ and pseudorapidities η, respectively.

3.2.2 The Inner Detector

The inner detector is located closest to the beam pipe and shown in Figure 3.4. The main purpose of the inner detector is the tracking of charged particles and subsequent vertex measurements. Charged particles created in the interaction produce charges by ionisation of the material while traversing the different subcomponents of the inner detector. Being closest to the beam pipe, the pixel detector is traversed first, followed by the semiconductor tracker (SCT) and the transition radiation tracker (TRT). Each of the subcomponents is present as a barrel and end-cap version as depicted in Figure 3.4a. In total, the inner detector can track particles within $|\eta| \leq 2.5$. Furthermore, it is immersed in a 2 T magnetic field created by a solenoid magnet bending the trajectories of charged particles with a curvature depending on the particle's momentum. Therefore, the inner detector can also

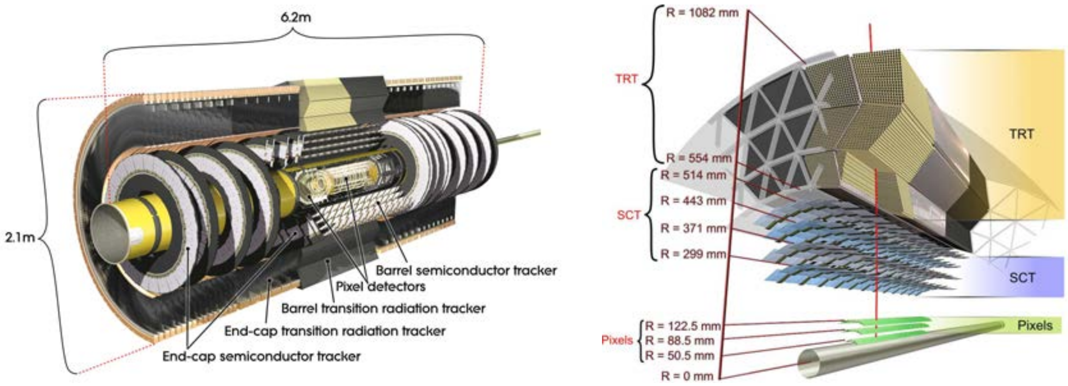

(a) Total inner detector (b) Barrel region

Fig. 3.4: Schematic overview of the ATLAS inner detector showing the different subcomponents. Figure 3.4a shows both the barrel region with a cylindrical ordering of the pixel detector, the semiconductor and the transition radiation tracker as well as the end-cap region where the subcomponents are ordered in disks. Figure 3.4b focusses on the barrel region and states the distances of the different layers to the beam pipe.

measure the particle's momentum.

The pixel detector consists of $50 \times 400\,\mu\mathrm{m}^2$ silicon pixels ordered in three layers as shown in Figure 3.4b. This results in more than 80 million read-out channels. The pixel detector is a crucial part of the ATLAS detector needed to precisely locate vertices in an event. Especially the correct identification of secondary vertices is necessary to identify heavy flavour jets and is greatly beneficial for top-quark analyses.

The semiconductor tracker is similar to the pixel detector, but uses silicon strips instead of pixels. This allows the coverage of a larger area and thus the SCT is placed further away from the beam pipe. In total, there are eight layers of silicon strips which are grouped in pairs of two. The layers in each of these pairs are placed in very close proximity and skewed with respect to each other to achieve a two dimensional resolution in η-ϕ.

The transition radiation detector consist of 7 m long and 2 mm wide straw tubes filled with gas. A wire is placed in the centre alongside the tube and acts as an electrode while the exterior of the tube provides the second electrode. Therefore, the charge deposited in one of the tubes can be measured. Furthermore, several materials with different dielectric constants are placed between the tubes. This leads to the emission of measurable amounts of transition radiation which is detected by the straw tubes [39]. The emitted radiation is characteristic for the type of particle which traversed the TRT and so is the resulting amount of charge deposition. As a consequence, the transition radiation tracker is used to differentiate between different kinds of particles, especially electrons and light hadrons.

3.2.3 The Calorimeters

The energy of almost all particles – with the exception of muons, neutrinos and possible unknown particles – is measured in the electromagnetic and hadronic calorimeter. Both are so called sampling calorimeters which consist of high density absorber material interleaved by an active medium. The energy of a particle is determined by completely stopping it within the calorimeter and measuring the total deposited energy. The deposited energy is obtained from the total charge that has been deposited in the active material. Electromagnetically interacting particles will undergo bremsstrahlung and pair-creation, and hence form an electromagnetic shower. This shower ionises the active medium resulting in a measurable charge. Hadrons passing the absorber material interact strongly with the nuclei of the material resulting in a particle shower that will further deposit charge. However, being only able to register charge deposition in the active material, ionisation in the absorber as well as neutral particles are not registered. Therefore, the deposited charge has to be carefully calibrated to the energy of the incident particle. The uncertainty of this calibration and the resulting difference between the real detector and detector simulations is a major source of systematic uncertainty in analyses involving jets. The effect of one of these uncertainties will also be evaluated in the analyses presented here.

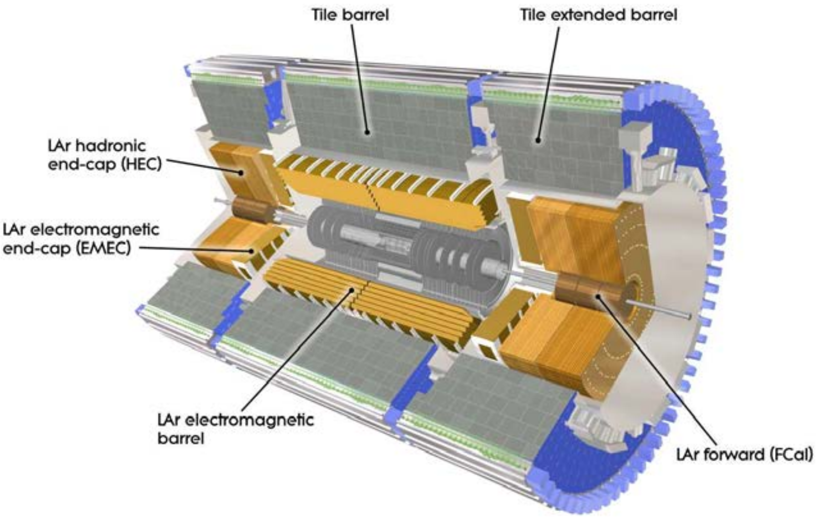

Fig. 3.5: Schematic overview of the ATLAS calorimeter system showing both the electromagnetic and hadronic calorimeters.

Figure 3.5 shows a schematic overview of the ATLAS calorimeter system. The electromagnetic calorimeter covers a range of $|\eta| < 3.2$ and consists of lead absorber plates which are interleaved by liquid argon as the active medium.

The hadronic calorimeter is comprised of absorber plates interleaved by plastic scintillators. In the barrel region, $|\eta| < 1.7$, iron plates are used as absorber while copper with liquid argon as sampling medium are used in the end-cap region $1.5 < |\eta| < 3.2$ and high density copper and tungsten are used closer to the beam axis ($3.1 < |\eta| < 4.9$) in order to improve the radiation hardness.

3.2.4 The Muon System

As mentioned before, muons are one of the few types of particles that are not stopped in the calorimeters. This is because muons are minimal ionising particles which traverse the inner parts of the detector with only a very small energy deposition. Therefore, the calorimeters are surrounded by the muon spectrometer whose sole purpose is the identification of muons

and the measurement of their momentum. To fulfil the latter task, the muon spectrometer is immersed in a 4 T magnetic field generated by a toroidal magnet. The muon track is reconstructed from hits in monitored drift tubes and cathode strip chambers.
As the presence of muons in an event indicates possibly interesting events for later analysis, the muon spectrometer also comprises fast resistive plate chambers and thin gap chambers. These are used as a trigger signal for the trigger system, which is described in the following.

3.2.5 The Trigger System

To decide which events should be recorded for later analysis, several trigger systems are each organised in different levels. These triggers are designed to trigger on potentially interesting events by studying certain characteristics, e.g. a muon with a large momentum. Each level of the trigger has to process less events than the previous one thus giving it more time to apply more complex algorithms to identify interesting events. These triggers are necessary because the permanent storage requirements which would be needed to store every event exceed technically possible rates by several orders of magnitude.
The ATLAS trigger system is comprised of three different levels. The first level (L1) is a hardware-based trigger and quickly decides whether an event is potentially interesting based on rough criteria and the information provided by the calorimeters and the muon system. The second level (L2) and the event filter (EF) are both software-based and employ the information from all subdetectors to refine this decision. While the EF trigger takes the entire detector into account, the L2 trigger focusses on Regions of Interest (RoI) previously identified by the L1 trigger. As both have significantly more time to process a single event due to L1's preselection, more complex algorithms can be used. Hence, they are also referred to as high level triggers (HLT).
Figure 3.6 shows a schematic overview of the ATLAS trigger system including the average decision times per trigger level and the resulting event rates.

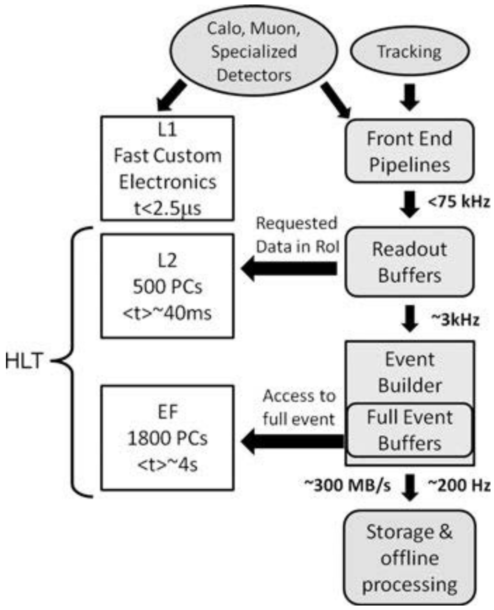

Fig. 3.6: Schematic of the ATLAS trigger system. [40]

4 Unfolding

Despite the effort which is undertaken to optimise and constantly improve the ATLAS detector, it is unavoidable – as for any other device used in measurements – that the measurement itself affects the result of the measurement. The correction for these uncertainties in the analyses can be straight forward in case of effects which apply a constant deviation on the result of the measurement and can be corrected on an event-by-event basis. While this is true for some, many sources of uncertainty introduce a statistical deviation and no per-event correction is possible. Nonetheless, the measured spectrum of a quantity is given by the convolution – also called *folding* – of the true spectrum and the probability density function describing the statistical effect on the observable. The inverse process, which is called *unfolding*, can be used to deduce the true spectrum from the measured one as discussed in this section.

In the following, a variable x refers to a one-dimensional quantity which can be estimated per event while $\vec{x}$ refers to the distribution of this quantity described by a histogram and treated as a vector. Capital letters refer to matrices and X represents the covariance matrix between the bins whose contents are given by $\vec{x}$.

4.1 Problem of Unfolding

Let t be the true value of an observable, e.g. the mass of the top quark or the transverse momentum of a particle. It is distributed according to a probability density function $f(t)$ (e.g. a Breit-Wigner distribution in case of a particle's mass). Furthermore, let r be the measured observable which is itself distributed according to $g(r)$. In the unfolding, one assumes that for every t there is a measured value r and vice versa.[1] Furthermore, let $p(r|t)$ be the probability for measuring r given a certain t (where t takes the role of a parameter instead of a random variable described by p). It is often referred to as the *response* of the device. The relationship between the different distributions is

$$g(r) = \int p(r|t) f(t) \mathrm{d}t \ . \tag{4.1}$$

---

[1] Efficiencies can be included as corrections factors after the unfolding is performed.

The interchanged relationship holds as well:

$$f(t) = \int p(t|r)g(r)\mathrm{d}r \ . \tag{4.2}$$

It becomes clear that knowing $p(t|r)$ would solve the problem of unfolding and Equation (4.2) would immediately yield the desired $f(t)$. However, the main challenge in using unfolding is to actually estimate $p(t|r)$. While $p(r|t)$ – as a conditional probability density function with t being the independent parameter – does not actually contain any information about the distribution of t itself (that is the reason why $f(t)$ had to be included explicitly in Equation (4.1)), this is not true for $p(t|r)$. By using Bayes' theorem one can rewrite $p(t|r)$:

$$p(t|r) = \frac{p(r|t)}{g(r)}f(t) \ . \tag{4.3}$$

Therefore, $p(t|r)$ cannot be constructed from the knowledge of $p(r|t)$ alone. Before a possible strategy to approximate $p(t|r)$ is presented, the above considerations are translated to a realistic use-case with a finite number of measurements in which the probability density functions are approximated as histograms.

Due to the finite number of observable events, the true observable t is binned into N bins of size Δt_i while the reconstructed observable r is binned into M bins of size[2] Δr_j. Therefore, the *response* of the device used for the measurement can be described in matrix form – the so called *response matrix*:

$$\hat{A}_{ij} = p\big(r \in \Delta r_i | t \in \Delta t_j\big) =: p\big(r_i|t_j\big) \ ,$$

is the probability of reconstructing an event in the i-th bin of the measured histogram while the true value lies in the j-th bin of the true histogram. The response matrix is typically obtained by generating a large number of Monte Carlo events with both the true value t and the reconstructed value r of the observable. The response matrix is then obtained by interpreting the two dimensional histogram A in t and r as a conditional probability density function and normalising the one-dimensional slices in r with constant t. Analytically, this probability is obtained by integrating the response in both dimensions:

$$\hat{A}_{ij} = p\big(r \in \Delta r_i | t \in \Delta t_j\big) = \frac{\int_{\Delta r_i}\int_{\Delta t_j} p(r|t)f(t)\mathrm{d}r\mathrm{d}t}{\sum_{i'=1}^{M}\int_{\Delta r_{i'}}\int_{\Delta t_j} p(r|t)f(t)\mathrm{d}r\mathrm{d}t} \ .$$

A problem when dealing with binned data in unfolding is evident: as the response of the measurement $p(r|t)$ is not a probability density function in t, one has to include $f(t)$ in order to calculate the response matrix. In case the response matrix is taken from Monte Carlo simulations, one introduces a dependency on the true distribution. This can lead to

---

[2] If the most general case of $M \geq N$ and $\Delta r_i \neq \Delta t_i \, \forall i$ is applicable depends on the used unfolding technique.

a bias in any measurements using the unfolded distribution which has to be checked. This effect can be reduced by choosing small Δt such that $f(t)$ is almost constant within each bin.

In terms of histograms described by vectors, the true $\vec{t}$ and measured distributions $\vec{r}$ are now related by a linear transformation:

$$\vec{r} = \hat{A} \cdot \vec{t} \,. \tag{4.4}$$

The goal of unfolding is to solve this equation by estimating $\vec{t}$ for a given measured distribution $\vec{r}$ and known response matrix $\hat{A}$. In the following sections, the aspect common to all approaches on how to estimate $\vec{t}$ is presented. This is followed by a discussion of unfolding using singular value decomposition – the method used in this analysis.

4.2 Regularisation

The most obvious approach on how to estimate $\vec{t}$ is the multiplication of Equation (4.4) with the inverse $\hat{A}^{-1}$:

$$\vec{t} = \hat{A}^{-1} \cdot \vec{r} \,. \tag{4.5}$$

However, doing this strongly amplifies statistical fluctuations in the measured distribution which yields a highly fluctuating distribution in the estimated true value with high correlations between its bins (see example in [41]). An example for this effect will also be given in Section 9.1. Any meaningful method of unfolding has to account for this effect and separate these contributions due to statistical fluctuations from the main components of the distributions describing its shape. This is typically referred to as *regularisation*. The impact of the regularisation on the unfolded distribution and the subsequent analysis has to be thoroughly checked: regularisation is an external constraint imposed on the problem and the parameters tuning its behaviours can – in principal – be chosen arbitrarily. Therefore, regularisation can introduce a bias to the analysis which has to be evaluated carefully.

4.3 Singular Value Decomposition

In this approach, singular value decomposition is used to rank the different contributions to the unfolded distribution and suppress the ones caused by statistical fluctuations. The method was first proposed by Höcker and Kartvelishvili [41]. Singular value decomposition is related to the determination of the eigenvalues and eigenvectors of quadratic matrices but can be applied to a general real $M \times N$ matrix A leading to the factorisation:

$$\underset{M\times N}{A} = \underset{M\times M}{U} \cdot \underset{M\times N}{S} \cdot \underset{N\times N}{V^T} \,.$$

Here, S is a – similar to the eigenvalue problem – diagonal matrix whose diagonal elements are the singular values of A and fulfill $S_{ii} > 0 \, \forall \, i$. Both matrices U and V^T are orthogonal and their columns give the left and right singular vectors of the decomposition. Without loss of generality, the singular values can be ordered in a non-increasing order by swapping corresponding singular vectors in U and V^T respectively.

4.3.1 Description of the Method

The first step is the interpretation of the unfolding problem as a χ^2 minimisation problem:

$$\chi^2 = (\hat{A}\vec{t} - \vec{r})^T R^{-1} (\hat{A}\vec{t} - \vec{r}) \ . \tag{4.6}$$

Minimising the χ^2 still leads to the exact but unwanted solution given by Equation (4.5). In the next step, the unknown is rescaled by dividing it component-wise by the true distribution $\vec{t}^{ini}$ which is used to obtain the response matrix $\hat{A}$ in Monte Carlo simulations:

$$\sum_{j=1}^{N} \hat{A}_{ij} t_j = \sum_{j=1}^{N} \hat{A}_{ij} t_j^{ini} \underbrace{\frac{1}{t_j^{ini}} t_j}_{\omega_j} = \sum_{j=1}^{N} A_{ij} \omega_j \ ,$$

where A is again the two dimensional histogram filled in a Monte Carlo simulation before it is normalised to obtain $\hat{A}$. For any reasonable initial guess for $\vec{t}^{ini}$, the new unknown $\vec{\omega}$ should be a smooth distribution which is a crucial part for the later introduced regularisation. Furthermore, one uses singular value decomposition to simplify the χ^2 by decomposing the covariance matrix R of the measured distribution. Being a symmetric matrix, its decomposition is given by:

$$R = QKQ^T \qquad \rightarrow \qquad R^{-1} = QK^{-1}Q^T \ .$$

Inserting this into Equation (4.6) and defining a modified matrix A' and a vector of measured values $\vec{r}'$ given by

$$A'_{ij} = \frac{1}{R_{ii}} \sum_{m=1}^{M} Q_{im} A_{mj} \qquad \text{and} \qquad r'_i = \frac{1}{R_{ii}} \sum_{m=1}^{M} Q_{im} r_m$$

yields the modified χ^2 minimisation problem:

$$\chi^2 = (A'\vec{\omega} - \vec{r}')^T (A'\vec{\omega} - \vec{r}') \ . \tag{4.7}$$

By performing these transformations, the covariance matrix of the $\vec{r}'$ is the unit matrix I, which will have an important consequence when tuning the parameter that will steer the regularisation. Nonetheless, the modified χ^2 is – in principal – still the same as in equation (4.6) and hence is still affected by the problem of enhancing statistical fluctuations in the measurement. In order to reduce the fluctuations, one introduces a regularisation scheme to the χ^2 problem which prefers smooth solutions when minimising the equation (4.7). The method presented here uses the so called Tikhonov regularisation [42] which minimises the second derivative of the unknown $\vec{\omega}$ in an inverse problem. In the binned case discussed here, the second derivative can be written as

$$\sum_i [(\omega_{i+1} - \omega_i) - (\omega_i - \omega_{i-1})]^2 \ .$$

Therefore, the final χ^2, after adding this additional constraint, reads

$$\chi^2_\tau = (A'\vec{\omega} - \vec{r}')^T (A'\vec{\omega} - \vec{r}') + \tau \cdot (C\vec{\omega})^T (C\vec{\omega}) \ , \tag{4.8}$$

where C is the matrix representation of the Tikhonov regularisation given by

$$C = \begin{pmatrix} -1 & 1 & 0 & & & \\ 1 & -2 & 1 & & & \\ 0 & 1 & -2 & & & \\ & & & \ddots & & \\ & & & & -2 & 1 \\ & & & & 1 & -1 \end{pmatrix}$$

and τ the regularisation parameter controlling the strength of the regularisation. This parameter depends on the actual problem and can vary for each A. In case the value of τ is chosen to be very low, the effect of the regularisation is negligible and the obtained result of the minimisation is again essentially equal to the exact solution in Equation (4.5). In contrast, if τ is chosen too large, the result of the minimisation is predominantly determined by the regularisation term in Equation (4.8), resulting in the obtained unfolded spectrum being forced towards the Monte Carlo input $\vec{t}^{ini}$ and significant contributions not stemming from statistical fluctuations being removed. The effect of different values for τ when applying unfolding during this analysis will be discussed in Section 9.1.

In order to understand the effect of the regularisation and to find a strategy to identify the optimal value for τ, one has to further solve the system. Minimisation of χ^2_τ leads to a new system of equations:

$$\begin{bmatrix} A' \\ \sqrt{\tau}C \end{bmatrix} \vec{\omega} = \begin{bmatrix} A'C^{-1} \\ \sqrt{\tau}I \end{bmatrix} C\vec{\omega} = \begin{bmatrix} \vec{r}' \\ 0 \end{bmatrix} \ . \tag{4.9}$$

In order to be able to calculate C^{-1}, a small value has to be added to the diagonal of C. Before deriving a solution for the general system, a solution for the special case of $\tau = 0$ is obtained by applying the singular value decomposition to obtain $AC^{-1} = USV^T$. Substituting this into Equation (4.9) leads to

$$USV^T \cdot C\vec{\omega} = \vec{r}' \quad \Leftrightarrow \quad S \cdot \underbrace{V^T\vec{\omega}}_{\vec{z}} = \underbrace{U^T\vec{r}'}_{\vec{d}} \quad \Leftrightarrow \quad S\vec{z} = \vec{d} \ .$$

The new unknown $\vec{z}$ and the rotated measured value $\vec{d}$ are now connected by a diagonal matrix and the solutions for $\vec{z}$ can be trivially determined to be $z_i^{(0)} = d_i/S_{ii}$. It is important to note that the d_i are the coefficients of the different, orthogonal contributions to the measured distribution given by the columns of U. Due to $\vec{d}$ being obtained by rotating $\vec{r}'$, its covariance matrix D is also equal to the unit matrix. Nonetheless, to obtain a proper solution for the unfolding, one has to take the regularisation into account and solve for $\tau \neq 0$. It can be shown that this can be done by replacing all $\vec{d}$ by

$$d_i^{(\tau)} = d_i \frac{S_{ii}^2}{S_{ii}^2 + \tau} \quad \Rightarrow \quad z_i^{(\tau)} = d_i \frac{S_{ii}}{S_{ii}^2 + \tau} \tag{4.10}$$

which leads to the modified solution $z_i^{(\tau)} = d_i^{(\tau)}/S_{ii}$ which is also dependent on the regularisation parameter τ as expected. Remember that the S_{ii} are in decreasing order: for the first few terms in the decomposition and a chosen τ, one finds $S_{ii}^2 \gg \tau$ and thus $d_i^{(\tau)} \approx d_i$. However, for the latter terms, the coefficients are dampened yielding $d_i^{\tau} \approx 0$ and thus excluding these contributions from entering the solution $\vec{z}$.

4.3.2 Unfolded Distribution and Covariance

After obtaining the solution $\vec{z}$ as described above, the true distribution $\vec{t}$ can be estimated by reverting the rotation and scaling:

$$\vec{\omega} = C^{-1} V \cdot \vec{z} \quad \Rightarrow \quad t_i = t_i^{ini} \cdot \omega_i \ .$$

One benefit of the unfolding method is the straight forward calculation of the uncertainties. As the covariance matrix of $\vec{d}$ is known to be the unit matrix, the covariance matrix for $\vec{z}^{(\tau)}$ is obtained directly from Equation (4.10) by propagating the uncertainty:

$$Z_{ik}^{(\tau)} = \begin{cases} \frac{S_{ii}^2}{(S_{ii}^2+\tau)^2} & i = k \\ 0 & i \neq k \end{cases}$$

The covariance matrix for $\vec{\omega}$ and eventually $\vec{t}$ can be obtained by transforming $Z^{(\tau)}$:

$$W^{(\tau)} = C^{-1} V \cdot Z^{(\tau)} \cdot \left(C^{-1} V\right)^T \quad \Rightarrow \quad T_{ik}^{(\tau)} = t_i^{ini} W_{ik}^{(\tau)} t_k^{ini} \ .$$

The analysis described in this thesis uses the `RooUnfold` [43] implementation of this unfolding method. All calculations and transformations are performed by the framework, the only necessary inputs are the measured distribution, the response matrix and the regularisation parameter τ. Therefore, one possible approach on obtaining the optimal value for τ is presented in the following.

4.3.3 Choosing a Regularisation Parameter τ

The optimal value for the regularisation parameter can be obtained by studying the coefficients d_i of the decomposed measured distribution. Significant contributions to the spectrum are expected to have a significant coefficient, meaning a value clearly different from zero when taking the known variance of one into account. In fact, the coefficients of contributions due to statistical fluctuations are expected to follow a unit Gaussian distribution.

Therefore, the optimal value for τ can be obtained by determining the index k such that the d_i for $i > k$ are in agreement with a unit Gaussian distribution. In Section 9.1, this will be visualised by plotting $\log|d_i|$ over i where the transition from the significant to non-significant contributions can be clearly seen. The value for τ is then determined by $\tau = S_{kk}^2$, which will dampen the effect of contributions with $i > k$ as seen in Equation (4.10).

Even though the most general implementation of the method can use any value for τ, the `RooUnfold` implementation used here automatically calculates τ for a provided value for k.

5 The Particle Level

The particle level is the ideal choice when performing a fiducial measurement. This chapter will argue why it yields measurements both independent of detector and modelling effects. Furthermore, the objects on this level are defined.

5.1 Motivation

The guiding principle of a fiducial measurement as presented here is obtaining a result independent of both the used detector and the modeling in the simulations needed to interpret the results. Therefore, the fiducial differential cross-section measurement can be directly compared to or combined with other such measurements done by different experiments. Additionally, the result does not become outdated in case of physical models being changed. Furthermore, different models can be tested by comparing them with the measured fiducial distribution without the need to include the detector effects in the predictions of the model.

The different stages of the evolution of an event are depicted in Figure 5.1. The hard process produces elementary particles which are the constituents of the *parton level*. The next step is the *particle level*, which refers to the state of the event after parton shower and the hadronisation. It is comprised of all particles which are stable enough to be measured directly by the detector. These are mainly stable hadrons like protons, neutrons, pions and kaons, the long lived charged leptons (electron and muon), neutrinos and photons.
Finally, the *reconstruction level* consists of the measured objects after the stable particles have traversed the detector. Conclusively, the only level which is experimentally accessible is the reconstruction level. Parton and particle level are only accessible in Monte Carlo simulations.

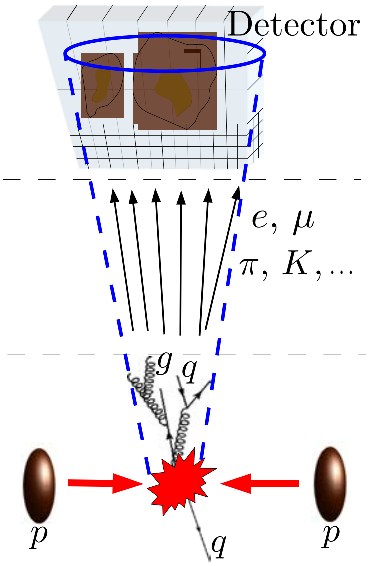

Fig. 5.1: Evolution of an event.

The actual measurement – which is always on reconstruction level – does not satisfy the requirements for a fiducial measurement as it is largely dependent on the used detector. Therefore, the measured distribution has to be corrected for the detector effects using unfolding. This raises the question as to which level in the evolution one wants to unfold

to: to the parton or particle level?
As one is interested in the differential cross-section with respect to the mass of a particle which occurs in the studied process, it seems intuitive to unfold down to this particle: the top-quark. However, like all other quarks, the top-quark cannot be observed. Quarks hadronise before they could ever reach any device capable of measuring them and top-quarks are expected to decay even before hadronisation takes place. Hence the invariant mass of the top-quark parton is an ill-defined observable from a physical point of view. Furthermore, the correction applied by unfolding would include not only effects due to the detector but also due to the models used for parton shower and hadronisation. Accordingly, the obtained result would indeed be independent of the used detector but dependent on those modeling effects.
Additionally, unfolding to the top-quark parton induces a number of technical problems one would have to deal with:

1. The reasonably good description of measured data using Monte Carlo simulations is based on particle shower and hadronisation simulations. Both are optimised to take the output of the parton level event generators and add radiation and hadronisation such that observed data is well described. There is no guarantee that the top-quark parton in the Monte Carlo simulation behaves the same as the one in reality. Furthermore, the result of the unfolding would strongly depend on the used Monte Carlo generator and parton shower simulation resulting in difficulties when comparing results obtained with different Monte Carlo generators.
2. There is no object corresponding to the top-quark parton on the reconstruction level. The measured jets and leptons would have to be combined in some way to form an observable. The combining procedure and its uncertainties would also be included in the response matrix and increase the complexity of the problem.

Concluding this discussion, in order to avoid all the problems and uncertainties with parton level observables, the analysis will use a well-defined top-quark on particle level. Consequently, the unfolding only corrects for detector effects as the level to which one unfolds is the one right before the detector. In the following section, the objects on the particle level will be defined.

5.2 Object Definition

This section describes the object definitions on particle level which are used in this analysis. As mentioned before, the particle level is comprised of all the particles that are stable enough to be detected. In a Monte Carlo simulation, this corresponds to the output which is passed to the detector simulation. This subset of all Monte Carlo particles is obtained by requiring the Monte Carlo status code being equal to one. The full Monte Carlo truth record is required in the following, including information on the ancestry of the particles.

Charged Leptons

Electrons and muons are the charged leptons which can be observed. Besides the signal process, electrons and muons can also stem from the decay of a hadron inside a jet. To identify the signal electrons and muons, one traces back the Monte Carlo ancestry and checks whether the particle stems from a hadron. In case it stems from the decay of a tau lepton, the ancestry of this tau lepton is studied. All identified signal charged leptons are *dressed* by adding photons within $\Delta R \leq 0.1$ to the lepton in order to incorporate QED final state radiation. Only photons which do not stem from jets are considered in the lepton dressing. This is again implemented by tracing back the Monte Carlo ancestry of the photon and verifying that it does not stem from a hadron.

Missing Transverse Momentum

The missing transverse momentum is given by the momentum which is necessary to ensure momentum conservation in the transverse plane. On reconstruction level this quantity is predominantly caused by neutrinos which cannot be detected with the ATLAS detector.[1] On particle level, one defines this quantity as the transverse component of the selected signal neutrinos. These signal neutrinos are identified in the same manner as the charged leptons. As the neutrinos do not interact electromagnetically, no photon dressing is performed.

Jets

Jets are constructed from all remaining stable particles which have not been selected when identifying the charged leptons and the missing transverse momentum. The jets are clustered by using the anti-k_t 0.4 [44] clustering algorithm. The identification of jets stemming from b-quarks, which is of utmost importance in measurements involving top-quarks, is done on reconstruction level by looking for a displacement of jets with respect to the primary vertex of the event. This is caused by b-quarks forming B hadrons which are relatively long-lived such that a measurable displacement can be observed before they decay and form a jet. To replicate this on particle level, one also includes B hadrons in the jet clustering which have decayed within the simulation (status code not equal to one). As their decay products are already included in the jet clustering and to avoid biasing the energy of the jet, their energy is scaled down to 10^{-5} GeV hence the B hadron will be included in the correct jet due to its direction without changing the jet itself. Jets which contain at least one of these B hadrons are then flagged as b-jets.

A Top-Quark Definition: Pseudo Tops

A definition of the top-quark on particle level is done similarly to the definition on reconstruction level by combining the previously defined objects to match the decay

---

[1] Objects outside of the detector acceptance are not reconstructed and thus also contribute to the missing transverse momentum.

signature of a top-quark. This analysis uses semileptonically decaying $t\bar{t}$ pairs with exactly one electron or muon in the final state. Typically, a kinematic likelihood fit [45] is performed to combine the objects and reconstruct a top-quark. In spite of the good performance of these methods, this analysis refrains from using a kinematic fit in the interest of retaining model independence.
In kinematic fits, one introduces corrections – so called transfer functions – down to parton level and constrains the kinematics of these partons to obtain the best jet-to-parton assignment. As discussed before, this analysis aims to avoid using any parton level information as bare quarks cannot serve as proper observables. In consequence, one uses an operational definition for top-quarks – the so called pseudo tops [46].

The definition for pseudo tops used here requires events which, in addition to having exactly one charged lepton, need to have at least two b-tagged jets and a minimum of four jets in total.
The pseudo tops are then constructed by taking the two leading b-jets in p_T and comparing their ΔR with respect to the charged lepton. The one which has the smaller value of ΔR is associated with the leptonically decaying pseudo top, the other one with the hadronically decaying one. The two jets stemming from the hadronically decaying W boson are taken to be the two leading in p_T of all remaining jets in the event.

5.3 Object and Event Selection

Besides requiring the minimal number of objects to use the definition for pseudo tops, it is not absolutely necessary to apply any further selection criteria on particle level. However, this leads to very small efficiencies to accept an event on reconstruction level for certain phase space regions of the detector. Particle level objects can be outside of the geometrical acceptance of the detector, or they are too soft and consequently not measured. Acceptance effects can be corrected by multiplying each bin i in the unfolded spectrum with the $1/\varepsilon_i$ where $0 \leq \varepsilon_i \leq 1$ is the efficiency to accept an event in this bin.
However, in phase space regions which are not accessible by the detector, the efficiencies will become small and their values mainly dependent on the modelling in the Monte Carlo sample being used for determining the efficiency. Hence the correction for the efficiency is also a model dependent extrapolation into unaccessible regions of the phase space, contradicting the guiding principle of a fiducial measurement of having a model-independent result. Consequently, a basic object and event selection is applied. The event selection criteria are explained in the following and have been chosen to approximately resemble the ATLAS acceptance neglecting special features of the detector. Therefore, the fiducial region defined in this manner can also be used by other experiments – for example the CMS experiment with a similar acceptance region.

The objects – electrons, muons and jets – are required to have a pseudorapidity of $|\eta| \leq 2.6$. This is slightly looser than the acceptance region of the inner detector in the ATLAS experiment but is chosen to reduce the number of events passing the reconstruction level but failing the particle level selection. For the same reason, they must have a transverse momentum of at least $p_T \geq 20\,\text{GeV}$, which is slightly looser than the requirement on reconstruction level described in Section 7.2. An event is selected on particle level if it fulfills the following criteria:

$n_{l^{\pm}} = 1$	exactly one charged signal lepton,
$n_{\text{jets}} \geq 4$	at least four jets in the event,
$n_b \geq 2$	of those, at least two have to be b-jets,
$\Delta R(l, \text{jets}) \geq 0.4$	overlap removal for each pair of jets and leptons.

In the following chapter, the object definitions and the selection criteria are applied to generated Monte Carlo samples and studies on the differential cross-section $\mathrm{d}\sigma/\mathrm{d}m_t$ on particle level are presented.

6 Particle Level Studies

In this chapter, the particle level definition presented in the previous chapter is used for the study of simulated $t\bar{t}$ events. The obtained distribution in m_t is studied in terms of its behaviour under the variation of the physical parameters predominantly describing its shape: the assumed width Γ_t and mass m_t of the top-quark. In the following, the studies focus on the pseudo top built from three jets. For simplicity, all observables of the hadronically decaying pseudo top are written with subscript t unless otherwise stated.

6.1 Monte Carlo Settings and Tools

The preliminary studies have been performed using Sherpa 2.1.0 [47]. The Catani-Seymour subtraction based shower [48] is used to shower the result of the Amegic [49] and Comix [50] matrix element interfaces. Matrix element merging with truncated showers [51] is applied and photons are handled by the Photons package [52].

The Sherpa matrix element generator is used to generate $t\bar{t}$ events with potentially one extra jet $pp \rightarrow t\bar{t}(j)$. The subsequent decays $t \rightarrow Wb$ and the decays of the W boson are factorised and treated by the hard decay handler in order to speed up the event generation by several orders of magnitude. Furthermore, the decays of the two W bosons are configured such that they produce $t\bar{t} \rightarrow b\bar{b}l\nu jj$ to avoid the generation of unnecessary events as they would fail an imposed selection criteria requiring events to have exactly one signal electron or muon. The contribution of $\tau\tau$ dilepton events with one tau decaying hadronically and one leptonically is deemed negligible and thus ignored here. The output of Sherpa is stored using HepMC 2.06.08 [53] which allows easy access to the Monte Carlo truth history. The jet clustering is done by using FastJet 2.0.4 [54, 55].

6.2 Consistency Checks and Event Selection

The particle level object definition described in Section 5.2 is applied to a sample with $m_t = 172.5\,\text{GeV}$ and $\Gamma_t = 1.3\,\text{GeV}$, which is generated according to the settings described in the previous section. In order to test the particle level definition in terms of its capability to identify the signal leptons correctly, no object and event selection is applied for now. Figure 6.1a shows the number of identified signal electrons and muons in the sample. The relative contributions exactly match the expectation if the possible decays of τ leptons in τ+jets events are taken into account.

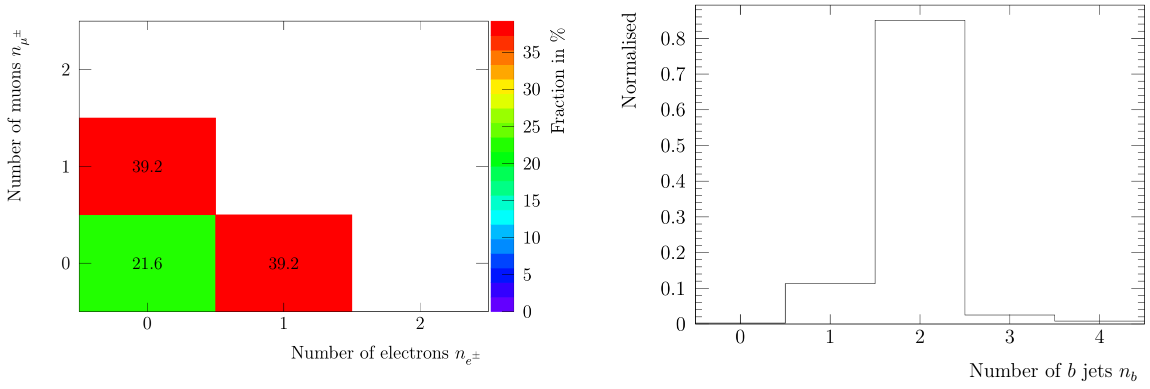

(a) Fraction of signal Leptons.

(b) Number of b-tagged jets.

Fig. 6.1: Number of particle level objects based on the definition in section 5.2 without applying any event selection. Plots are taken from a Sherpa sample with $m_t = 172.5$ GeV and $\Gamma_t = 1.3$ GeV.

The number of b-tagged jets – still without any event selection applied – is shown in Figure 6.1b. As can be seen, the majority of events possess two b-tagged jets. In case of $n_b = 1$, one of the b jets is not identified. In the clustering, a small cut of $p_T \geq 10$ GeV is applied to reduce the number of jets being stored in the sample which can lead to low energetic b-jets being removed. Additionally, it is possible that the B hadron is not associated with the correct jet in the clustering due to a larger deviation between its direction and the jet axis. Even though only two b-quark partons are produced in the event, more than two b-tagged jets can occur due to B hadrons decaying into further B hadrons in the Monte Carlo simulation. Hence, these hadrons can tag different jets if their direction is significantly different with respect to their mother particle.

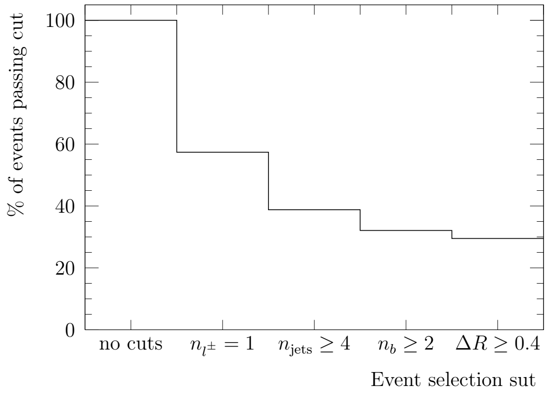

Fig. 6.2: Cutflow for particle level event selection. Sample: $m_t = 172.5$ GeV and $\Gamma_t = 1.3$ GeV.

Figure 6.2 depicts the cutflow when applying the particle level events selection after selecting the objects as described in the previous section. About 40% of the events fail the first selection criteria that requires the events to have exactly one charged signal lepton. This is partly due to τ leptons decaying hadronically thus yielding no charged signal lepton in the final state. The larger fraction of events failing this cut compared to the fractions given in figure 6.1a is due to the object selection rejecting a substantial amount of charged leptons.

The object definition also causes a large amount of events to have less than four jets, resulting in those events failing the second event selection criteria. The last two selection criteria on particle level then reduce the number of selected events to $\sim 30\%$ of the original number. All samples, which are used in the presented studies, have been generated such that at least three million events remain after the event selection.

6.3 Width and Mass variation

As mentioned before, studying the potential benefits and applications of measuring the differential cross-section $\mathrm{d}\sigma/\mathrm{d}m_t$ on particle level is one of the goals of this thesis. Consequently, investigating the effect of different values for m_t and Γ_t on the shape of the distribution in m_t^{part} is crucial. Therefore, this section will present the plots visualising the shape of the distribution while the next section will quantify these differences using ensemble tests.

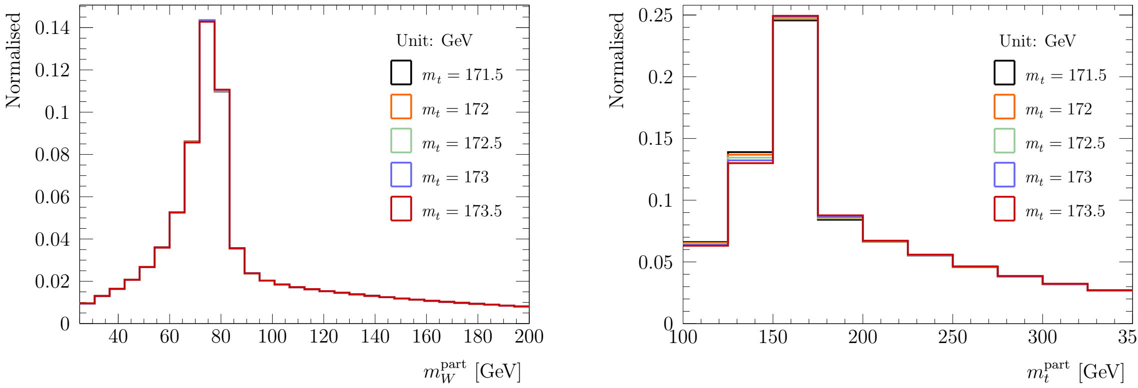

(a) m_W^{part} distribution (b) m_t^{part} distribution

Fig. 6.3: Distributions in the invariant mass of the hadronically decaying pseudo top and W boson on particle level. The distributions are shown for different values of the top-quark's mass m_t which was set in the Monte Carlo generator.

As expected, no difference between the electron and muon channel is observed on particle level and thus both are merged for the particle level studies. In Figure 6.3, the distribution in the invariant mass of the hadronically decaying pseudo top and W boson are shown for different values of the top-quark mass m_t. As expected, the distribution in m_W^{part} shown in Figure 6.3a does not show a dependence on the value of m_t. Figure 6.3b to the right shows the invariant mass of the hadronically decaying pseudo top-quark. The relatively large bin width of 25 GeV has been chosen in light of later performed unfolding studies: it has to be larger than the resolution to avoid large correlations. As one can see, the distribution in m_t^{part} shows a significant dependence on m_t. For a smaller value of m_t, the distribution is shifted to smaller values of m_t^{part} as expected. However, m_t has been varied within the current experimental precision. Being better than 1%, the differences in the shapes are small.

Figure 6.4 shows the same two plots as before for different values of the top-quark decay width. As before, the distribution in m_W^{part} in Figure 6.4a shows no dependence on the value of Γ_t. The large range of different values for the decay width spans two orders of magnitude. A clear dependence can be seen in case of m_t^{part}. The distributions shown in Figure 6.4b are broader for increasing values of Γ_t. Nonetheless, even on particle level without any detector effects, the distribution is much broader than the width of the

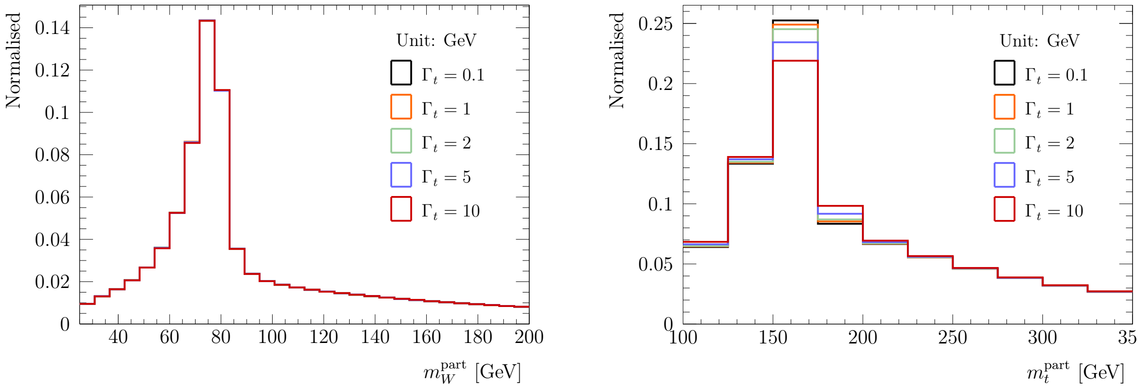

(a) m_W^{part} distribution

(b) m_t^{part} distribution

Fig. 6.4: Distributions in the invariant mass of the hadronically decaying pseudo top and W boson on particle. The distributions are shown for different values of the top-quark's decay width Γ_t which was set in the Monte Carlo generator.

underlying top-quark. This is caused by effects of the jet clustering as the jet energies and direction do not exactly match the ones of the partons they supposedly stem from. Therefore, special care has to be taken concerning all uncertainties affecting jet energies in the measurement as those can easily exceed – and thus hide – the effect of Γ_t. This will be discussed in detail in Section 10.

Both the distribution in m_t^{part} and m_W^{part} display a very long tail which is caused by events in which the wrong jets are chosen to construct the hadronically decaying pseudo top. Those events do not contribute to the sensitivity of the distribution in m_t^{part} on m_t and Γ_t and hence reduce the statistical precision in a measurement of these variables.

6.4 Ensemble Tests

Figures 6.3b and 6.4b show a clear difference in the shape of the distributions depending on the value of the underlying parameters used in the Monte Carlo event generation process. The depicted distributions are based on simulations with a vast abundance of simulated events and thus the statistical fluctuations are negligible. However, in the full 8 TeV data sample with an integrated luminosity of $\int \mathcal{L} = 20.3\,\mathrm{fb}^{-1}$ recorded by the ATLAS experiment, one expects roughly 100000 selected $t\bar{t}$ events with exactly one e or μ in the final state (see Section 7.4).

Focussing on the question of how well the different shapes can be discerned, this section will estimate the expected statistical uncertainty for 100000 selected events. This is equivalent to the best possible precision in case of a detector which measures the particle level constituents perfectly. The determination of the statistical precision will be done using a parametrised template fit with distributions as in Figures 6.3b and 6.4b as templates. To this end, one first derives a parametrisation of the shapes to obtain the distribution for any given value of Γ_t and m_t. In the following, the fitting procedure is explained and an example is shown before the results of the ensemble tests are given.

6.4.1 Template Parametrisation

In order to be able to predict the shape of the m_t^{part} distribution for different values of m_t and Γ_t, a parametrisation is necessary. Two parametrisations are obtained: one as a function of Γ_t at a fixed mass of $m_t = 172.5\,\text{GeV}$ and one being a function of m_t at a fixed decay width of $\Gamma_t = 1.3\,\text{GeV}$. In principal, a two dimensional fit estimating both m_t and Γ_t would be ideal – especially given the Standard Model connection between the mass and width of the top-quark. However, obtaining a two dimensional parametrisation – and generating a large amount of samples for different combinations m_t and Γ_t – would be necessary to achieve this. This was deemed too costly for the studies discussed here and hence only one dimensional fits are performed. Furthermore, the effect of varying m_t and Γ_t are distinct as the first leads to a translation of the distribution while the latter changes the width. Therefore, one-dimensional fits are expected to work very well.

Unfortunately, no parametrisation using an analytic probability density function could be determined which is able to describe the distribution reasonably well. To circumvent this limitation, one parametrises each bin in the histogram separately as a function of the underlying value. To achieve this, the distribution in each generated sample is normalised such that the sum over all bins is equal to one – as is the case in Figures 6.3b and 6.4b. Figure 6.5 shows the bin content of two bins for different values of Γ_t at a fixed mass of $m_t = 172.5\,\text{GeV}$. It is found that the dependence of the i-th bin's content can be described by a second degree polynomial:

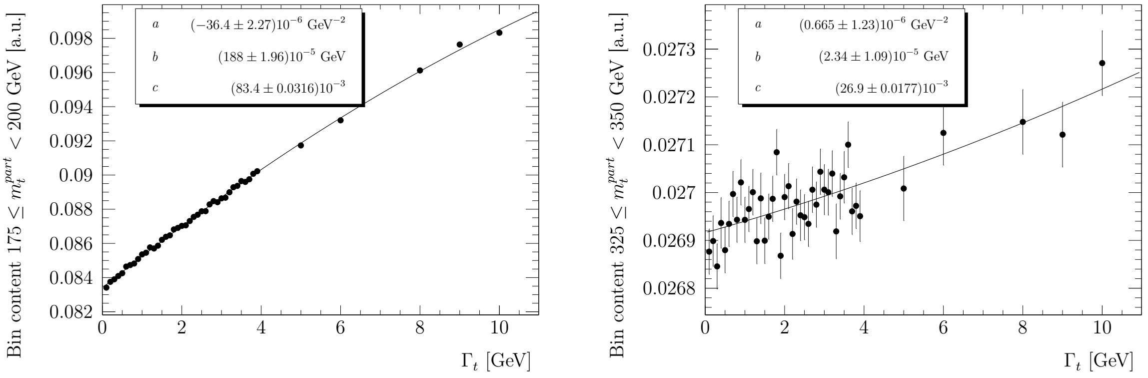

(a) peak (b) tail

Fig. 6.5: The content of a bin in the peak and the tail of the distribution in m_t^{part}. Additionally shown are the corresponding second degree polynomial fits to parametrise the dependence on Γ_t for fixed $m_t = 172.5\,\text{GeV}$. As can be seen, the polynomials describe the dependence well.

$$f_i^x(x) = a \cdot x^2 + b \cdot x + c \ ,$$

with x being either m_t or Γ_t. To obtain the histogram for a given value of x, the value for each bin is taken from the corresponding parametrisation. Afterwards, the entire histogram is scaled up to match the desired total number of events yielding the expected number of events in the i-th bin ν_i^x.

The parametrisation also smoothes the function and removes statistical fluctuations due to finite statistics in the Monte Carlo samples themselves as seen in case of bins in the tail of the distribution, e.g. Figure 6.5b. All parametrisations are given in the appendix in Figures A.1, A.2, A.3 and A.4.

6.4.2 Fitting Procedure

As mentioned before, these studies employ a template fit to test the sensitivity of the chosen observables under variation of m_t and Γ_t (again referred to as x). The parametrisations obtained before serve as the template used in the fit. As a first step, one defines a true and in the following fixed value of x. The true distribution ν_i^x is obtained by scaling the result of the parametrisation to match a total number of histogram entries of $N = 100000$, roughly corresponding to the expected number of signal events selected with the ATLAS detector. ν_i^x is then used to generate pseudo-datasets by drawing a random number y_i for each bin i from a Poisson with mean ν_i^x. To estimate the value $\hat{x}$ whose distribution in m_t^{part} obtained from the parametrisation best match the observed pseudo-dataset, one performs a χ^2 fit to the pseudo-dataset:

$$\chi^2 = (\vec{\nu}^x - \vec{y})^T Y^{-1} (\vec{\nu}^x - \vec{y}) \ .$$

Here, a histogram is again given in vector notation. The matrix Y is the covariance matrix of $\vec{y}$. In this first step, $\vec{y}$ is obtained by fluctuating the bin contents of the true histogram. Therefore, the covariance matrix is simply a diagonal matrix: $Y_{ij} = \delta_{ij} y_i$. Nonetheless, the general matrix notation for the χ^2 is introduced here as the same fitting procedure will be applied later on to evaluate the performance of the unfolding. In that case, Y becomes the non-trivial covariance matrix given by the unfolding procedure as described in Section 4. Figure 6.6 illustrates the shape of the χ^2 function around its minimum. The plot is taken from a randomly chosen pseudo-dataset with a true value of $\Gamma_t = 1.3\,\text{GeV}$ and $m_t = 172.5\,\text{GeV}$. The estimator $\hat{x}$ for the true value is given by the minimum of the χ^2 determined by using the Minuit software package [56]. Around its minimum, the χ^2 is well described by a second degree polynomial. Therefore, the probability density function of the estimator $\hat{x}$ can be assumed to be reasonably well described by a Gaussian distribution. Consequently, the estimated statistical uncertainty $\hat{\sigma}(x)$ – defined as Gaussian 68% uncertainty – is given by the σ which solves

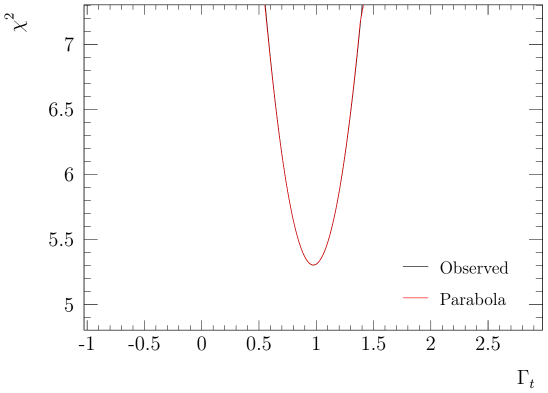

Fig. 6.6: Example χ^2 for Γ_t fit. A perfect agreement between the χ^2 and the polynomial is seen.

$$\Delta\chi^2 = \chi^2(\hat{x} \pm \sigma) - \chi^2(\hat{x}) = 1 \ .$$

In the following, the results of the ensemble tests are presented. In such a test, the here described procedure is repeated for a large number of pseudo-datasets to study the statistical properties of the estimators.

6.4.3 Results

For each chosen true value, 20000 pseudo-datasets are generated and the fit described above is performed. In the following, the performance of the fit and the expected statistical uncertainty when studying variations of the mass and width are described.

Estimation of the Decay Width

The results of the ensemble test estimating $\hat{\Gamma}_t$ is given in Figure 6.7. In the range of $\Gamma_t = 1\,\text{GeV}$ and $\Gamma_t = 3\,\text{GeV}$, true values for the decay width are tested in steps of 0.1 GeV. Figure 6.7a shows the distribution in $\hat{\Gamma}_t$ for $\Gamma_t = 1.3\,\text{GeV}$. As can be seen, the distribution resembles a Gaussian distribution which is in agreement with the observation that the region around the minimum in the χ^2 is well described by a second degree polynomial. The same is true for the distribution in $\hat{\sigma}(x)$ – the estimator for the statistical uncertainty on $\hat{\Gamma}_t$ – shown in Figure 6.7b. It is also noteworthy that the distribution is very narrow, yielding almost the same value for $\hat{\sigma}(x)$ in every pseudo-dataset. Qualitatively, the plots are the same for the other tested true values Γ_t and hence not shown here.

The following Figure 6.7c displays the expectation value of the estimator $\hat{\Gamma}_t$ for different true values Γ_t. A deviation between the expectation value of an estimator and the true value would indicate a biased measurement. Both values agree very well for all tested Γ_t. A linear fit yields values compatible with the ideal case of no offset and a slope of one. Figure 6.7d shows the expectation value of the statistical uncertainty $\hat{\sigma}(\Gamma_t)$. Overall, a statistical precision of roughly 0.3 GeV is expected with a minor increase towards larger values of Γ_t. As this is the expectation value on particle level and assuming a perfect detector, the actual statistical uncertainty is going to be larger once the reconstruction level and unfolding are considered. Furthermore, the statistical uncertainty is typically proportional to $1/\sqrt{N}$ and hence even in case the 100000 events which are used as the available statistics turns out to not have been chosen optimally, the expected uncertainty would only change slightly.

To validate whether the estimated statistical uncertainty correctly describes the spread of $\hat{\Gamma}_t$ seen in Figure 6.7a, the pull distributions are calculated. Figure 6.7e shows the distribution of $(\hat{\Gamma}_t - \Gamma_t)/\hat{\sigma}(\Gamma_t)$ assuming $\Gamma_t = 1.3\,\text{GeV}$. If the estimator is indeed distributed according to a Gaussian distribution, the distribution in the pull has to be compatible with a unit Gaussian if $\hat{\sigma}(\Gamma_t)$ is correctly estimated. As can be seen, the distribution agrees well with a unit Gaussian distribution. The same is true for all other studied values of Γ_t but not shown here. Figure 6.7f shows the mean value and the standard deviation of the pulls for all tested Γ_t. As can be seen, both agree very well with the expected values indicating that the statistical uncertainties are estimated correctly.

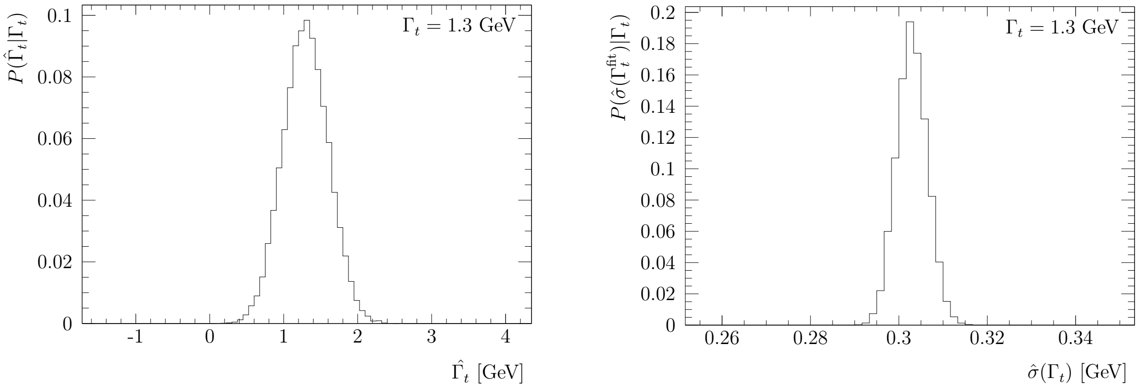

(a) Distribution in $\hat{\Gamma}_t$ for $\Gamma_t = 1.3\,\mathrm{GeV}$ **(b)** Distribution in $\hat{\sigma}(\Gamma_t)$ for $\Gamma_t = 1.3\,\mathrm{GeV}$

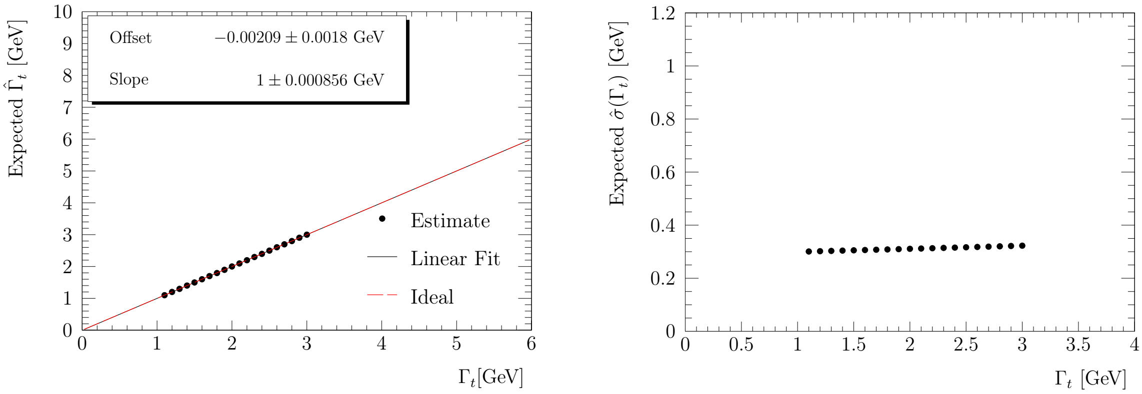

(c) Expected $\hat{\Gamma}_t$ **(d)** Expected $\hat{\sigma}(\Gamma_t)$

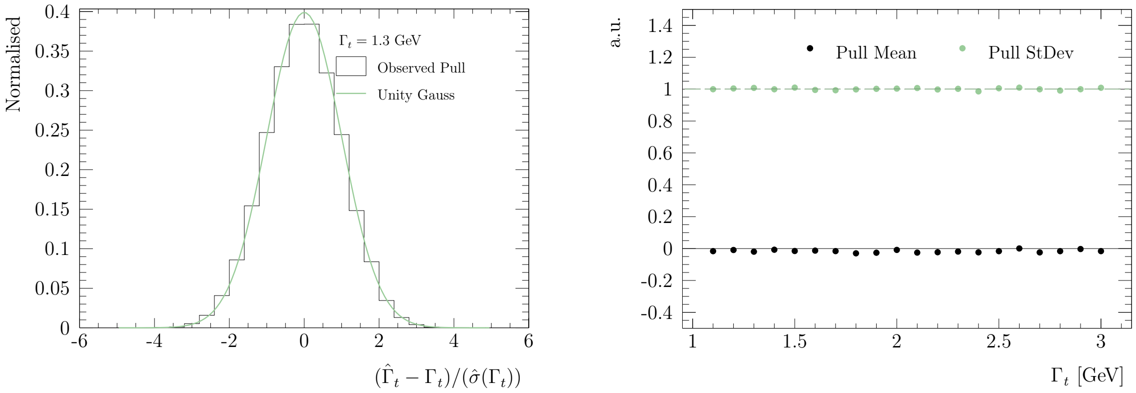

(e) Pull distribution for $\Gamma_t = 1.3\,\mathrm{GeV}$ **(f)** Pull mean and standard deviation

Fig. 6.7: Results of the ensemble test on particle level investigating the sensitivity of the distribution in m_t^{part} to Γ_t. For the pull distribution as well as the distributions in the estimators, the results for a true value of $\Gamma_t = 1.3\,\mathrm{GeV}$ are chosen for illustrative purposes. The corresponding distributions for other values of Γ_t are found to yield identical results. Overall the figures demonstrate a good performance of the fit, for more details see the text.

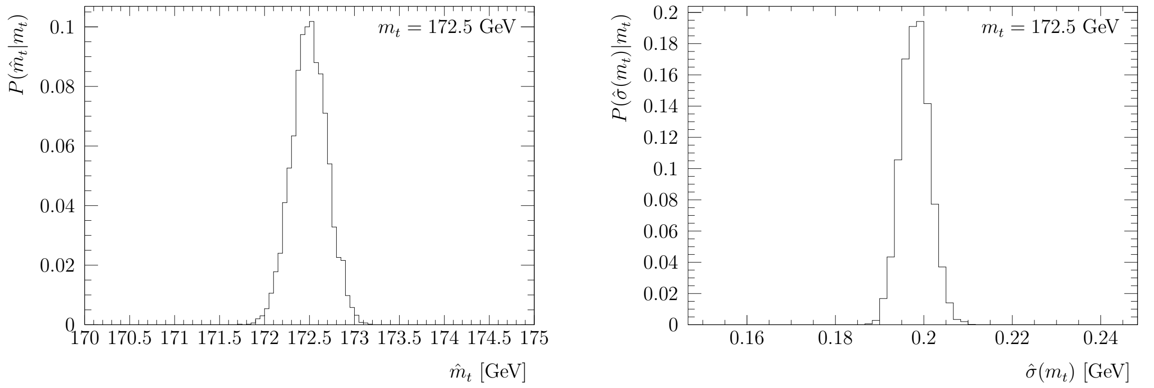

(a) Distribution in $\hat{m}_t$ for $m_t = 172.5$ GeV **(b)** Distribution in $\hat{\sigma}(m_t)$ for $m_t = 172.5$ GeV

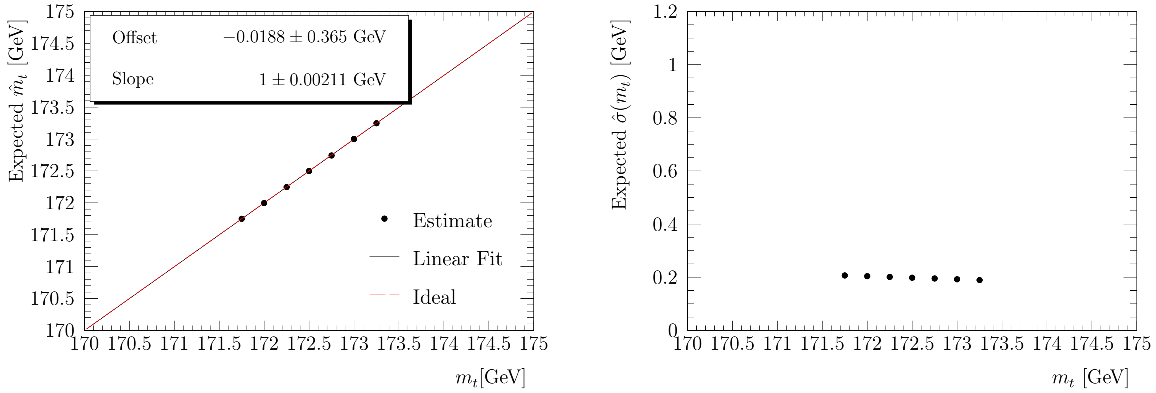

(c) Expected $\hat{m}_t$ **(d)** Expected $\hat{\sigma}(m_t)$

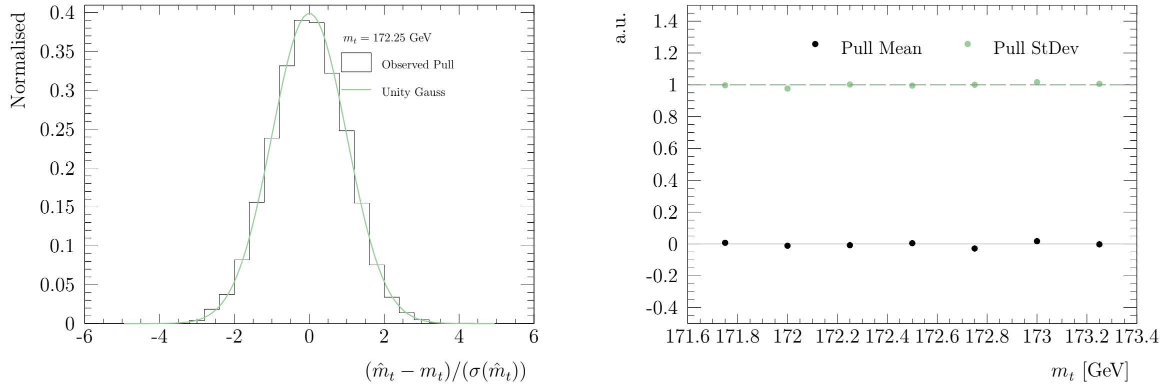

(e) Pull distribution for $m_t = 172.5$ GeV **(f)** Pull mean and standard deviation

Fig. 6.8: Results of the ensemble test on particle level investigating the sensitivity of the distribution in m_t^{part} on m_t. For the pull distribution as well as the distributions in the estimators, the results for a true value of $m_t = 172.5$ GeV are chosen for illustrative purposes. The corresponding distributions for other values of m_t are found to yield identical results. Overall the figures demonstrate a good performance of the fit, for more details see the text.

Estimation of the Mass

A second ensemble test on particle level is performed to study the estimation of the top-quark mass and the expected statistical precision. The corresponding plots depicting the results of the test are shown in Figure 6.8. As the same points presented before in the discussion of the results for Γ_t still apply, they are not repeated here. Overall, the ensemble test again reveals a well-performing fit. The estimator $\hat{m}_t$ is unbiased and the estimated statistical uncertainty $\hat{\sigma}(m_t)$ seems to be correctly determined. The expected statistical uncertainty on particle level is about 0.2 GeV corresponding to a very small relative uncertainty. Concluding, m_t can be determined precisely on particle level.

6.5 Potential for Model Testing

As mentioned in the motivation for a particle level measurement: the quantities can be used to easily test different models on their agreement with the measurement without having to add a simulation of detector effects on top of the model predictions. Therefore, one example for such a model test is presented here and will be picked up in the following chapters discussing the unfolding.

In order to illustrate the potential for model testing, the matrix element final state multiplicity is taken as an example. As discussed in Section 2.3, Monte Carlo event generation is separated into the matrix element and the parton shower stage. For the studies presented so far, $pp \to t\bar{t}(j)$ events are generated. This means that the matrix elements for $t\bar{t}$ and $t\bar{t}j$ final states have been calculated. Any further QCD radiation, and thus jets, are added during the parton shower stage of the event generation. However, it is also possible to just generate $t\bar{t}$ events and let the parton shower do all radiation effects. Consequently, one could also add more partons in the matrix element calculation before passing the event to the parton shower. While the first is potentially several orders of magnitude faster, the latter is potentially more precise. More final state particles allow more complicated processes with additional internal lines which go beyond mere radiation effects. An unfolded data spectrum could be used to easily find the number of additional partons required to achieve a good agreement.

Figure 6.9a shows the distribution in m_t^{part} for three different samples generated with Sherpa as described before but with zero, up to one and up to two additional partons in the matrix element. All three samples have the same values of $m_t = 172.5$ GeV and $\Gamma_t = 1.3$ GeV. A clear deviation between the different curves can be see. To visualise the difference between the different settings, an ensemble test is performed using the distribution for $1j$ as the reference. As before, each pseudo-dataset is a Poisson variation corresponding to a total statistics of $N = 100000$. For every pseudo-dataset, the χ^2 with respect to the distributions in Figure 6.9a is calculated and the resulting distributions in χ^2/d.o.f. are shown in Figure 6.9b.

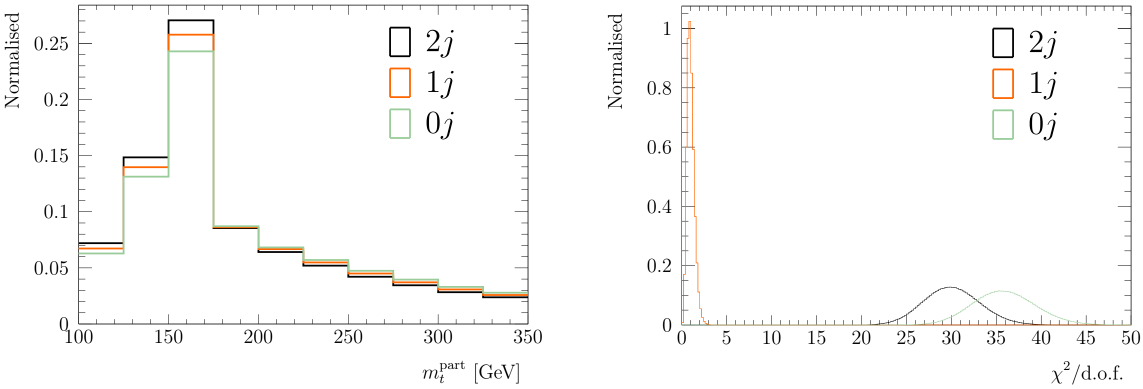

(a) m_t^{part} distribution **(b)** Separability

Fig. 6.9: The effect of different numbers of additional matrix element final state multiplicities ($2j$ means up to two additional partons etc.). Figure 6.9a shows the resulting distributions in m_t^{part} while 6.9b contains a plot illustrating the separability. The shown χ^2/d.o.f. is obtained by sampling $1j$ with a statistics of $N = 100000$.

Obviously, the distribution for $1j$ is centered around one. The distributions for $0j$ and $2j$ are clearly distinct and show no overlap with $1j$ and thus the different multiplicities can be clearly differentiated on particle level within the expected statistics. The following chapters follow up on this effect and test if this statement is still valid once the additional uncertainties due to unfolding and systematic effects are considered.

7 The Reconstruction Level

The actual measurement coming from the detector is done on reconstruction level. Therefore, this section will present the object definitions and event selection criteria applied on this level. Additionally, the Monte Carlo samples used to model the reconstruction level are described and their predictions are compared to the actual data. Lastly, the connection between both levels in this analysis – the response matrix – is presented.

7.1 Object Definition

While a Monte Carlo event record is the input when defining the objects on particle level, reconstruction level definitions rely solely on the output of the detector. The different detector subsystems, as described in Section 3.2, and their different behaviour depending on the incoming particle are the crucial ingredients.

Jets

Jets are reconstructed in the detector from the calorimeter cells which are combined to form topological clusters. These clusters are given as an input to the jet clustering which again employs the anti-k_t clustering algorithm with a jet radius of $R = 0.4$. The obtained jets are then calibrated based on the p_T and η obtained from the clustering. Among different quality criteria being applied in the selection of jets, they are required to have $p_T > 25\,\mathrm{GeV}$ and $|\eta| < 2.5$.
Jets stemming from b-quarks are identified by making use of the long lifetime of B hadrons present in these jets. A displacement between the primary vertex and their decay vertex can be resolved in the detector. This information can be analyzed by several algorithms [57]. In this analysis, a cut is applied to the output of the neural-network based MV1 tagger, which has been calibrated to have an efficiency of 70% for identifying a b-jet [58].

Electrons

Electrons shower and deposit their energy in the electromagnetic calorimeter. To differentiate electrons from photons, these clusters have to be matched to tracks in the inner detector. Detailed information on the reconstruction algorithm and the efficiencies can be found in References [59, 60]. Selected electrons need to be within the detector's central region $|\eta| < 2.47$ with the transition region $1.37 < |\eta| < 1.52$ between barrel and end-cap electromagnetic calorimeter being excluded. Narrow QCD jets can produce a very similar signature in the detector. To reduce the contribution of those fake leptons, a set of quality and isolation criteria is applied as well.

Muons

Muons can be detected in the inner detector as well as the muon system. In the top physics group, an algorithm performing a global track fit utilising both information is used and its performance is studied in Reference [61]. As muons can be produced during the decay of a hadron inside a jet, a set of isolation requirements is applied in addition to the quality requirements on the performed track fit. The obtained muon is required to have $p_T > 25\,\mathrm{GeV}$ and $|\eta| < 2.5$ to be selected.

Missing Transverse Momentum

The missing transverse momentum can be obtained by requiring momentum balance in the transverse plane. Therefore, the momentum in the transverse plane of all selected objects presented before is combined with the rejected objects and all topological clusters not associated with a jet. Several calibrations are then applied to obtain an estimate for the missing transverse energy in the event.

7.2 Event Selection

Similar to the event selection on particle level, several criteria are employed to select $e +$ jets and $\mu +$ jets events and to suppress the contributions from background events. Background events are events whose signature in the detector is equal to that of the desired signal events. These can either be processes which already produce the same parton level signature as the one found in the decay of $t\bar{t}$ pairs or caused by misidentification of objects in the detector. The following criteria are used:

- The event must have been triggered by a trigger system specifically looking for electrons in the $e +$ jets and muons in the $\mu +$ jets channel. For electrons, either the EF_e24vhi_medium1 or EF_e60_medium1 must have fired while EF_mu24i_tight and EF_mu36_tight are used for muons.
- The primary vertex in the event is required to have at least five tracks associated to it.
- Exactly one good, selected electron or muon is found in the event.
- This charged lepton must match the lepton which caused the trigger to fire. The distance in ΔR between the trigger lepton and the selected lepton has to be smaller than 0.15 in order for them to be matched.
- The event must have at least four selected jets in total.
- Two of those jets must be tagged as b-jets.

Besides these requirements, additional criteria are applied which take care of technical problems that might have occurred. Examples for this are requiring the data taking to have taken place under good run conditions and the rejection of events with so called bad jets not stemming from physical objects but detector noise in the calorimeters. The analysis uses TopRootCore [62], a set of packages provided by the top physics working group of the ATLAS collaboration which takes care of the object reconstruction, applying the recommended calibrations and performing the event selection on samples provided as input.

The samples which are used in these studies are described in the following.

7.3 Data and Monte Carlo Samples

The analysis uses the full dataset recorded by the ATLAS detector at a centre-of-mass energy of 8 TeV corresponding to a total integrated luminosity of $\int \mathcal{L} = 20.3\,\text{fb}^{-1}$. After applying the event selection presented in the previous section, the set of selected events is comprised of different contributions from the signal process and several background sources. The different contributions are modelled by Monte Carlo simulations which simulate up to the particle level. These simulations are then processed by a Geant4 simulation of the ATLAS detector [63, 64].

The $t\bar{t}$ signal sample is simulated by the PowHeg generator [65–67] using the CT10 parton density functions [68]. PowHeg is interfaced to Pythia [69] which is used for the simulation of the underlying event and the hadronisation. The underlying event refers to the remnants of two colliding protons and is simulated using the CTEQ6L1 parton density function [70].

Vector bosons produced in association with extra jets from radiation can mimic the signature of the studied $t\bar{t}$ decays. In case of a leptonically decaying W boson, $W+$jets events have the same signature if enough jets pass the b-tag requirement. Even though leptonically decaying Z bosons would yield two charged leptons, one of those might not be reconstructed and only seen as missing transverse momentum. Hence, $Z+$jets production is also considered as a background. Both processes are generated using Alpgen [71] with the CTEQ6L1 parton density function and passed to Pythia with the same settings as before.

The diboson events WW, ZZ and WZ can also yield the same signature if one of the bosons decays leptonically, the other hadronically. The processes are modeled by Alpgen and hadronisation is done by Herwig [72] with the CTEQ6L1 parton density function.

Lastly, the contributions due to single top-quarks are generated using AcerMC [73] for the t-channel production. In case of s-channel or Wt production, the process is simulated by PowHeg. In both cases, the events are passed again to Pythia.

All of the aforementioned samples are normalised to $\int \mathcal{L} \cdot \sigma$ where σ are the respective theoretical predictions for their cross-section. Lastly, pure QCD processes solely consisting of jets in the final state can also pass the event selection. This requires one of those jets to be reconstructed as a charged lepton and hence this background is often referred to as fake lepton or QCD multijet. Even though isolation criteria are employed in the object selection it cannot be avoided that some of those events pass the selection. To estimate the contribution of this background, a data driven method is used. The matrix method [74, 75] compares the yields of the nominal event selection with one using a loosened lepton isolation criterion. From this, event weights are derived and the shape as well as the normalisation of the background is determined from the data sample using those weights.

7.4 Monte Carlo and Data Comparison

The aforementioned Monte Carlo and data samples are passed through the reconstruction and event selection. The number of selected events in each sample for the different channels are shown in Table 7.1. Due to requiring two b-tagged jets, a high signal purity of more than 80% is achieved. However, the Monte Carlo simulations in total predict less selected events than are actually observed in data. The kinematic distributions for the pseudo top-quark are given in Figure 7.1 and 7.2. As can be seen, the underestimation is present in almost all bins of the distribution with the exception of the high $p_{T,t}^{reco}$ region. This indicates a mis-modelling in the Monte Carlo simulations. The agreement between predictions and data will improve once modelling uncertainties are considered. Nonetheless, the predictions follow the shape of the data reasonably well and hence are sufficient for the proof-of-concept studies performed in this analysis.
About 125000 $t\bar{t}$ events are predicted to be selected in the 8 TeV dataset recorded by the ATLAS detector. This is close to the number previously assumed in the studies presented in the previous chapter. To ensure consistency, the following studies are thus also performed using $N = 100000$.

7.5 Response Matrix

The response matrix – the main ingredient needed in any unfolding method – is derived from the $t\bar{t}$ signal sample. The particle level is constructed in each event and the event selection is performed. In order to construct the response matrix from a two-dimensional histogram, pairs of the invariant masses of the hadronically decaying pseudo top on particle and reconstruction level are required. Therefore, the event has to pass both selections.

	e+jets	μ+jets
$t\bar{t}$	49709.3	75911
Single top-quarks	3422.26	4457.68
W+jets	1448.25	2683.05
Z+jets	404.067	430.192
Diboson	47.5089	63.3363
Fake lepton	2236.24	1798.83
Total	57267.6	85344.1
Data	59191	90836

Tab. 7.1: Event yields for the data and simulated samples.

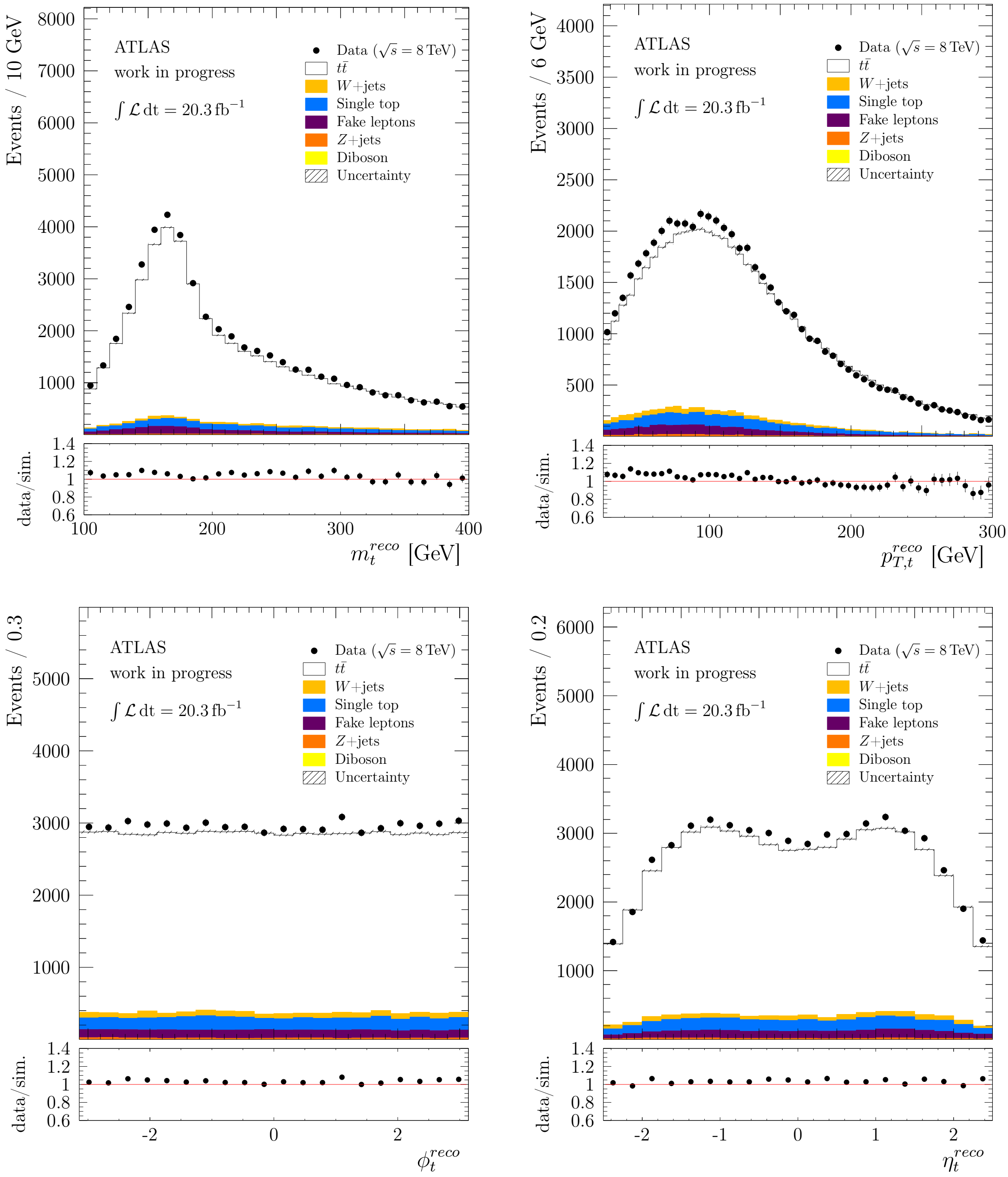

Fig. 7.1: Monte Carlo and data comparison for events passing the e+jets selection. The uncertainty on the Monte Carlo predictions is caused by limited statistics available in the Monte Carlo samples. In the ratio plot, it is combined with the statistical uncertainty due to the number of measured events.

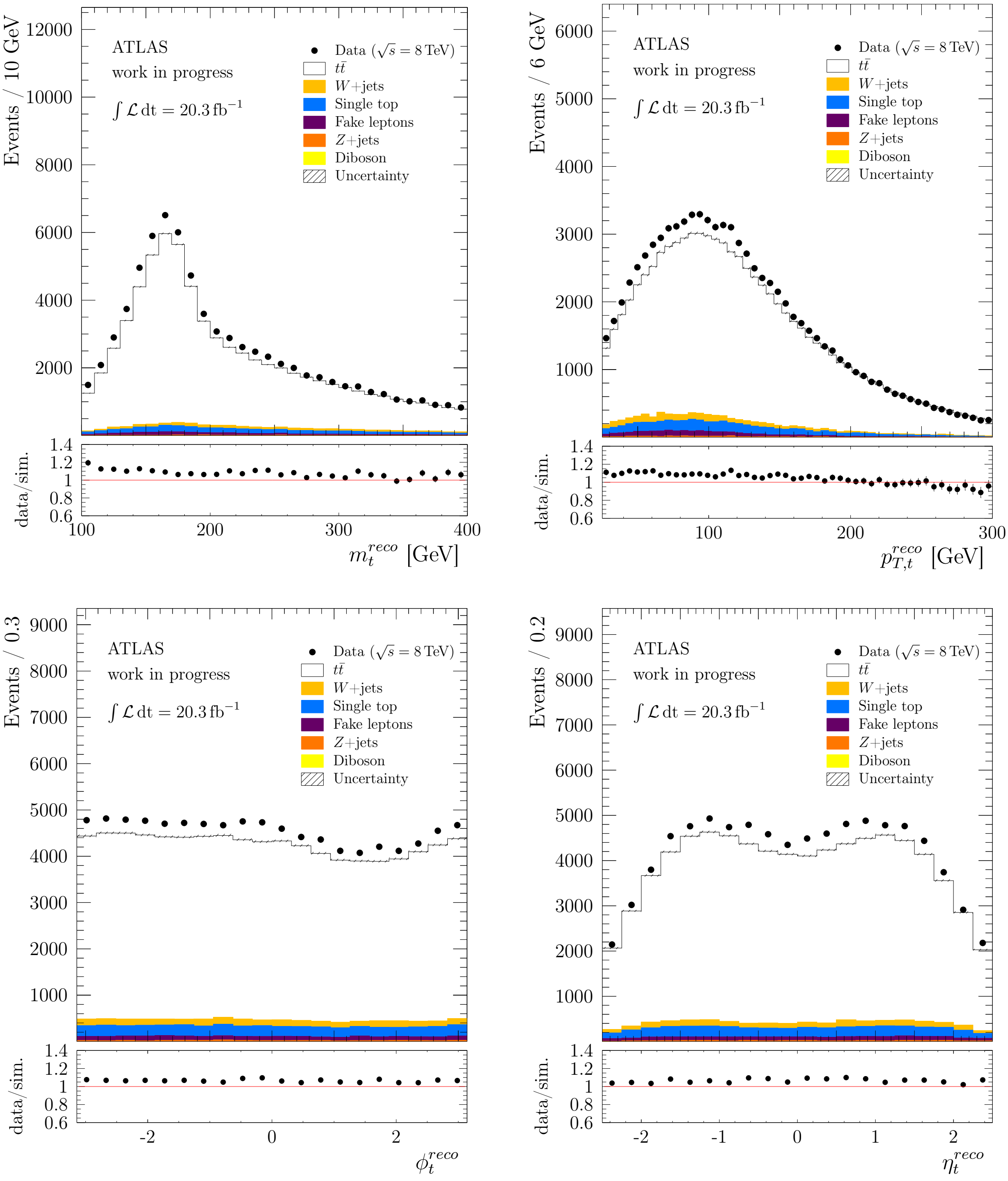

Fig. 7.2: Monte Carlo and data comparison for events passing the μ+jets selection. The uncertainty on the Monte Carlo predictions is caused by limited statistics available in the Monte Carlo samples. In the ratio plot, it is combined with the statistical uncertainty due to the number of measured events.

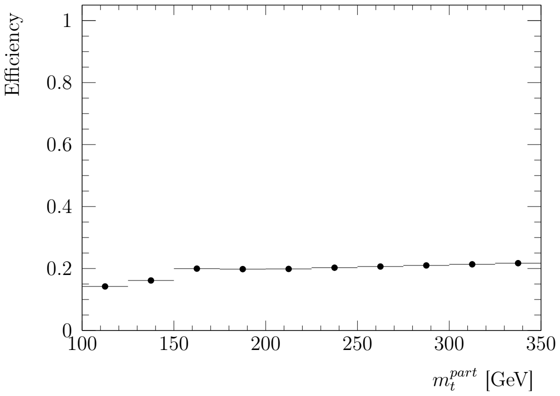

Fig. 7.3: Efficiency to select an event on reconstruction level if it is selected on particle level.

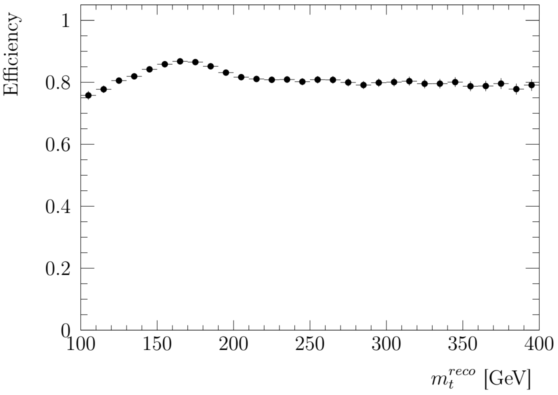

Fig. 7.4: Efficiency to select an event on particle level if it is selected on reconstruction level.

The efficiency to reconstruct an event on reconstruction level if it has already passed the particle level selection is shown in Figure 7.3. It can be interpreted as the efficiency of the detector and can be corrected during the unfolding process by applying the inverse of the efficiency as a correction factor on the unfolded distribution. Except for the first two bins, the efficiency is almost constant over the entire range of m_t^{part} values. The smaller values in the first two bins are caused by the looser event selection on particle level causing more events with small m_t^{part} to pass the selection. However, the looser event selection on particle level is necessary to counteract one problem: the set of events selected on reconstruction level is not a subset of the events selected on particle level. This is seen in Figure 7.4 which shows the efficiency for an event to pass the particle level selection if it has passed the reconstruction level one. The efficiency is much larger than in the opposite case but significantly smaller than 100%. This efficiency can not intuitively be interpreted as a property of the detector as it indicates that the detector measured an event that was actually not there. The treatment of such an efficiency is still under discussion. One possibility is the application of the efficiency as per bin correction on the measured distribution before applying the unfolding procedure.

The response matrix obtained from the e+jets events passing both event selections is shown in Figure 7.5. As can be seen, the maximum in each row of the matrix is consistent with the value of m_t^{part} for that row. Nonetheless, the distributions are very broad and one bin in m_t^{part} gives substantial contributions to a large range of m_t^{reco} values. This is caused by the large resolution on the mass of the pseudo top in addition to combinatorial effects. As no matching between the objects on particle and reconstruction level is performed, the response matrix also includes events where the reconstruction level pseudo top is not built from using the measured version of the jets used to build the particle level pseudo top. Therefore, few events with a large deviation of m_t^{part} and m_t^{reco} are found.

The large bin width of 25 GeV is necessary to reduce large bin-to-bin migrations. The response matrix shows this as the maximum in m_t^{reco} in one bin of m_t^{part} does not overlap with the maximum in neighbouring bins of m_t^{part}. For smaller bin width in m_t^{part}, this is not the case anymore which has a negative impact on the performance of the unfolding. Studies

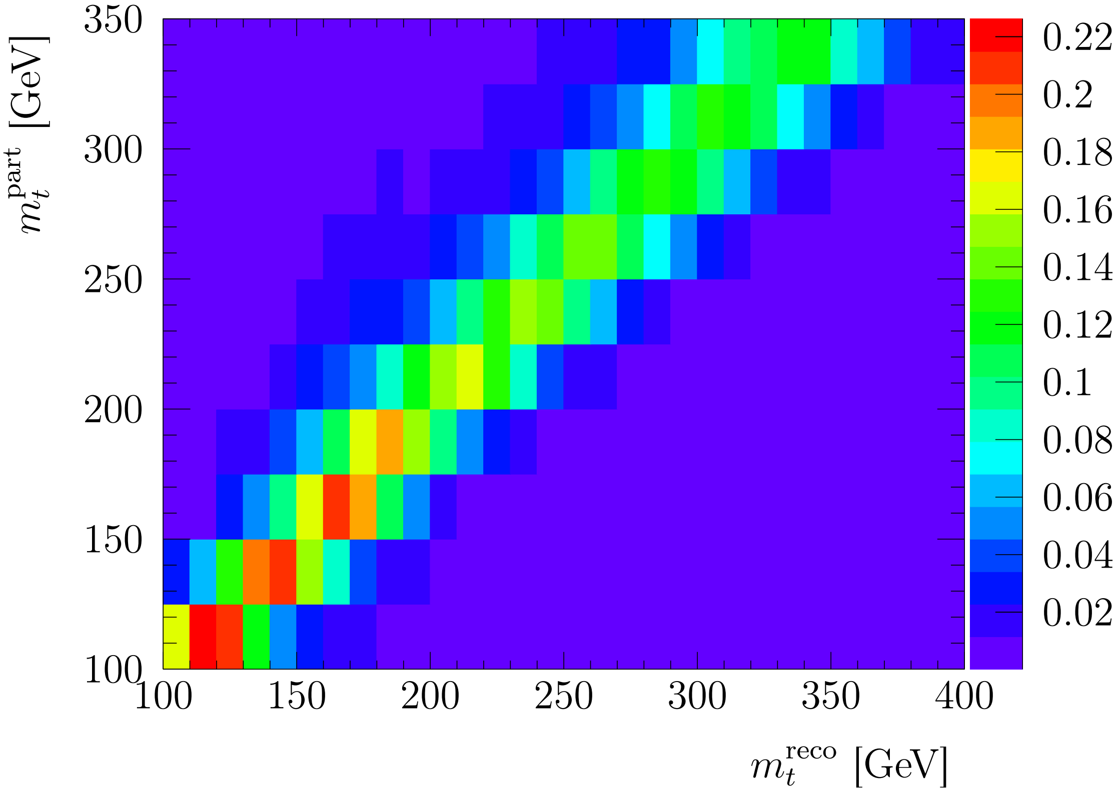

Fig. 7.5: Response matrix for e+jets obtained from the $t\bar{t}$ signal sample. It is normalised as a conditional probability function $p\left(m_{t,i}^{reco}|m_{t,j}^{part}\right)$ and hence each row in the histogram sums up to one.

using smaller bin sizes show a negative impact on the performance as large correlations arise in the unfolded spectrum.

The response matrix is used in the following chapters to both generate reconstruction level distributions as well as in the unfolding studies presented. As all following studies are to be understood as being proof-of-concept studies, one neglects the differences between electrons and muons. The aforementioned response matrix obtained from $e+$jets events is used to model the detector in the following studies while the statistics still correspond to the one expected for $e+$jets and $\mu+$jets.

8 Reconstruction Level Studies

This chapter presents reconstruction level studies similar to the ones performed on particle level in Chapter 6. It describes the sensitivity to m_t and Γ_t using reconstruction level distributions, unfolding to particle level will be discussed in the next chapter. The template fit used to investigate potential biases and the expected statistical uncertainty when testing different values for m_t and Γ_t is identical and thus not described here. For all following studies, the measurement process is defined to be described by the response matrix seen in Figure 7.5. Reconstruction level templates are thus obtained by multiplying the particle level distributions taken from the samples generated with Sherpa in Chapter 6 with the response matrix (see Equation (4.4)). The distributions in m_t^{reco} for any value of m_t and Γ_t are also obtained by using the parametrisations for m_t^{part} and smearing those with the response matrix.
For simplicity, effects due to reconstruction and selection efficiencies are not included in these studies. Both efficiencies are correction factors applied per bin and hence will have an influence on the shape of the unfolded distribution. However, the templates would also be corrected and scaled. Therefore, no change in the studied sensitivities would be seen.

8.1 Width and Mass Variation

The distribution in m_t^{reco} is shown in Figure 8.1 for different values of m_t and Γ_t respectively. As can be seen, the shape of the distribution still depends on the values assumed in the Monte Carlo generator. The distributions are still shifted towards smaller m_t^{reco} values for decreasing m_t and become broader for increasing Γ_t.

However, the overall distribution is much broader than the particle level distribution due to resolution effects. Hence, one expects a significant reduction in the expected statistical precision, especially when estimating the decay width of the top-quark. An ensemble test is again employed to investigate the sensitivity on both properties of the top-quark.

8.2 Results of the Ensemble Test

The pseudo-datasets used in this test are generated by randomly fluctuating the reconstruction level distributions corresponding to an expected number of events of $N = 100000$ as before. The results of the Γ_t ensemble test are shown in Figure 8.2. As can be seen in

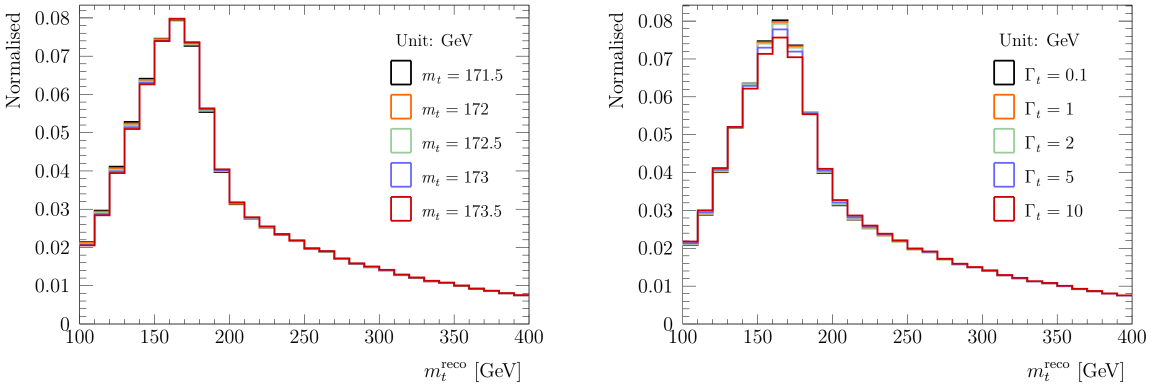

(a) m_t variation **(b)** Γ_t variation

Fig. 8.1: Distributions in the invariant mass of the hadronically decaying pseudo top m_t^{reco} on reconstruction level. 8.1a shows the normalised distributions for different values m_t while 8.1b for different values of Γ_t

Figures 8.2a and 8.2c, the result of the fit is unbiased as before. The standard deviation estimated from the pull distribution again agrees with the expectation and hence indicates a correct estimation of the statistical uncertainty in each template fit. However, the expected statistical uncertainty seen in Figure 8.2b is about 0.95 GeV which is about three to four times larger than the uncertainty found on particle level. This is consistent with the observation that the reconstruction level distribution is much broader because of the detector resolution.

The results of the sensitivity test for m_t are presented in Figure 8.3. They also show a well performing template fit with no biases. The expected statistical uncertainty is roughly 0.3 GeV and thus only slightly larger than on particle level. This is due to the sensitivity on the mass being based on the translation of the distribution which is less affected by resolution effects and hence retains much of the precision seen on particle level.

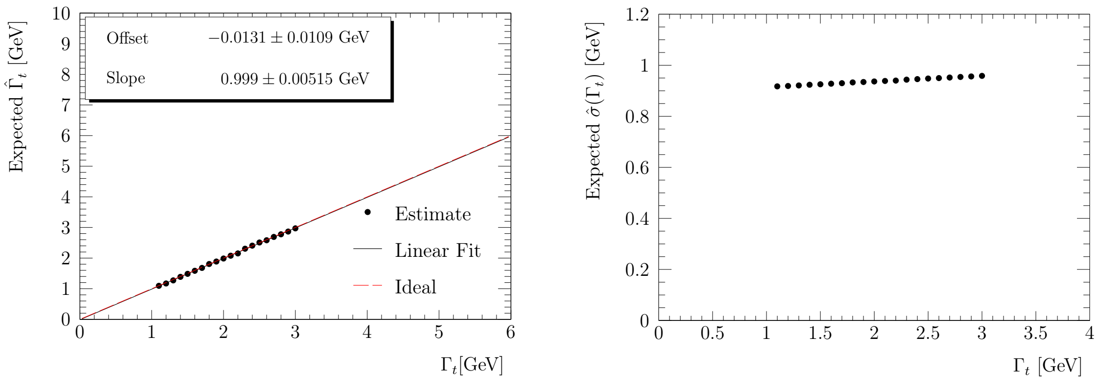

(a) Expected $\hat{\Gamma}_t$

(b) Expected $\hat{\sigma}(\Gamma_t)$

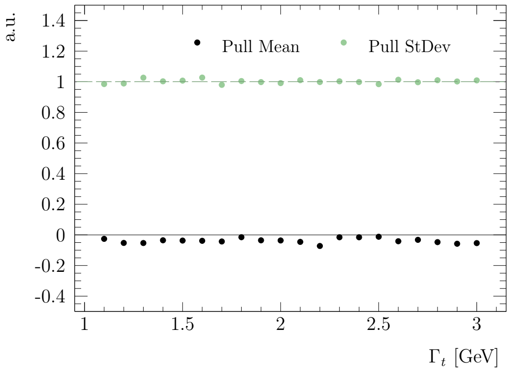

(c) Pull mean and standard deviation

Fig. 8.2: Results of the ensemble test on reconstruction level investigating the sensitivity of the distribution in m_t^{reco} to Γ_t. Overall the figures demonstrate a good performance of the fit, for more details see the text.

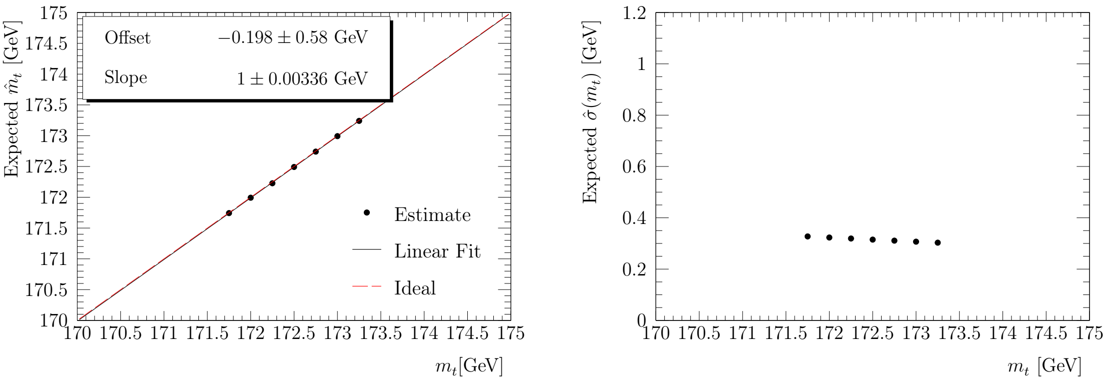

(a) Expected $\hat{m}_t$

(b) Expected $\hat{\sigma}(m_t)$

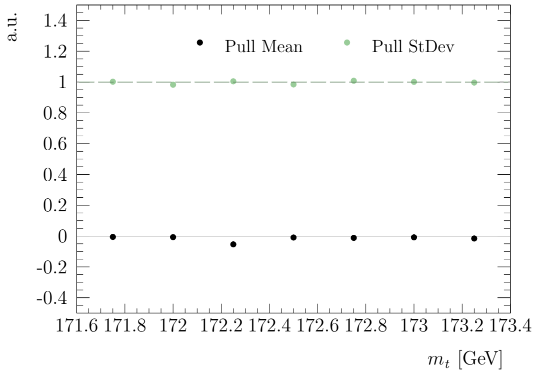

(c) Pull mean and standard deviation

Fig. 8.3: Results of the ensemble test on reconstruction level investigating the sensitivity of the distribution in m_t^{reco} to m_t. Overall the figures demonstrate a good performance of the fit, for more details see the text.

9 Correction to Particle Level

In this chapter, unfolding is applied to reconstruction level distributions to study the performance of the unfolding and the effect on the estimation of the top-quark mass and decay width. First, the effect of different values for the regularisation parameter on the unfolded distribution is discussed and an optimal value is determined. Afterwards, ensemble tests are employed to determine the sensitivity on m_t and Γ_t and to investigate potential biases due to the regularisation. Concluding this, the example to illustrate the potential of model testing is picked up again.

Illustrating figures showing unfolded distributions and the obtained correlation matrices are all based on the same, randomly chosen pseudo-dataset from the reconstruction level ensemble test for $m_t = 172.5\,\text{GeV}$ and $\Gamma_t = 1.3\,\text{GeV}$.

9.1 Choice of Regularisation Parameter τ

Section 4.2 discusses the necessity for a regularisation scheme to reduce statistical fluctuations in the unfolded distribution. To illustrate this effect, Figure 9.1 shows the results of the unfolding of the randomly chosen pseudo-dataset without any regularisation applied. The unfolding was performed using the SVD method and setting $\tau = 0$. As can be seen in Figure 9.1a, the unfolded distribution fluctuates around the true distribution and the statistical uncertainty per bin is significantly larger than the ones for the reconstructed distribution also shown. These large uncertainties are partially compensated by the high

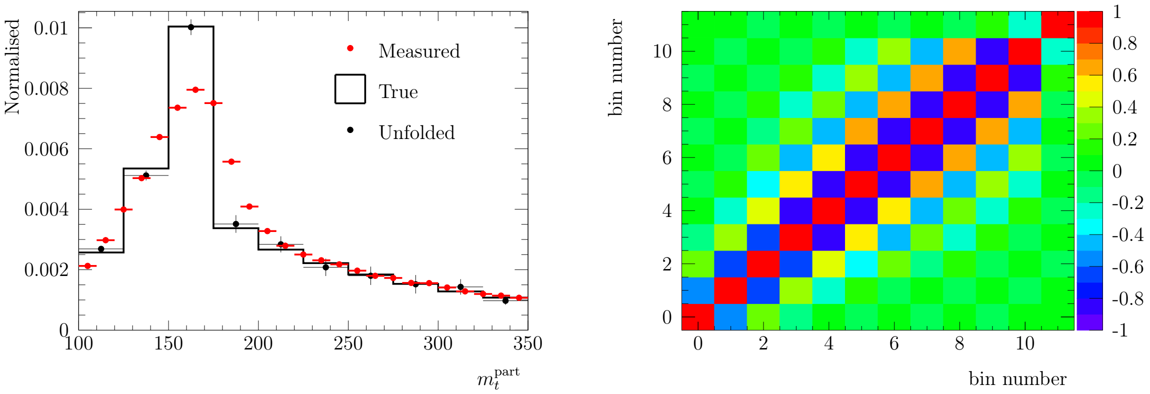

(a) Unfolded distribution (b) Correlation matrix

Fig. 9.1: Result of unfolding for one pseudo-dataset without regularisation being applied ($\tau = 0$).

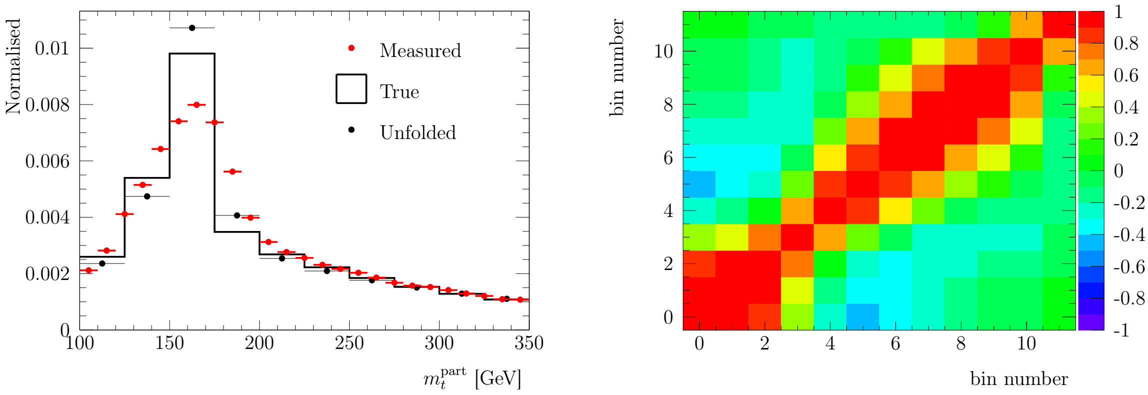

(a) Unfolded distribution (b) Correlation matrix

Fig. 9.2: Result of unfolding for one pseudo-dataset using large regularisation parameter $\tau = S_{kk}^2$ with $k = 4$.

correlation between the bins as shown in Figure 9.1b revealing fully negatively correlated neighbouring bins. Note here: the migration of events between the different bins in the distribution is not limited to the visible range of the histogram. Consequently, the so called under- and overflow bins collecting all events outside of the actual range of the histogram are considered as two additional bins in the unfolding. Therefore, the shown correlation matrix contains two additional entries for the first and last bin.

In conclusion, to obtain an unfolded distribution free of such fluctuations, the regularisation parameter τ has to be tuned. However, large values for the regularisation do not necessarily yield a better result. To illustrate this effect, Figure 9.2 shows the result of the unfolding using a large value for the regularisation parameter $\tau = S_{kk}^2$ corresponding to $k = 4$. This means that the regularisation will suppress all but the first four terms in the singular value decomposition. As seen in Figure 9.2a, the regularisation removed significant parts of the distribution. Hence, the obtained result from the unfolding is all but useless considering that true and unfolded distribution do not agree at all. Furthermore, large correlations between neighbouring bins are observed which will further complicate the usage of the result due to difficulties in inverting such a correlation matrix.

A possible strategy to determine the optimal value for τ has been presented in Section 4.3. It is based on the obtained coefficients d_i after decomposing the measured histogram in a set of orthogonal contributions. Significant contributions should have coefficients substantially different from zero, in terms of its standard deviation which is – by construction – equal to one. Coefficients for contributions due to statistical fluctuations should be compatible with zero and follow a unit Gaussian distribution. As the orthogonal contributions to the measured histogram are solely defined by the response matrix A and the matrix for the Tikhonov regularisation C, the basis of the decomposition does not change if the measured histogram is changed. Only the coefficients with respect to this new basis do. Therefore, the mean of the absolute value for $|d_i|$ can be estimated by averaging the $|d_i|$ over the

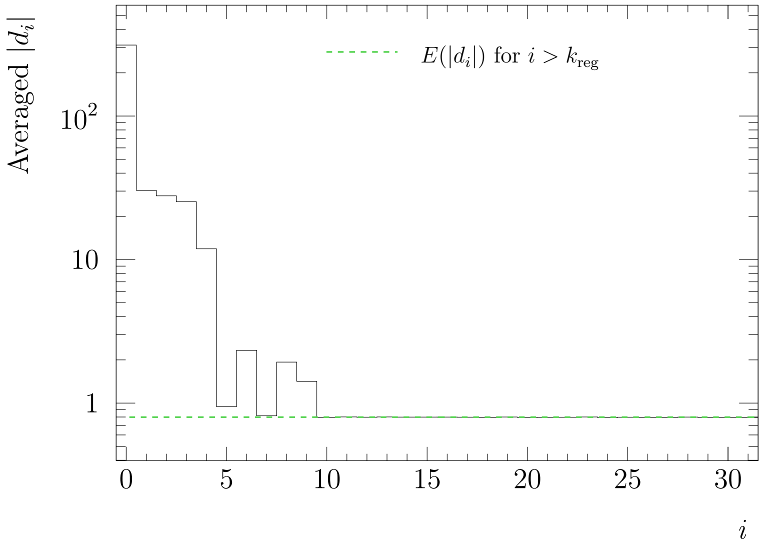

Fig. 9.3: Average coefficient $|d_i|$ of the orthogonal contributions to the measured histograms. Obtained from reconstruction level pseudo-datasets for $m_t = 172.5\,\text{GeV}$ and $\Gamma_t = 1.3\,\text{GeV}$.

pseudo-datasets used in the previous section.

Figure 9.3 shows the obtained average $|d_i|$ values for the pseudo-datasets with $m_t = 172.5\,\text{GeV}$ and $\Gamma_t = 1.3\,\text{GeV}$. For all other studied combinations, the obtained plot is practically identical. It can be seen that the first $|d_i|$ have values significantly larger than zero and thus give a significant contribution. For example $i = 4$, which was chosen in the example in Figure 9.2, clearly is not the last contribution that should be taken into account. Removing those yields the observed discrepancy between true and unfolded spectrum.

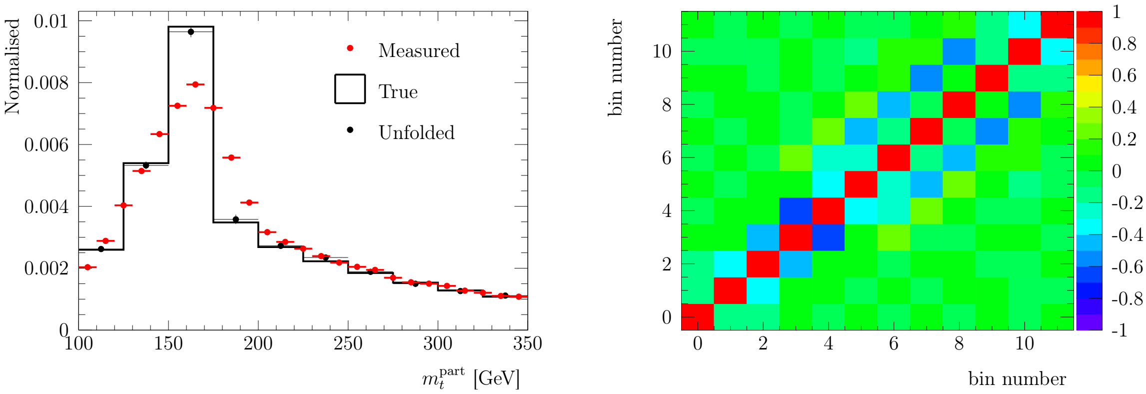

(a) Unfolded distribution

(b) Correlation matrix

Fig. 9.4: Result of unfolding for one pseudo-dataset using large regularisation parameter $\tau = S_{kk}^2$ with $k = 10$.

For $i \geq 10$, the average $|d_i|$ agree very well with the expected value if d_i is indeed distributed according to a unit Gaussian for non-significant contributions. Therefore, the optimal value for the regularisation parameter is given by $\tau = S_{kk}^2$ with $k = 10$. Figure 9.4 shows again the results of the unfolding for the same pseudo-dataset as before.

The unfolded distribution is very close to the true one. Furthermore, the bins in the unfolded distribution are much less correlated than in the previous cases. Only the bins corresponding to the rising and falling flanks are negatively correlated with the central bin. This is to be expected as the largest migration of events will occur at the flanks of the peak.

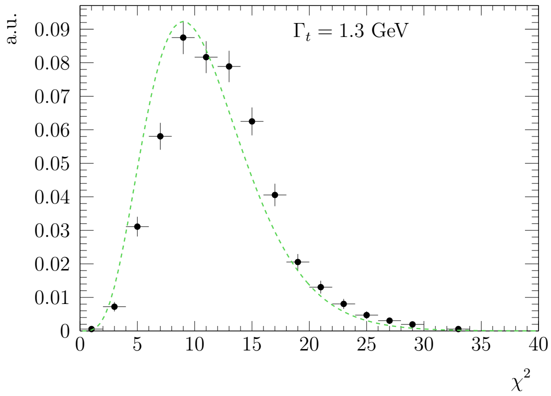

Fig. 9.5: Distribution in the χ^2 between unfolded and true distribution.

Figure 9.5 shows the distribution in the χ^2 computed by comparing the unfolded and true distribution on particle level after unfolding the reconstruction level pseudo-datasets. The estimated covariance matrix of the unfolded distribution is used in the χ^2 calculation. In green, the analytical χ^2 distribution for eleven degrees of freedom is shown ($k = 10$ means the problem is effectively reduced to eleven equations). The expected distribution is slightly shifted towards smaller values compared to the observed distribution. Nonetheless, testing all other possible choices for k and comparing the resulting distribution in χ^2 with the analytical form for $k + 1$ degrees of freedom reveals the best agreement for $k = 10$. Furthermore, the regularisation does not introduce a hard cutoff for all $i > k$ but instead applies a dampening (compare to Equation (4.10)). Therefore, some contributions for $i > k$ might be present depending on the actual distribution of singular values. Hence, the directly obtained number of degrees of freedom $k + 1$ is probably slightly underestimating the actual number which would yield a better agreement between analytical and observed distribution in χ^2.

Overall, the unfolding seems to be able to reconstruct the true distribution reasonably well. In the following, the effect of the unfolding on the estimation of Γ_t and m_t is evaluated as potential biases might be introduced.

9.2 Estimating the Decay Width

When introducing the concept of regularisation in Section 4.2, one remark was given: any kind of regularisation is an external constraint imposed on the problem. Even though the previous section shows huge differences in the performance of the unfolding depending on the chosen value for τ, the choice of a specific τ remains – in the end – arbitrary.

The estimator is rarely unaffected by arbitrarily adding such constraints and thus the regularisation is very likely to introduce a bias. The effect of this bias on the estimation of the top-quark decay width will be described in this section. All considerations are also valid for the estimation of the top-quark mass but will not be discussed in such a detail in this context.

To estimate the decay width, the unfolded reconstruction level pseudo-datasets with known true Γ_t are fitted using the particle level templates as described in Section 6.4.2. The covariance matrix obtained from the unfolding method is used in the χ^2 being minimised. Due to the significantly longer time required to process one pseudo-dataset due to the computation intensive unfolding, only 1800 pseudo-datasets are used per studied true value of Γ_t.

The unfolding method employed in this thesis uses the Tikhonov regularisation. As mentioned before, this demands the unfolded result to be smooth. As smoothness is typically not the first property that comes to mind when talking about distributions with a peak, the distribution should be smooth after dividing it by $\vec{t}^{ini}$. Where $\vec{t}^{ini}$ is chosen to be equal to the distribution in the $t\bar{t}$ signal sample used to obtain the response matrix. Therefore, the regularisation term itself depends on the value of Γ_t as seen in Figure 9.6. For this plot, $\vec{\omega}$ is obtained by using the parametrised particle level templates: $\omega_i = \nu_i^{\Gamma_t}/t_i^{ini}$.

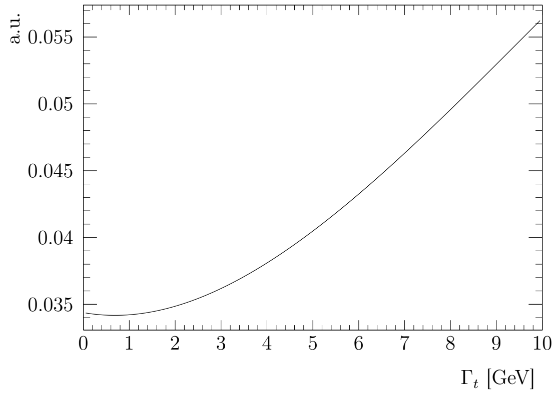

Fig. 9.6: Tikhonov regularisation term $(C\vec{\omega})^T(C\vec{\omega})$ as a function of Γ_t.

Consequently, one expects the regularisation term to prefer distributions more compatible with a small value of Γ_t. Additionally, the bias should become higher for increasing τ as the importance of the regularisation also increases. The regularisation introduces a smooth cutoff which should suppress contributions due to statistical fluctuation as discussed before. Nonetheless, depending on the structure of the decomposed matrix, the cutoff can also affect significant contributions if the corresponding singular value is too close to the value chosen for the regularisation parameter. This will also lead to a bias in the unfolding which increases with increasing τ.

Figure 9.7 compares the expectation value of the template fit result with the corresponding true value for the fitted pseudo-datasets. The ensemble tests are performed for different settings for the regularisation parameter ranging from no regularisation in Figure 9.7*a* to a very large regularisation in 9.7f. As expected, the estimator is unbiased in case of no regularisation due to no external constraints being imposed. This changes towards larger regularisations which lead to a steady increase in the bias. At the working point of the unfolding at $k = 10$, a small bias can be seen. Within the studied range from 1 to 3 GeV, the largest bias amounts to a shift of 9% with respect to the true value. A further increase in the regularisation leads to an even higher bias in case $k = 9$ and an almost useless fit result in case of $k = 8$. This again demonstrates the necessity to carefully tune and select the optimal value for the regularisation parameter. As k can only take integer values, $k = 9$ is the value immediately next to the optimal value but already yields a substantially decreased performance in the template fit.

Figure 9.8 shows the results of the ensemble test for $k = 10$. As can be seen in Figure 9.8a,

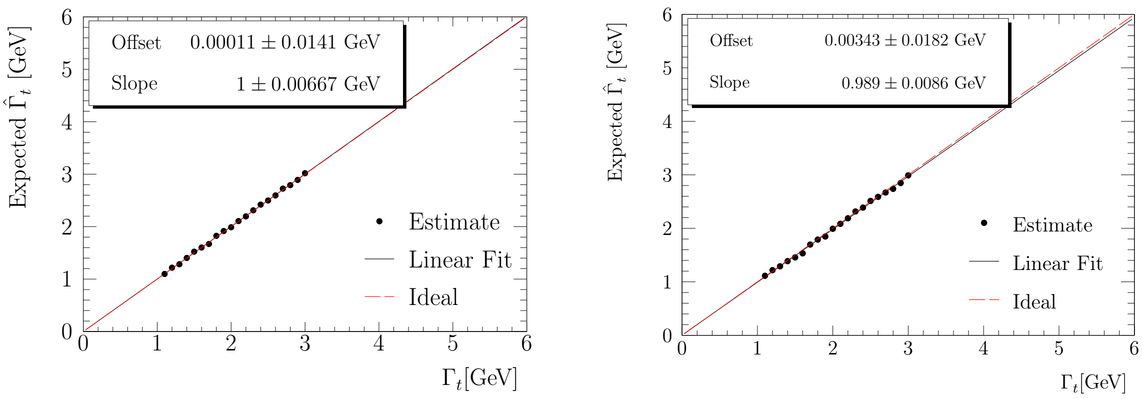

(a) No regularisation **(b)** $k = 15$

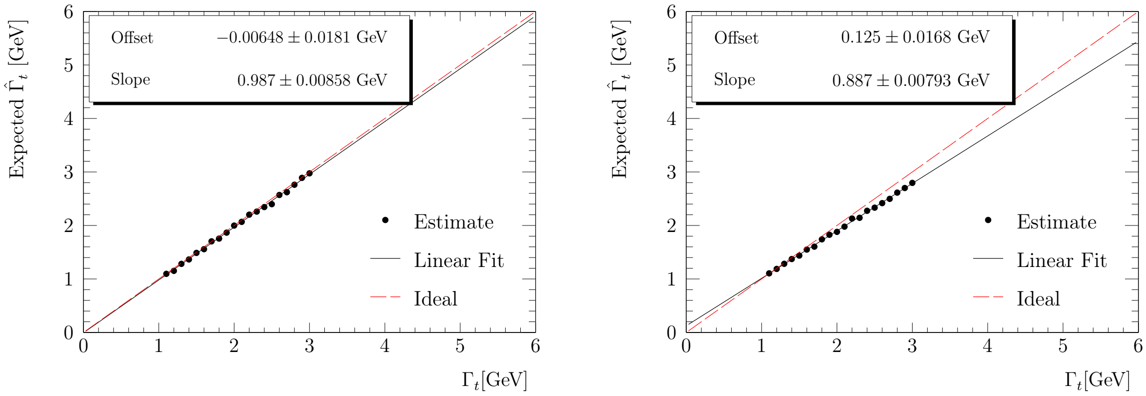

(c) $k = 12$ **(d)** $k = 10$

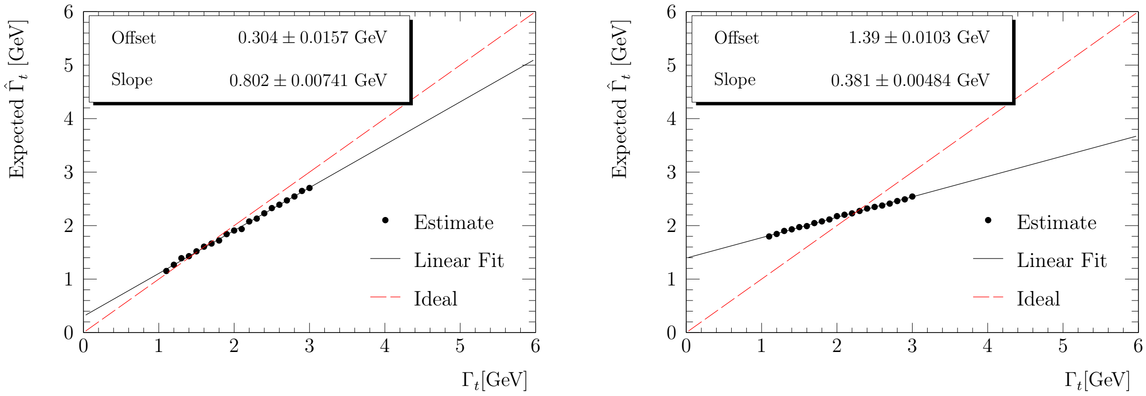

(e) $k = 9$ **(f)** $k = 8$

Fig. 9.7: Expectation value $\hat{\Gamma}_t$ of the template fit compared with the true value Γ_t for different regularisation parameters $\tau = S^2_{kk}$. The expectation value is obtained from a set of pseudo experiments which are unfolded and then fitted to obtain $\hat{\Gamma}_t$. An increasing bias for decreasing values of k (corresponding to a stronger regularisation) can be seen.

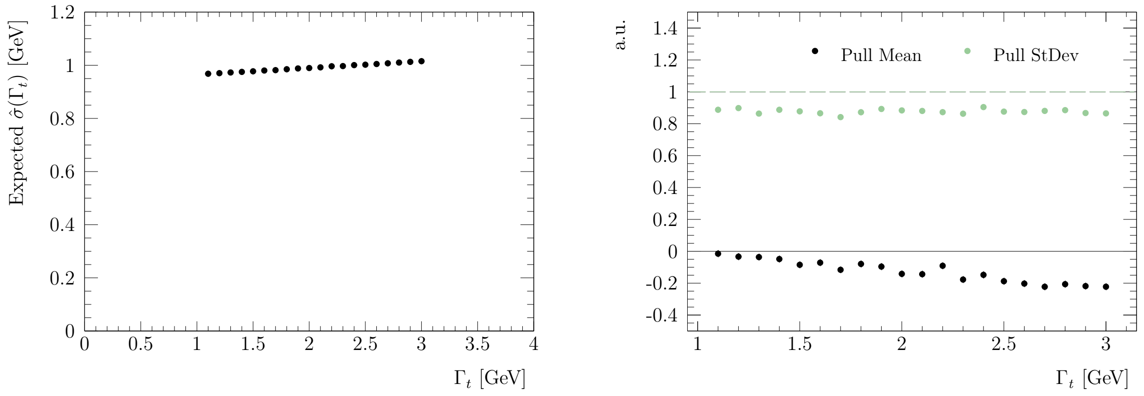

(a) Unfolded distribution (b) Correlation matrix

Fig. 9.8: Result of the ensemble test incorporating unfolding using the optimal regularisation parameter $\tau = S_{kk}^2$ with $k = 10$.

the expected statistical uncertainty is roughly 1 GeV. It is actually slightly larger than, but still comparable to, the expected statistical uncertainty on reconstruction level. This is expected as the unfolding cannot add sensitivity to the reconstruction level distribution which is not there to begin with. Figure 9.8b shows the mean and standard deviation of the pull distributions. The mean values are consistent with the previously seen bias when studying the expectation value of the fit.

However, the standard deviation is significantly smaller than one, indicating overestimated uncertainties in the fit. This effect is also a result of the applied regularisation and increases for larger values of τ. Compensating for the overestimated uncertainties reduces the expected statistical uncertainty and brings it even closer to the one seen in the reconstruction level studies. Consequently, no statistical sensitivity on the decay width is lost by unfolding to particle level instead of performing the measurement on reconstruction level. Due to the large uncertainty, the effect of the bias at $k = 10$ is probably negligible in an actual measurement. The following section will briefly present the results of the ensemble test studying the sensitivity to m_t.

9.3 Estimating the Mass

As mentioned before, the discussion about the effect of different values of the regularisation parameter τ also applies in the estimation of the top-quark mass. Figure 9.9 shows the results of the ensemble test. As is the case for the decay width, a small bias is seen at the regularisation working point $k = 10$. The expected statistical uncertainty is about 0.35 GeV and again slightly larger than the one obtained on reconstruction level. However, studying the pulls again reveals an overestimation of the uncertainty. Therefore, using unfolded distributions in the analysis does not lead to any loss or gain in terms of the precision when measuring the mass of the top-quark.

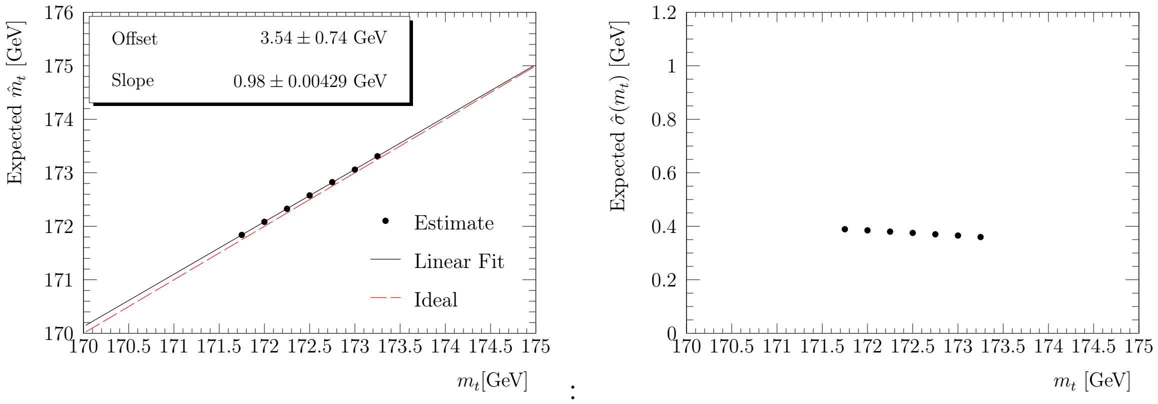

(a) Expected $\hat{m}_t$

(b) Expected $\hat{\sigma}(m_t)$

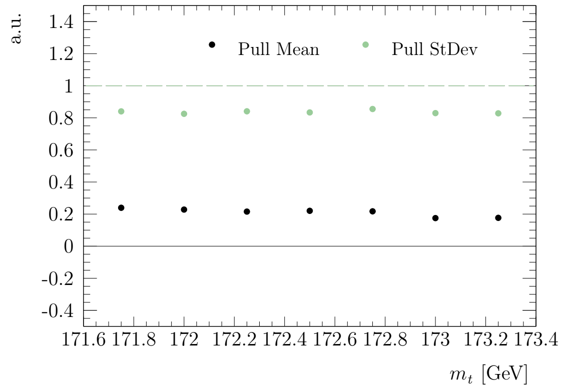

(c) Pull mean and standard deviation

Fig. 9.9: Results of the ensemble test investigating the sensitivity to m_t after applying unfolding. Qualitatively, the results show a small bias introduced by the regularisation. The expected uncertainty agrees with the reconstruction level test.

9.4 Potential for Model Testing

In this section, the example for model testing, which was discussed in Section 6.5, is continued. One of the main motivations to perform a fiducial measurement with unfolding to particle level is the possibility to easily test models without having to run a simulation of the detector. As seen in the previous sections, including unfolding in the analyses does not eliminate the increased uncertainties due to detector effects. Therefore, the study on the separability of the different models with different matrix element multiplicities has to be repeated including the unfolding step.

To evaluate the separability, one again performs ensemble tests in which the reconstruction level distribution in m_t^{reco} for $1j$ is sampled with statistics of $N = 100000$ and then unfolded. The unfolded distribution is then compared to the particle level distributions for the different multiplicities by calculating the χ^2 as before.

The result of the comparison with the particle level $1j$ distribution is already shown in Figure 9.5. The results in the reduced χ^2 are shown in Figure 9.10. The obtained distributions for $0j$ and $2j$ do not have any overlap with the distribution for $1j$. Even though the distributions are still very well separated, the total difference is smaller than the one seen in Figure 6.9b for the particle level ensemble test. Nonetheless, at least in the absence of systematic uncertainties, the unfolded distribution could be used to decide which matrix element multiplicity is sufficient to describe the data.

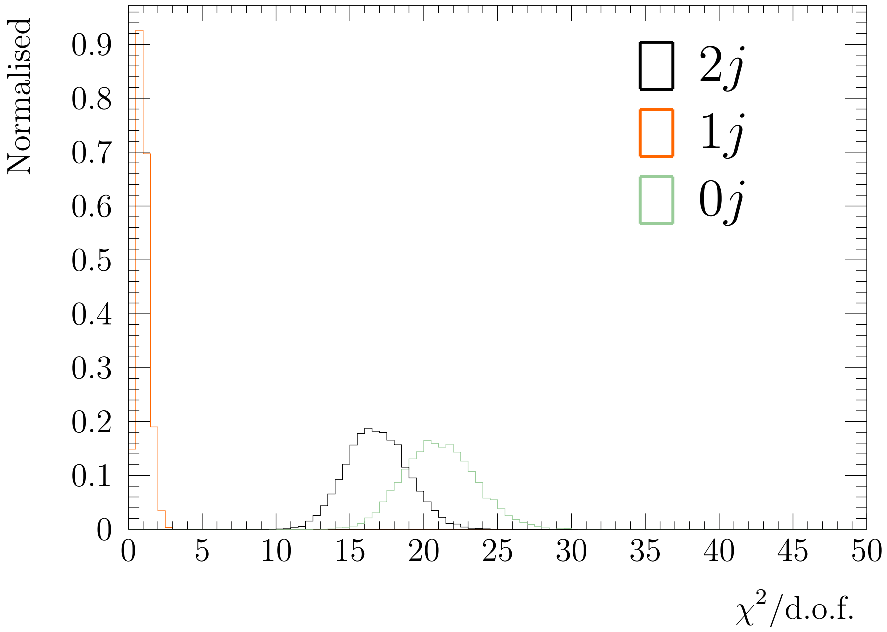

Fig. 9.10: Reduced χ^2 to illustrate the separability of samples with different matrix element multiplicity after unfolding the reconstruction level distribution. 9000 pseudo-datasets are generated for $1j$, unfolded and compared to the true distributions on particle level by calculating the χ^2. Each dataset was generated with statistics corresponding to $N = 100000$ events.

In the next and last chapter, light is shed on the influence of one systematic uncertainty – the jet energy resolution – which will have a large impact on the estimation of the decay width.

10 Jet Energy Resolution

This chapter discusses the uncertainty due to the jet energy resolution modelling in Monte Carlo using a detector simulation. As will be demonstrated, this uncertainty has a huge impact on the performance of a top-quark decay width measurement. In a detector simulation, the energies and momenta of the “measured” jets are additionally smeared to model the resolution effects on these quantities present in the real detector. This is already included in the response matrix used in the previous studies and responsible for the reconstruction level distribution in m_t^{reco} being much broader than the corresponding particle level one in m_t^{part}.

However, the amount of smearing that has to be applied in the simulation is itself just an estimated quantity with an uncertainty [76]. This uncertainty has to be taken into account and propagated to an uncertainty on the measured decay width. The effect of the uncertainty is modeled by applying an additional smearing factor, which is drawn from a Gaussian distribution, to the energy E and transverse momentum p_T of each jet. Additional smearing of the jet energies and momenta will broaden the distribution in m_t^{reco} and thus having exactly the same effect as a larger value for the decay width. This chapter will present the extend of this effect and propose techniques to minimise the effect in an actual measurement.

In the following, JER refers to the current size of the additional smearing that has to be applied as recommended by the ATLAS collaboration and implemented in TopRootCore. Additional factors indicate a modified size of this additional smearing, e.g. $0.5 \cdot JER$ refers to the σ of the Gaussian from which the additional smearing factor is drawn being only half as large as for JER.

10.1 Propagation of the Uncertainty

The effect of the uncertainty on the estimated top-quark decay width is studied by processing the $t\bar{t}$ signal sample with additional smearing applied to the jets. These new samples are then used to construct the response matrix for different strengths of the additional smearing. Two approaches can be followed to estimate the effect of this uncertainty: the newly obtained response matrices can be used in the construction of the reconstruction level distributions which are then unfolded using the nominal matrix as before. Alternatively, the reconstruction level distributions are generated as before

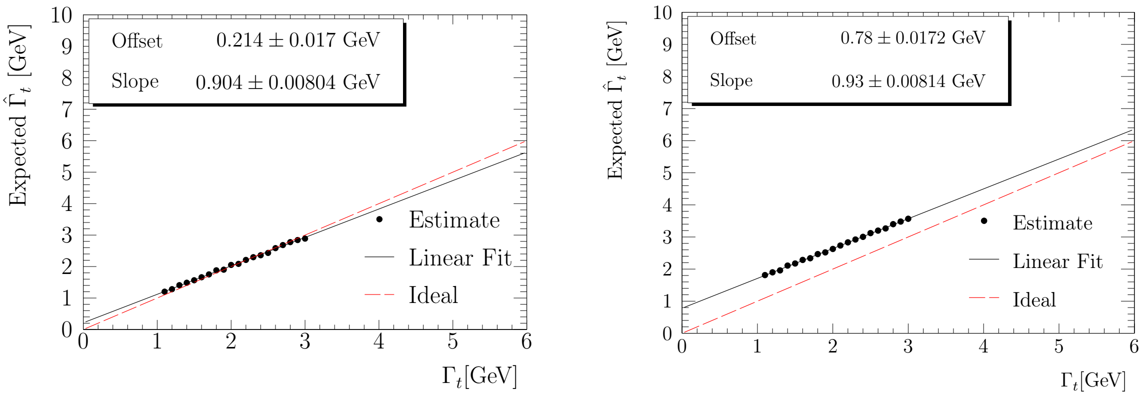

(a) $0.2 \cdot JER$ **(b)** $0.4 \cdot JER$

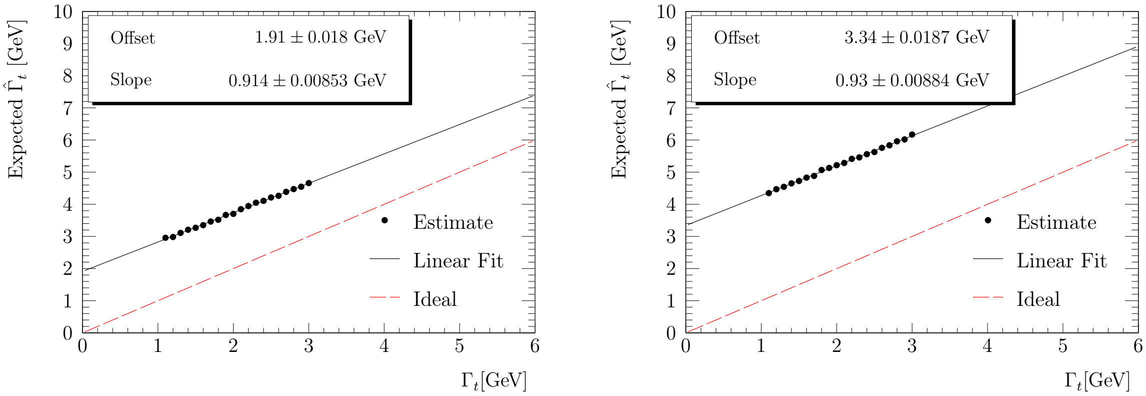

(c) $0.6 \cdot JER$ **(d)** $0.8 \cdot JER$

Fig. 10.1: Expectation value $\hat{\Gamma}_t$ of the template fit to m_t^{part} compared with the true value Γ_t for different strengths of the jet energy resolution uncertainty.

while the new matrices are used in the unfolding step. For these studies, one chooses the first approach as this leaves the actual analysis untouched as only the input – given by reconstruction level distributions – is modified.

The unfolded distributions are then again fitted using the particle level templates. The influence of the systematic uncertainties is investigated using the same ensemble test as before with a fixed regularisation parameter with $k = 10$. The expectation value for $\hat{\Gamma}_t$ is shown in Figure 10.1 for four different strengths of the jet energy resolution uncertainty. While the additional bias in case of $0.2 \cdot JER$ is negligible, it becomes very large even for values still below the recommended value. It is remarkable how the additional uncertainty leads to a bias which just shifts all expectation values up by approximately the same amount. This confirms that the additional uncertainty has the same effect as a larger value for the decay width. The effect will render any measurement useless, especially when the recommend value, which is not even shown here, is used for the jet energy resolution uncertainty.

Therefore, an approach on how to deal with this uncertainty in the measurement and hopefully constrain it to an acceptable level is discussed in the following.

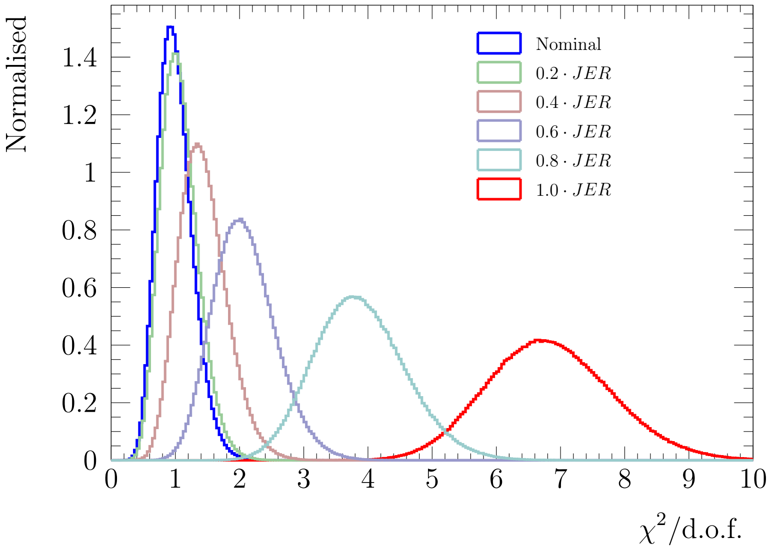

Fig. 10.2: χ^2 test to study the separability of different JER smearing factors using the hadronically decaying W boson mass on reconstruction level. For an interpretation of the shown distribution see the text.

10.2 Constraining the JER Uncertainty

The aforementioned uncertainty on the jet energy resolution is applied in the modelling to ensure an agreement between the simulated samples and the actual data measured by the detector. However, the recommended values should be suitable for a variety of applications and not underestimate the uncertainty. Unfortunately, the resolution has to be modelled as precisely as possible in a decay width measurement. Therefore, a so called *in-situ* calibration of the jet energy resolution should be performed in the measurement. In such a calibration, one performs not only a fit in Γ_t but also in ΔJER which calibrates the resolution and is typically scaled to the known uncertainty $\Delta JER \cdot JER$. The uncertainty on $\hat{\Gamma}_t$ is then obtained by projecting the uncertainty of ΔJER obtained in the fit on Γ_t. Obviously, this fit cannot be performed using the distribution of the mass of the top-quark as the shape of the distribution depends in a similar way on Γ_t and ΔJER. An alternative choice is the distribution of the invariant mass of the W boson based on the pseudo-top definition. As seen before, the latter does not depend on Γ_t and can thus be used in a simultaneous fit determining Γ_t and ΔJER. To estimate the potential for constraining JER, the differences between the reconstruction level W distribution in the $t\bar{t}$ signal sample for different JER smearings and the nominal sample is studied. This is done similarly to the model testing: the nominal distribution is sampled for a statistics of $N = 100000$ and compared with the true distributions by calculating the χ^2. Figure 10.2 shows the distribution in the reduced χ^2 after sampling the nominal distribution many times. The plot shows a good agreement between the χ^2/d.o.f. for the nominal and the $\Delta JER = 0.2$ sample. Therefore, the additional smearing is within the statistical uncertainty which explains the negligible impact on $\hat{\Gamma}_t$ seen in Figure 10.1a. The performed test to constrain ΔJER can be interpreted by assuming the data to be distributed according the nominal distribution without any additional smearing. The fit is unlikely to yield $\Delta JER > 0.8$ as both $0.8 \cdot JER$ and $1.0 \cdot JER$ yield distributions in χ^2/d.o.f. clearly separated of the nominal distribution. However, for smaller values of ΔJER, different ΔJER are hardly distinguishable. As an example, assuming the fit yields a value of $\Delta JER = 0.4$, the uncertainty on this value will be large due to the high overlap to $\Delta JER = 0.2$ and $\Delta JER = 0.6$ seen in Figure 10.2. Projecting this uncertainty onto Γ_t will still yield a substantial uncertainty (see their huge difference in effect shown in Figure 10.1). Fortunately, the uncertainty on the fitted ΔJER and hence on $\hat{\Gamma}_t$ will decrease with additional data as the separation between the curves will improve.

Once multidimensional probability density functions are obtained, the fit with an in-situ calibration of JER can be implemented on reconstruction level. In case of a particle level analysis, one would face several problems: to perform the fit simultaneously for Γ_t and ΔJER, the entire fit should be applied on particle level. This requires the unfolding of the two-dimensional distribution in m_t^{reco} and m_W^{reco}. Unfortunately, the method which is used in this analysis and is found to yield satisfactory results can only unfold one-dimensional problems. One alternative method is Bayesian iterative unfolding [77] which was also tested in this analysis but discarded due to larger biases towards $\vec{t}^{ini}$. Additionally, the $t\bar{t}$ signal sample needs to have a significantly larger statistics as the four-dimensional response matrix will have the squared number of bins compared to the two-dimensional case (which already has 384 bins).

Unfortunately, no Monte Carlo sample with sufficient statistics exists and generating a new one goes far beyond the scope of this thesis. However, the next section will present studies performed using an alternative observable which is less sensitive to the JER uncertainty.

10.3 Alternative Observable $\Delta m = m_t - m_W$

The W boson is constructed by two of the jets that are contained in the pseudo top definition. Therefore, effects which alter those jets resulting in a change of m_W^{reco} should also be affecting m_t^{reco} in a similar way and hence a stabilised observable can be defined by combining both. Several possibilities have been tried and the difference $\Delta m = m_t - m_W$ came out ahead in terms of sensitivity to Γ_t. The obtained distributions in Δm^{part} on particle level are shown in Figure 10.3a. Analog to the studies using m_t^{part} and m_t^{reco}, the sensitivity on particle level is taken from an ensemble test using parametrised templates to fit for Γ_t. The expected statistical precision is shown in Figure 10.3b to the right and is about the same as the one seen for m_t^{part}. The same studies as before have also been performed to verify that no bias is present in the fit (Figures A.5a and A.5b). The response matrix is obtained again from the $t\bar{t}$ signal sample (Figure A.5c), reconstruction level distributions are obtained by multiplying the particle level distributions with this matrix (Figure A.5d). The optimal value for the regularisation parameter $k = 8$ is determined (Figure A.5e) and the expected statistical uncertainty after unfolding is found to be actually slightly better than the one found before (Figure A.5f).

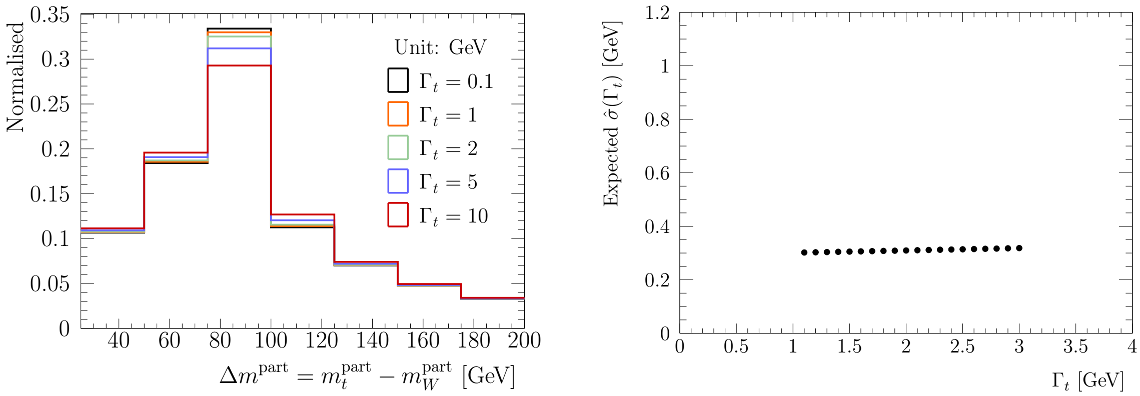

(a) Distributions

(b) Sensitivity

Fig. 10.3: Distribution and expected statistical uncertainty on Γ_t for $\Delta m^{part} = m_t^{part} - m_W^{part}$. Corresponding figures for m_t^{part} are 6.4b and 6.7d.Overall, about the same performance is seen for the new observable on particle level.

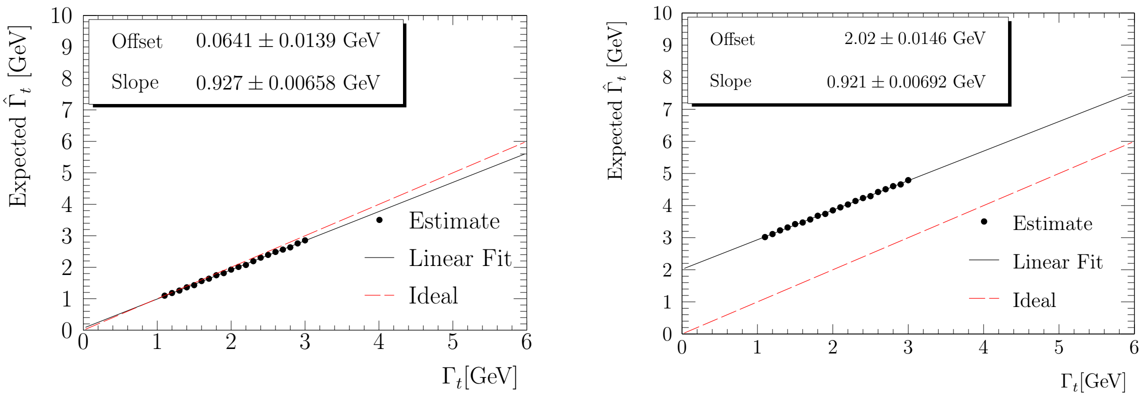

(a) Nominal

(b) $0.8 \cdot JER$

Fig. 10.4: Expectation value $\hat{\Gamma}_t$ of the template fit to unfolded distributions of m_t^{reco} compared with the true value Γ_t for different strengths of the jet energy resolution uncertainty.

Figure 10.4 shows the expectation value for $\hat{\Gamma}_t$ for the nominal and $0.8 \cdot JER$ smearing. In the nominal case, the fit is almost unbiased except for a small slope due to the regularisation as before. The results for $0.8 \cdot JER$ are still shifted towards larger values, however, the effect is substantially smaller than the one seen before in Figure 10.1d. Therefore, alternate observables can lead to a reduction in the uncertainty and should be considered in the actual measurement. It is also possible to combine both an observable less sensitive to resolution modelling uncertainties and an in-situ calibration in the measurement.

10.4 Potential for Model Testing

Concluding the discussion of the uncertainty due to the modeling of the jet energy resolution, the example for model testing is again picked up. In order to apply the χ^2 test as before to determine the separability between the different distributions, the systematic uncertainty has to be added to the unfolded histogram. The additional uncertainty per bin and the correlation are determined from the nominal and JER $t\bar{t}$ signal sample. This

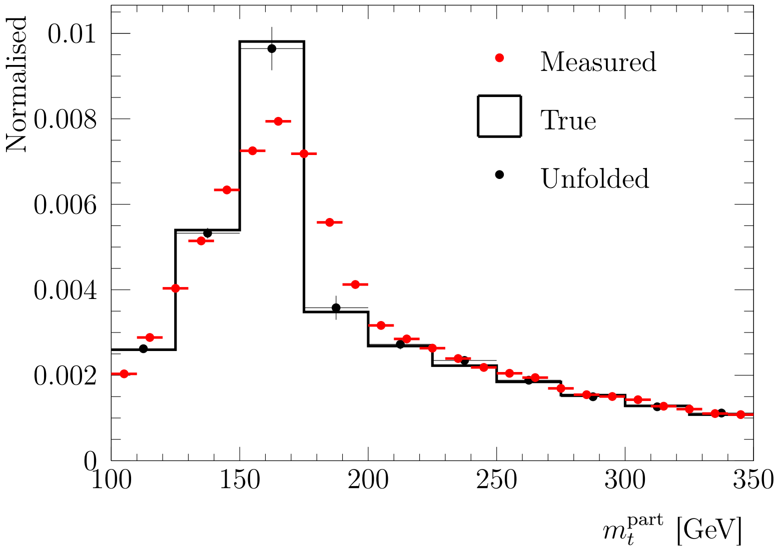

Fig. 10.5: Result of unfolding the same pseudo-dataset as in figure 9.4a. The shown uncertainty also includes the uncertainty due to the modeling of the jet energy resolution. See the text for details on how this additional uncertainty is evaluated.

additional uncertainty in one bin can in principle be determined by taking the difference after unfolding the reconstruction level distributions in both samples. However, this only yields the observed uncertainty for these two samples and does not allow the determination of the correlation between the bins.
To estimate the expected uncertainty (given by the expected difference), an ensemble test has to be performed. However, the nominal and JER sample are not statistically independent as they only differ in the detector simulation but are identical up to the particle level. Therefore, the reconstruction level distribution cannot be varied independently in an ensemble test. A method called Bootstrapping is used to generate the pseudo-datasets for the test [78]. In this method, for every simulated event, an event-weight is drawn from a Poisson distribution with $\nu = 1$ for every pseudo-dataset. If another sample using the same basic events is processed (as is the case for the nominal and JER $t\bar{t}$ signal sample), the same weights are used. The expected difference and correlation between the different bins is then obtained from averaging over the unfolded distributions in these pseudo-datasets. The method has the benefit of correctly producing the correlation of different histograms. Additionally, it separates the statistical fluctuations which affect both nominal and JER in the same way from the systematic difference due to the additional smearing applied to the jets' energies.

The covariance matrix for the expected uncertainty is then estimated by using this method and generating 1000 pairs of pseudo-datasets. The estimated covariance matrix for JER is then scaled to match the statistic of $N = 100000$ used in all ensemble tests presented before. To obtain the total covariance matrix of the unfolded histogram in m_t^{part}, both the matrix for JER and the one obtained from the unfolding procedure for this pseudo-dataset are added.

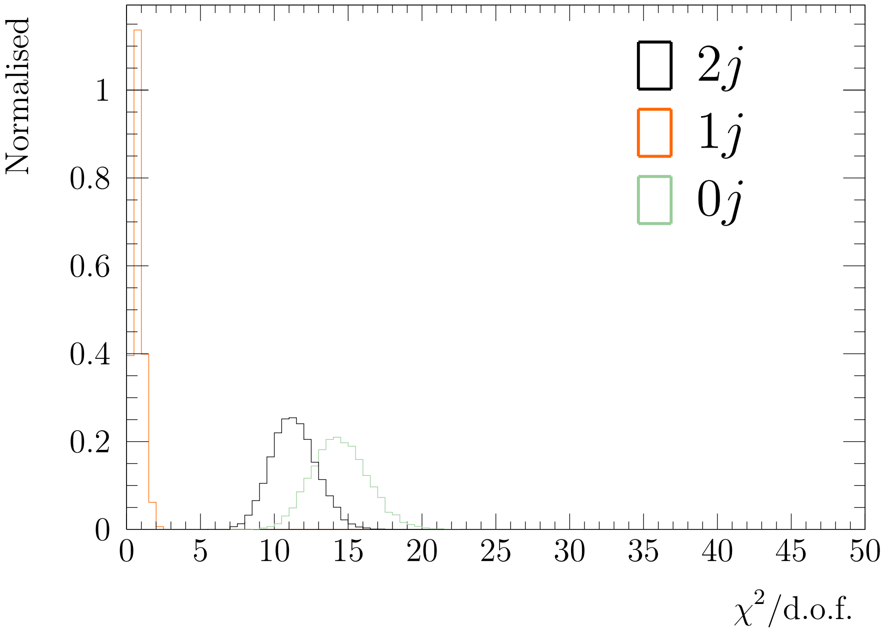

Fig. 10.6: Reduced χ^2 to illustrate the separability of samples with different matrix element multiplicity after unfolding the reconstruction level distribution. Covariance matrix for the uncertainty on the jet energy resolution modelling was considered in the calculation of χ^2.

Figure 10.5 shows the result of the unfolding for the same pseudo-dataset as used before. However, the shown uncertainty includes the estimate for the JER uncertainty. As can be seen, its effect is largest at the peak of the distribution. This is expected as those bins are the most affected by the additional bin migration due to the additional smearing of the energies. Unfortunately, those bins also have the highest sensitivity to the top-quark decay width. Hence the estimated uncertainty due to JER is consistent with the large impact seen when estimating Γ_t.

Figure 10.6 shows again the result of an ensemble test to investigate the separability between the different matrix element multiplicities. It is obtained by using the total covariance matrix in the test discussed in Section 9.4. Even though less than before, the $0j$ and $2j$ can still be clearly separated from the distribution for $1j$. Concluding this, there is still great potential in using the particle level distributions to test different models. However, it remains to be seen how this picture changes once all systematic uncertainties are considered.

11 Conclusion and Outlook

In this thesis, studies on the fiducial measurement of the differential cross section $\mathrm{d}\sigma/\,\mathrm{d}m_t^{part}$ are performed and the potential for measuring the top-quark decay width using this distribution is investigated. The studies are performed in the context of the ATLAS experiment at $\sqrt{s} = 8\,\text{TeV}$ using events with semileptonic decays of $t\bar{t}$ pairs with electrons and muons in the final state. Additionally, at least four jets need to be present in those events with a minimum of two of these jets being tagged as b-jets.
The fiducial measurement is defined on the particle level consisting of all particles stable enough to be detected. It is argued that observables on this level are independent of both detector and modelling effects. These stable particles are classified and clustered to obtain the objects resembling the actual physical objects also measured by the detector: electrons, muons and jets. In these studies, only hadronically decaying top-quarks formed by combining one b- and two non-b-tagged jets are used.

The object definition is applied to several Monte Carlo samples for different Γ_t in order to determine the expected sensitivity in an actual measurement of this quantity. For a statistics corresponding to the expected number of signal events in the full 8 TeV dataset, the expected statistical uncertainty on Γ_t is found to be about 0.3 GeV. This result is obtained by using only Monte Carlo truth information and does not even include any detector effects. Comparing this to the predicted value within the standard model of $\Gamma_t = 1.3\,\text{GeV}$ already illustrates the limited precision expected in a direct measurement of Γ_t. This is caused by the shape of $\mathrm{d}\sigma/\,\mathrm{d}m_t^{part}$ being already dominated by jet clustering effects instead of the decay width of the top-quark. Consequently, the statistical precision is reduced once detector effects are included. Using reconstruction level distributions, an expected statistical precision of roughly 1 GeV is obtained from the studies. This is substantially larger than the expected value on particle level alone and comparable to the predicted value for Γ_t itself. Extensive studies are performed to optimise the unfolding which is used to correct for the detector effects yielding the fiducial measurement on particle level. Overall, a good performance of the unfolding is achieved with only a small bias on the estimated Γ_t. However, unfolding itself cannot add information to the measurement and thus it is not surprising that no gain in sensitivity is seen when applying it. Furthermore, technical difficulties will arise once systematic uncertainties have to be constrained as multi-dimensional unfolding will become necessary. Especially uncertainties affecting the resolution of the measured energies require such a treatment as their effect on

the shape of $\mathrm{d}\sigma/\,\mathrm{d}m_t$ is similar to Γ_t and thus introduces a large bias. Lastly, the result still depends on the modelling of the templates used in the fit and thus the extracted value Γ_t does not fulfil the defining criteria for a fiducial measurement.
Concluding this, using a fiducial measurement of $\mathrm{d}\sigma/\,\mathrm{d}m_t^{part}$ to perform a single measurement of Γ_t cannot be recommended as no benefit is seen outweighing the additional level of complexity due to unfolding. This picture might change once a measurement combining the fiducial cross-sections from different experiments is performed. In a single measurement not aiming for a fiducial measurement, reconstruction level distributions can be used. A more sophisticated top-quark reconstruction – e.g. using a kinematic fit – can be performed. This will greatly reduce the combinatorial background, allow to incorporate additional information in every event and grant the possibility to reduce the minimal number of b-tagged jets in an event. Consequently, a better statistical precision should be achievable.

The here presented studies demonstrate that it is indeed possible to unfold the distribution in m_t^{reco}. Before, this was uncertain due to the challenge of reconstructing the peak in a distribution affected by a resolution whose magnitude is comparable to the peak itself.
While the fiducial cross-section is not beneficial in measuring the decay width, it is a very interesting measurement in itself. It has great model testing capabilities without having to include a simulation of the detector in the model prediction when comparing different models to the measured data. This is demonstrated by testing the separability of different simulations using matrix elements with varying multiplicities of additional partons. It is also demonstrated how systematic uncertainties can be propagated to the unfolded distribution on particle level. As all studies revealed a well-performing unfolding, it could now be applied to the measured distribution in data. After subtracting the expected background, the unfolding method is applied as discussed in detail in this thesis. It should take into account the efficiency to properly estimate the actual distribution on particle level.

A Additional Figures

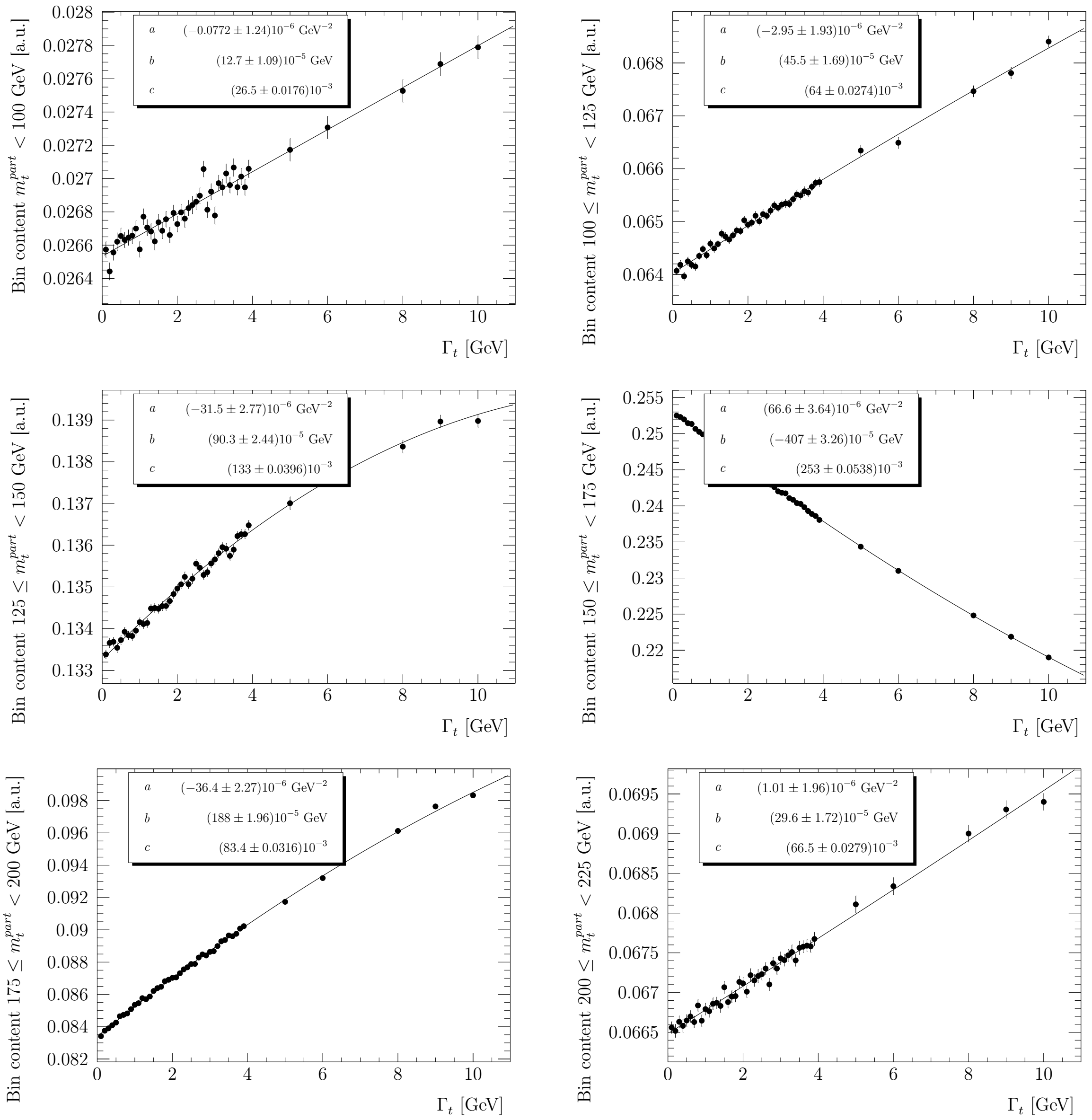

Fig. A.1: Bin parametrisations as a function of Γ_t.

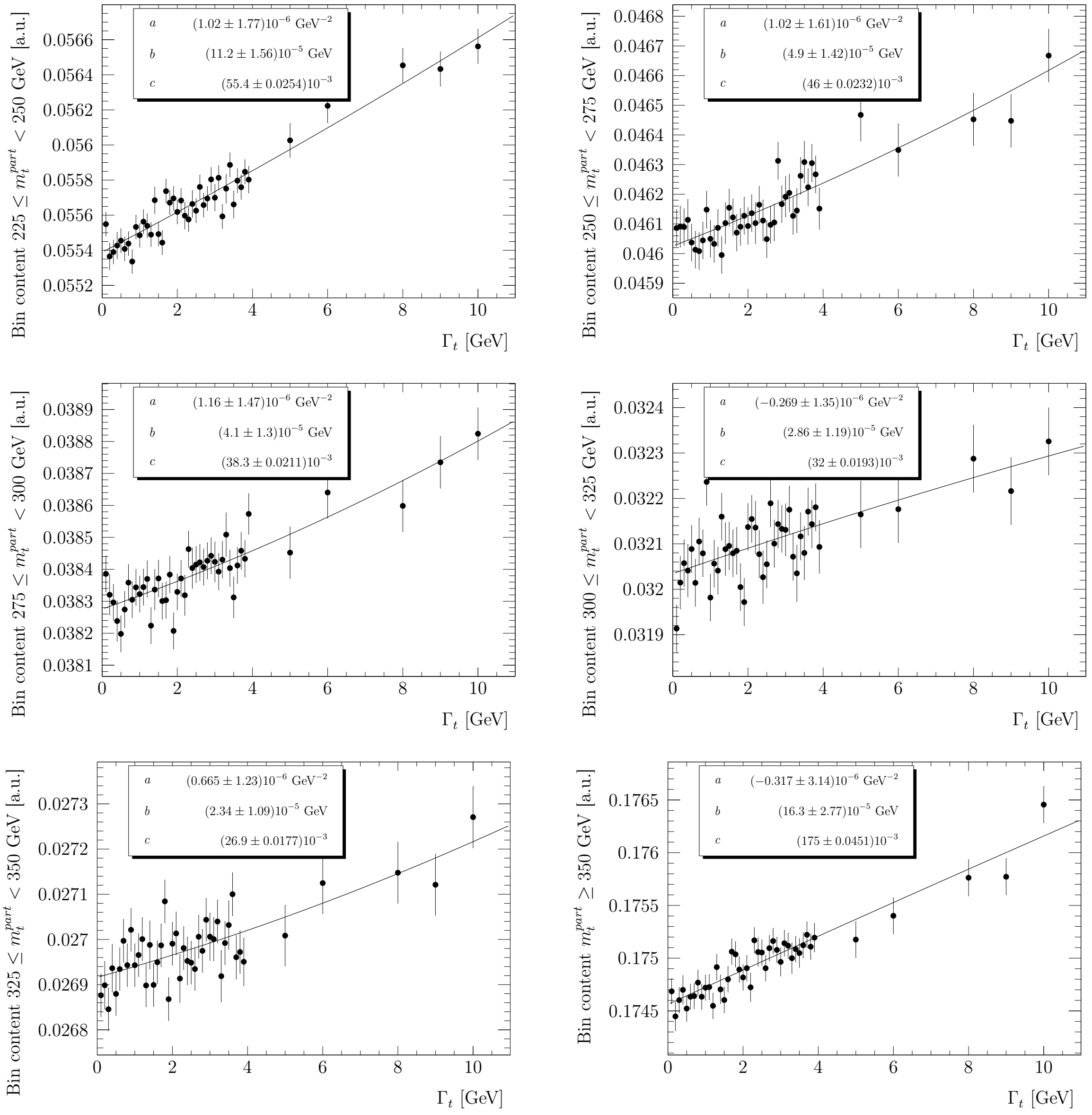

Fig. A.2: Bin parametrisations as a function of Γ_t.

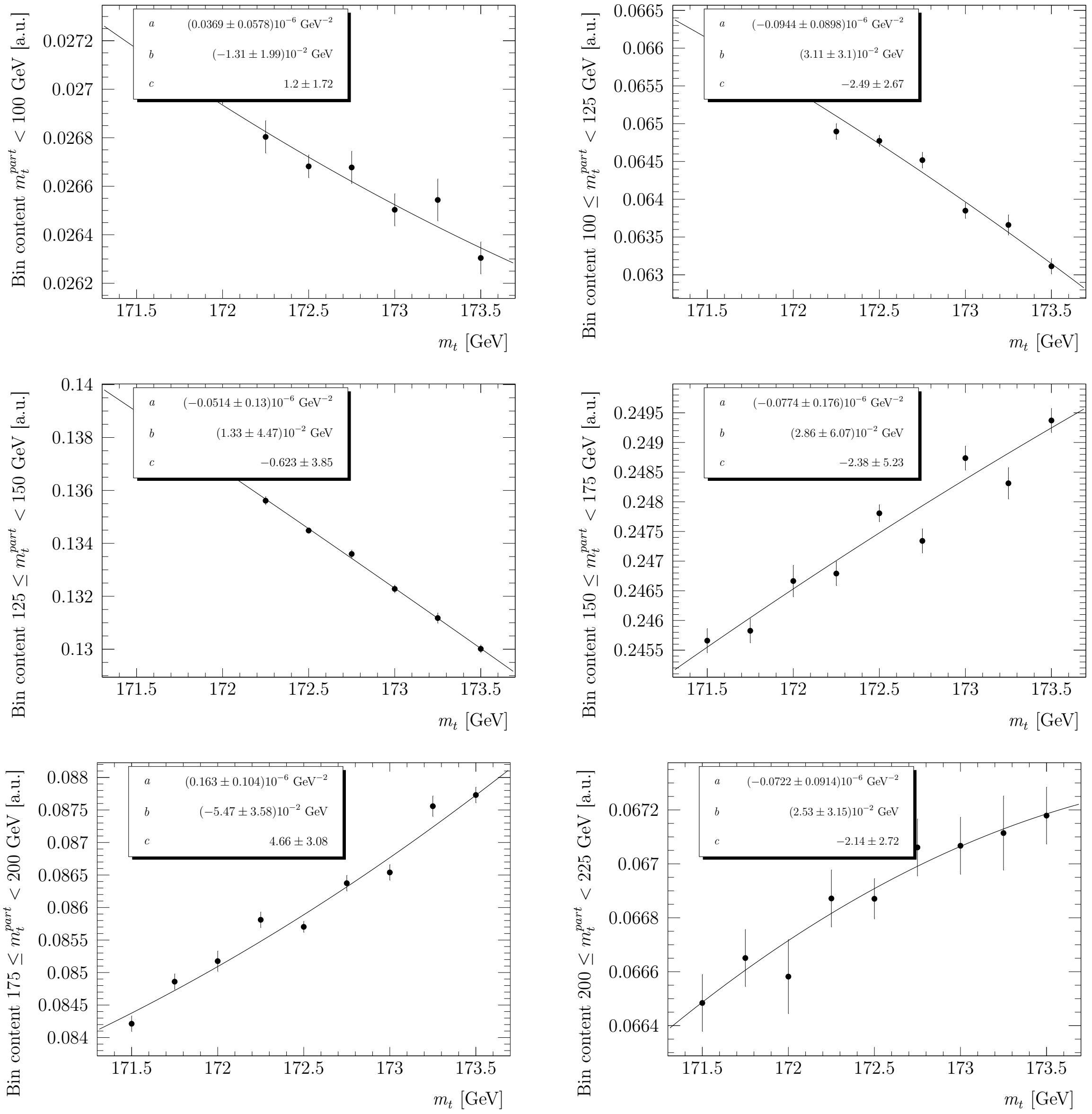

Fig. A.3: Bin parametrisations as a function of m_t.

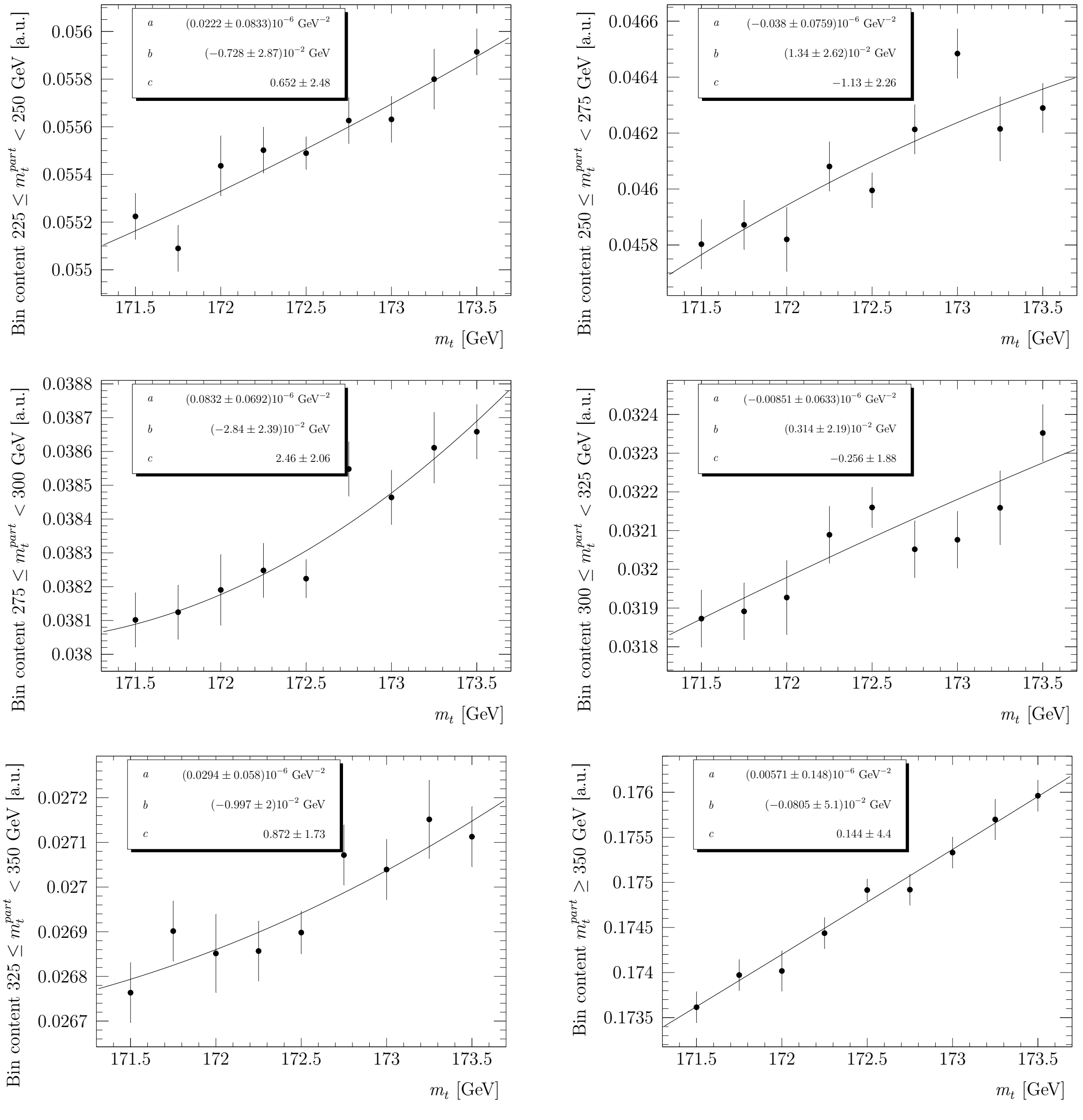

Fig. A.4: Bin parametrisations as a function of m_t.

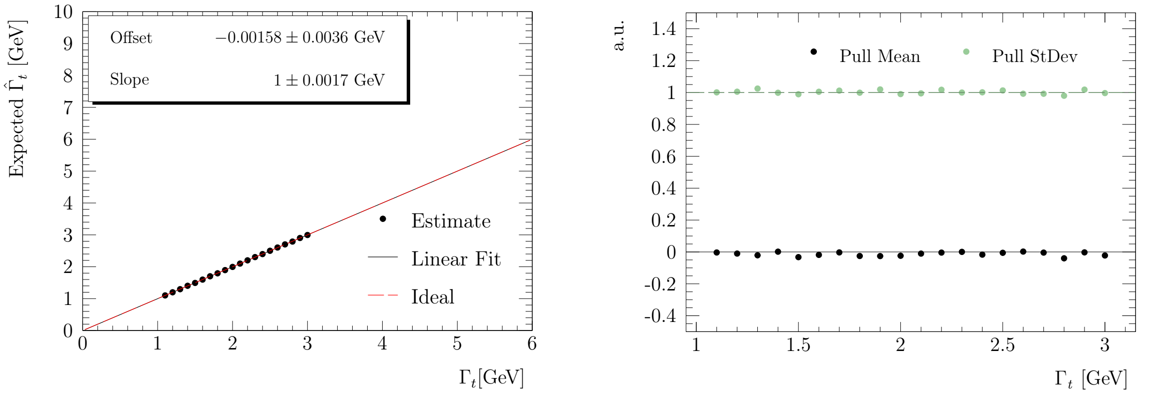

(a) $E(\hat{\Gamma}_t)$ on particle level

(b) Pull on particle level

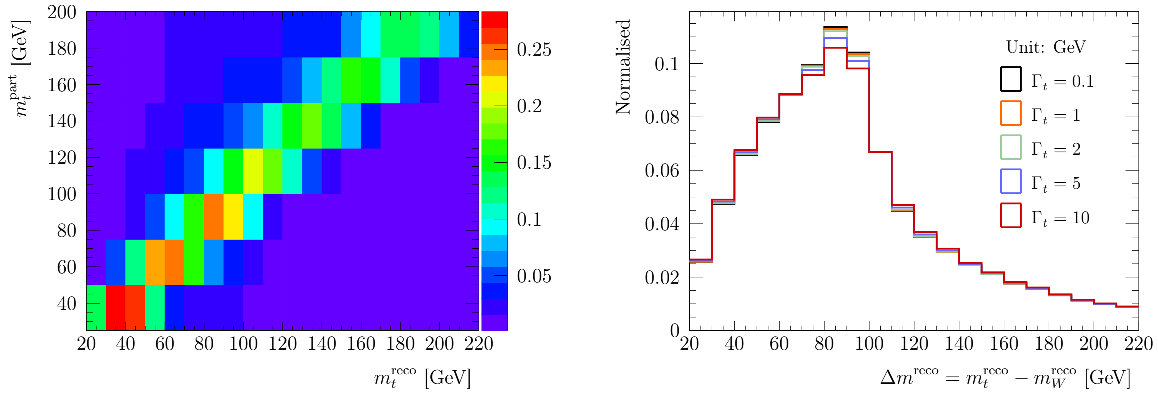

(c) Response matrix

(d) Reconstruction level

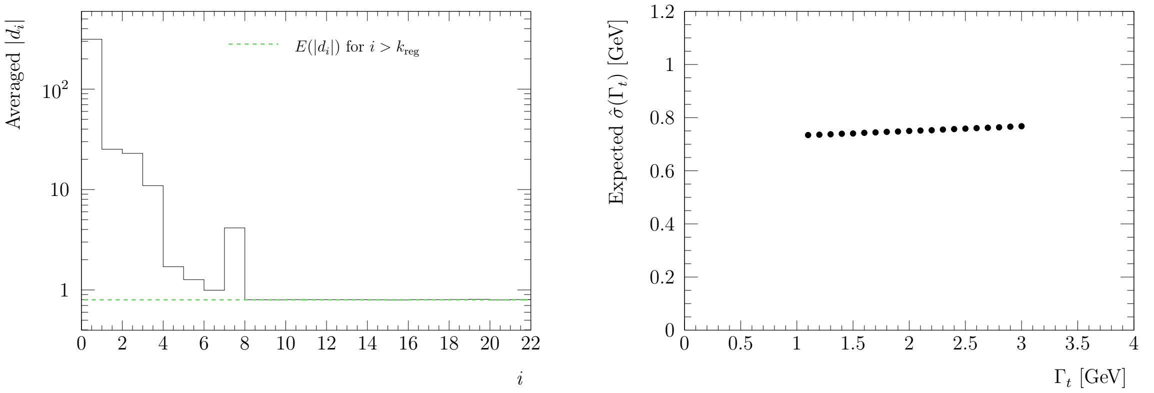

(e) Average $|d_i|$

(f) Expected statistical uncertainty after unfolding

Fig. A.5: Distributions for the alternate observable $\Delta m = m_t - m_W$.

Bibliography

[1] K. A. Olive *et al.* (Particle Data Group), *Review of Particle Physics*, Chin. Phys. C, **38**, 090001 (2014)

[2] S. Weinberg, *A Model of Leptons*, Phys. Rev. Lett., **19**, 1264 (1967)

[3] A. Salam *et al.*, *Electromagnetic and weak interactions*, Phys. Lett., **132**, 168 (1964)

[4] S. L. Glashow, *Partial-symmetries of weak interactions*, Nucl. Phys., **224**, 579 (1961)

[5] N. Cabibbo, *Unitary Symmetry and Leptonic Decays*, Phys. Rev. Lett., **10**, 531 (1963)

[6] M. Kobayashi *et al.*, *CP-Violation in the Renormalizable Theory of Weak Interaction*, Progr. Theoret. Phys., **492**, 652 (1973)

[7] P. W. Higgs, *Broken Symmetries and the Masses of Gauge Bosons*, Phys. Rev. Lett., **13**, 508 (1964)

[8] F. Englert *et al.*, *Broken Symmetry and the Mass of Gauge Vector Mesons*, Phys. Rev. Lett., **13**, 321 (1964)

[9] The CMS Collaboration, *Observation of a new boson at a mass of 125 GeV with the CMS experiment at the LHC*, Phys. Lett. B, **7161**, 30 (2012)

[10] The ATLAS Collaboration, *Observation of a new particle in the search for the Standard Model Higgs boson with the ATLAS detector at the LHC*, Phys. Lett. B, **7161**, 1 (2012)

[11] F. Abe *et al.* (CDF Collaboration), *Observation of Top Quark Production in $\overline{p}p$ Collisions with the Collider Detector at Fermilab*, Phys. Rev. Lett., **74**, 2626 (1995)

[12] S. Abachi *et al.* (D0 Collaboration), *Observation of the Top Quark*, Phys. Rev. Lett., **74**, 2632 (1995)

[13] T. Aaltonen *et al.* (CDF and D0 Collaborations), *Combination of the top-quark mass measurements from the Tevatron collider*, Phys. Rev. D, **86**, 092003 (2012)

[14] The ATLAS, CDF, CMS, and D0 Collaborations, *First combination of Tevatron and LHC measurements of the top-quark mass*, ATLAS-CONF-2014-008, CDF-NOTE-11071, CMS-PAS-TOP-13-014, D0-NOTE-6416 (2014)

[15] The ATLAS Collaboration, *Measurement of the top quark charge in pp collisions at $\sqrt{s} = 7$ TeV with the ATLAS detector*, J. High Energy Phys., **201311**, 1 (2013)

[16] A. Quadt, *Top quark physics at hadron colliders*, Eur. Phys. J. C, **483**, 835 (2006)

[17] The Durham HepData Project, *Online PDF plotting and calculation*, `http://hepdata.cedar.ac.uk/pdf/pdf3.html`, accessed: 12.07.2012

[18] The ATLAS Collaboration, *ATLAS Experiment - Public Results*, `https://twiki.cern.ch/twiki/bin/view/AtlasPublic/CombinedSummaryPlots`, accessed: 25.09.2014

[19] The ATLAS Collaboration, *A search for flavour changing neutral currents in top-quark decays in pp collision data collected with the ATLAS detector at* $\sqrt{s} = 7\ TeV$, J. High Energy Phys., **20129**, 1 (2012)

[20] A. Denner *et al.*, *The top width*, Nucl. Phys. B, **3581**, 46 (1991)

[21] A. Czarnecki *et al.*, *Two-loop QCD corrections to top quark width*, Nucl. Phys. B, **5443**, 520 (1999)

[22] K. G. Chetyrkin *et al.*, *Second order QCD corrections to* $\Gamma(t \to Wb)$, Phys. Rev. D, **60**, 114015 (1999)

[23] J. Gao *et al.*, *Top-Quark Decay at Next-to-Next-to-Leading Order in QCD*, Phys. Rev. Lett., **110**, 042001 (2013)

[24] N. Craig *et al.*, *Exclusive signals of an extended Higgs sector*, J. High Energy Phys., **201211**, 83 (2012)

[25] V. M. Abazov *et al.* (D0 Collaboration), *Improved determination of the width of the top quark*, Phys. Rev. D, **85**, 091104 (2012)

[26] The CMS Collaboration, *Measurement of the ratio in pp collisions at*, Physics Letters B, **736**, 33 (2014)

[27] T. Aaltonen *et al.* (CDF Collaboration), *Direct Measurement of the Total Decay Width of the Top Quark*, Phys. Rev. Lett., **111**, 202001 (2013)

[28] A. Buckley *et al.*, *General-purpose event generators for LHC physics*, Phys. Rep., **504**, 145 (2011)

[29] CERN, *TE-EPC-LPC in LHC*, `http://te-epc-lpc.web.cern.ch/te-epc-lpc/machines/lhc/general.stm`, accessed: 25.09.2014

[30] L. Evans *et al.*, *LHC Machine*, J. Instrum., **308**, S08001 (2008)

[31] CERN, *The accelerator complex*, `http://home.web.cern.ch/about/accelerators`, accessed: 24.07.2014

[32] K. Wille, *The Physics of Particle Accelerators: An Introduction*, Oxford University Press, Oxford (2001)

[33] The ATLAS Collaboration, *ATLAS Experiment - Public Results*, `https://twiki.cern.ch/twiki/bin/view/AtlasPublic/LuminosityPublicResults`, accessed: 07.05.2014

[34] The CMS Collaboration, *The CMS experiment at the CERN LHC*, J. Instrum., **308**, S08004 (2008)

[35] The LHCb Collaboration, *The LHCb Detector at the LHC*, J. Instrum., **308**, S08005 (2008)

[36] The ALICE Collaboration, *The ALICE experiment at the CERN LHC*, J. Instrum., **308**, S08002 (2008)

[37] The ATLAS Collaboration, *The ATLAS Experiment at the CERN Large Hadron Collider*, J. Instrum., **308**, S08003 (2008)

[38] The ATLAS Collaboration, *ATLAS Experiment - Photos*, `http://www.atlas.ch/photos/atlas_photos/selected-photos/full-detector/0803012_01-A4-at-144-dpi.jpg`, accessed: 12.06.2012

[39] B. Dolgoshein, *Transition radiation detectors*, Nucl. Instrum. Meth. A, **3263**, 434 (1993)

[40] The ATLAS Collaboration, *Performance of the ATLAS Trigger System in 2010*, Eur. Phys. J. C, **72**, 1849 (2011)

[41] A. Höcker *et al.*, *SVD approach to data unfolding*, Nucl. Instrum. Meth. A, **3723**, 469 (1996)

[42] A. N. Tikhonov *et al.*, *Solutions of Ill-Posed Problems*, V. H. Winston & Sons, Washington, D.C.: John Wiley & Sons, New York, (1977)

[43] T. Adye, *Unfolding algorithms and tests using RooUnfold*, arXiv:1105.1160 (2011)

[44] M. Cacciari *et al.*, *The anti-k_t jet clustering algorithm*, J. High Energy Phys., **200804**, 063 (2008)

[45] J. Erdmann *et al.*, *A likelihood-based reconstruction algorithm for top-quark pairs and the KLFitter framework*, Nucl. Instrum. Meth. A, **7480**, 18 (2014)

[46] The ATLAS Collaboration, *Measurement of the $t\bar{t}$ production cross-section as a function of jet multiplicity and jet transverse momentum in 7 TeV proton-proton collisions with the ATLAS detector*, arXiv: 1407.0891, submitted to J. High Energy Phys.

[47] T. Gleisberg *et al.*, *Event generation with SHERPA 1.1*, J. High Energy Phys., **0902**, 007 (2009)

[48] S. Schumann *et al.*, *A Parton shower algorithm based on Catani-Seymour dipole factorisation*, J. High Energy Phys., **0803**, 038 (2008)

[49] F. Krauss *et al.*, *AMEGIC++ 1.0: A Matrix element generator in C++*, J. High Energy Phys., **0202**, 044 (2002)

[50] T. Gleisberg *et al.*, *Comix, a new matrix element generator*, J. High Energy Phys., **0812**, 039 (2008)

[51] S. Hoeche *et al.*, *QCD matrix elements and truncated showers*, J. High Energy Phys., **0905**, 053 (2009)

[52] M. Schonherr *et al.*, *Soft Photon Radiation in Particle Decays in SHERPA*, J. High Energy Phys., **0812**, 018 (2008)

[53] M. Dobbs *et al.*, *The HepMC C++ Monte Carlo event record for High Energy Physics*, Comput. Phys. Commun., **1341**, 41 (2001)

[54] M. Cacciari *et al.*, *FastJet User Manual*, Eur. Phys. J. C, **72**, 1896 (2012)

[55] M. Cacciari *et al.*, *Dispelling the N^3 myth for the k_t jet-finder*, Phys. Lett. B, **641**, 57 (2006)

[56] F. James *et al.*, *Minuit: A System for Function Minimization and Analysis of the Parameter Errors and Correlations*, Comput. Phys. Commun., **10**, 343 (1975)

[57] The ATLAS Collaboration, *Commissioning of the ATLAS high-performance b-tagging algorithms in the 7 TeV collision data*, ATLAS-CONF-2011-102 (2011)

[58] The ATLAS Collaboration, *Calibration of the performance of b-tagging for c and light-flavour jets in the 2012 ATLAS data*, ATLAS-CONF-2014-046 (2014)

[59] The ATLAS Collaboration, *Electron reconstruction and identification efficiency measurements with the ATLAS detector using the 2011 LHC proton-proton collision data*, Eur. Phys. J. C, **747**, 2941 (2014)

[60] The ATLAS Collaboration, *Electron efficiency measurements with the ATLAS detector using the 2012 LHC proton-proton collision data*, ATLAS-CONF-2014-032 (2014)

[61] The ATLAS Collaboration, *Measurement of the muon reconstruction performance of the ATLAS detector using 2011 and 2012 LHC proton–proton collision data*, CERN-PH-EP-2014-151 (2014)

[62] The ATLAS Collaboration, *TopRootCore*, `https://twiki.cern.ch/twiki/bin/viewauth/AtlasProtected/TopRootCore`, accessed 21.08.2014

[63] S. Agostinelli *et al.*, *Geant4 – a simulation toolkit*, Nucl. Instrum. Meth. A, **5063**, 250 (2003)

[64] The ATLAS Collaboration, *The ATLAS Simulation Infrastructure*, Eur. Phys. J. C, **703**, 823 (2010)

[65] P. Nason, *A new method for combining NLO QCD with shower Monte Carlo algorithms*, J. High Energy Phys., **200411**, 040 (2004)

[66] S. Frixione *et al.*, *Matching NLO QCD computations with parton shower simulations: the POWHEG method*, J. High Energy Phys., **200711**, 070 (2007)

[67] S. Alioli *et al.*, *A general framework for implementing NLO calculations in shower Monte Carlo programs: the POWHEG BOX*, J. High Energy Phys., **1006**, 043 (2010)

[68] H.-L. Lai *et al.*, *New parton distributions for collider physics*, Phys. Rev. D, **82**, 074024 (2010)

[69] T. Sjöstrand *et al.*, *PYTHIA 6.4 physics and manual*, J. High Energy Phys., **200605**, 026 (2006)

[70] J. Pumplin *et al.*, *New Generation of Parton Distributions with Uncertainties from Global QCD Analysis*, J. High Energy Phys., **200207**, 012 (2002)

[71] M. L. Mangano *et al.*, *ALPGEN, a generator for hard multiparton processes in hadronic collisions*, J. High Energy Phys., **200307**, 001 (2003)

[72] G. Corcella *et al.*, *HERWIG 6: an event generator for hadron emission reactions with interfering gluons (including supersymmetric processes)*, J. High Energy Phys., **200101**, 010 (2001)

[73] B. P. Kersevan *et al.*, *The Monte Carlo event generator AcerMC versions 2.0 to 3.8 with interfaces to PYTHIA 6.4, HERWIG 6.5 and ARIADNE 4.1*, Comput. Phys. Commun., **1843**, 919 (2013)

[74] The ATLAS Collaboration, *Background studies for top-pair production in lepton plus jets final states in $\sqrt{s} = 7$ TeV ATLAS data*, ATLAS-CONF-2010-087 (2010)

[75] K. Becker *et al.*, *Estimation of Fake Lepton Background for Top Analyses Using the $\sqrt{s} = 8$ TeV Dataset*, ATL-COM-PHYS-2013-1100 (2013)

[76] The ATLAS Collaboration, *Jet energy resolution in proton-proton collisions at $\sqrt{\mathrm{s}} = 7$ TeV recorded in 2010 with the ATLAS detector*, Eur. Phys. J. C, **733**, 2306 (2013)

[77] G. D'Agostini, *A Multidimensional unfolding method based on Bayes' theorem*, Nucl. Instrum. Meth. A, **362**, 487 (1995)

[78] B. Efron, *Bootstrap Methods: Another Look at the Jackknife*, Ann. Statist., **71**, 1 (1979)

Acknowledgement

Foremost, I would like to thank Prof. Dr. Arnulf Quadt for giving me the opportunity to write my Master's thesis in particle physics and for being the first referee of this thesis. I am very grateful for his support in the past years which allowed me to participate in the CERN summer student program. My development from a Bachelor's student with no experience in particle physics to a person having a profound knowledge in this field is owed to his dedication and supervision. Furthermore, my thanks go to Prof. Dr. Ariane Frey for being the second referee.

I am very thankful to Prof Dr. Kevin Kröninger for being my supervisor and for proofreading my thesis. The countless discussions on my project and his many suggestions were tremendously helpful and allowed me to hone my skills as a particle physicist. My congratulations again for scoring the professorship.

Many thanks to Philipp Stolte for his support and help during this project and to Nils-Arne Rosien for sharing an office with me.

Moreover, I owe thanks to all the members of the institute, especially to the top working group, for all the fast and profound help as soon as I had any questions or technical complications.

My heartfelt gratitude goes to Fabian Wilk for the countless hours of discussions on particle physics and computing which were very helpful for developing my skills. I also want to thank my family and especially my parents for their endless support during my studies. Finally, my special thanks to my girlfriend Nedaa for her invaluable support, love and confidence in me. Thank you so much!

Erklärung

nach §17(9) der Prüfungs- und Studienordnung für den Bachelor-Studiengang Physik und den Master-Studiengang Physik an der Universität Göttingen:

Hiermit erkläre ich, dass ich diese Abschlussarbeit selbständig verfasst habe, keine anderen als die angegebenen Quellen und Hilfsmittel benutzt habe und alle Stellen, die wörtlich oder sinngemäß aus veröffentlichten Schriften entnommen wurden, als solche kenntlich gemacht habe.
Darüberhinaus erkläre ich, dass diese Abschlussarbeit nicht, auch nicht auszugsweise, im Rahmen einer nichtbestandenen Prüfung an dieser oder einer anderen Hochschule eingereicht wurde.

Göttingen, den October 28, 2014

(Dominik Müller)